

พฤติกรรมการกีดกันของโลหะผสมนิกเกิล-ทังสเตนผลึกนาโน

นายอำนวยการศักดิ์ เจียรไพโรจน์

วิทยานิพนธ์นี้เป็นส่วนหนึ่งของการศึกษาตามหลักสูตรปริญญาวิศวกรรมศาสตรดุษฎีบัณฑิต

สาขาวิชาวิศวกรรมโลหการ ภาควิชาวิศวกรรมโลหการ

คณะวิศวกรรมศาสตร์ จุฬาลงกรณ์มหาวิทยาลัย

ปีการศึกษา 2554

ลิขสิทธิ์ของจุฬาลงกรณ์มหาวิทยาลัย

บทคัดย่อและแฟ้มข้อมูลฉบับเต็มของวิทยานิพนธ์ตั้งแต่ปีการศึกษา 2554 ที่ให้บริการในคลังปัญญาจุฬาฯ (CUIR)

เป็นแฟ้มข้อมูลของนิสิตเจ้าของวิทยานิพนธ์ที่ส่งผ่านทางบัณฑิตวิทยาลัย

The abstract and full text of theses from the academic year 2011 in Chulalongkorn University Intellectual Repository(CUIR)
are the thesis authors' files submitted through the Graduate School.

CORROSION BEHAVIORS OF NANOCRYSTALLINE Ni-W ALLOYS

Mr. Amnuaysak Chianpairot

A Dissertation Submitted in Partial Fulfillment of the Requirements
for the Degree of Doctor of Engineering Program in Metallurgical Engineering

Department of Metallurgical Engineering

Faculty of Engineering

Chulalongkorn University

Academic year 2011

Copyright of Chulalongkorn University

Thesis Title	CORROSION BEHAVIORS OF NANOCRYSTALLINE Ni-W ALLOYS
By	Mr. Amnuaysak Chianpairot
Field of Study	Metallurgical Engineering
Thesis Advisor	Associate Professor Gobboon Lothongkum
Thesis Co-advisor	Dr. Yuttanant Boonyongmaneerat
Thesis Co-advisor	Professor Christopher A. Schuh

Accepted by the Faculty of Engineering, Chulalongkorn University in Partial Fulfillment of the Requirements for the Doctoral Degree

..... Dean of the Faculty of Engineering
(Associate Professor Boonsom Lerdhirunwong, Dr.Ing.)

THESIS COMMITTEE

..... Chairman
(Assistant Professor Ekasit Nisaratanaporn, Ph.D. DIC)

..... Thesis Advisor
(Associate Professor Gobboon Lothongkum, Dr.-Ing.)

..... Thesis Co-advisor
(Yuttanant Boonyongmaneerat, Ph.D.)

..... Thesis Co-advisor
(Professor Christopher A. Schuh, Ph.D.)

..... Examiner
(Assistant Professor Patama Visuttipitukul, Ph.D.)

..... Examiner
(Boonrat Lohwongwatana, Ph.D.)

..... External Examiner
(Wanida Pongsaksawad, Ph.D.)

อำนวยการพิมพ์ : เจียร์ไพโรจน์ : พฤติกรรมการกัดกร่อนของโลหะผสมนิกเกิล-ทังสแตน
ผลึกนาโน (CORROSION BEHAVIORS OF NANOCRYSTALLINE Ni-W
ALLOYS) อ. ที่ปรึกษาวิทยานิพนธ์หลัก : รศ.ดร. กอบบุญ หล่อทองคำ, อ. ที่ปรึกษา
วิทยานิพนธ์ร่วม : ดร. ยุทธนันท์ บุญยงมณีรัตน์, Prof. Christopher A. Schuh,
Ph.D., 135 หน้า.

เนื่องจากความแข็งที่เพิ่มขึ้นอย่างมากของขนาดเกรนระดับนาโน ทำให้โลหะผสม
นิกเกิลทังสแตนผลึกนาโนมีศักยภาพสูงในการใช้เป็นวัสดุเคลือบผิว อย่างไรก็ตาม ความรู้ด้าน
การกัดกร่อนของวัสดุชนิดนี้ยังจำกัด เป็นอุปสรรคต่อการนำไปใช้ในอุตสาหกรรมหลายประเภท
ดังนั้นในการวิจัยนี้ใช้กระบวนการศึกษาปัจจัยต่าง ๆ ที่มีอิทธิพลต่อการกัดกร่อนวัสดุนี้
เป็นระบบ ได้แก่ ขนาดเกรน ปริมาณทังสแตน สัณฐานผลึก องค์ประกอบของพื้นผิว การละลาย
ตัวของขอบเกรน การขยายขนาดของเกรน และค่าพีเอชในสารละลายโซเดียมคลอไรด์ 3.5%
โดยน้ำหนักที่อุณหภูมิห้อง โดยแบ่งการวิจัยออกเป็นสามส่วน ส่วนแรกศึกษาโลหะผสมนิกเกิล
ทังสแตนผลึกนาโนที่มีขนาดเกรนต่าง ๆ ซึ่งสังเคราะห์ด้วยกระบวนการชุบด้วยไฟฟ้า พบว่า
ปัจจัยที่ควบคุมการกัดกร่อนในสภาวะเบส คือ ปริมาณทังสแตนและสัณฐานผลึก และปัจจัย
ควบคุมการกัดกร่อนในสภาวะกรด คือ ปริมาณทังสแตน ส่วนที่สองศึกษาโลหะผสมนิกเกิล
ทังสแตนผลึกนาโนที่ผ่านการอบด้วยความร้อน เพื่อจำแนกผลของการละลายตัวของขอบเกรน
และการขยายขนาดของเกรนต่อการกัดกร่อน พบว่า ผลของปัจจัยทั้งสองต่ออัตราการกัด
กร่อนไม่มีนัยสำคัญ ส่วนที่สามใช้เทคนิคอิเล็กโทรเคมีคอลลิมพีแดนซ์ ศึกษากระบวนการทาง
เคมีไฟฟ้าของการกัดกร่อนที่ผิวหน้าสัมผัสระหว่างชิ้นงานและสารละลายหรืออินเตอร์เฟส
กระบวนการกัดกร่อนที่ผิวหน้าสัมผัสของโลหะผสมนิกเกิลทังสแตนผลึกนาโนถูกควบคุมโดย
ความจุไฟฟ้า (C_{dl}) และความต้านทานการแลกเปลี่ยนประจุ (R_{ct}) ซึ่งบ่งบอกถึงความต้านทาน
การกัดกร่อนของนิกเกิลทังสแตนผลึกนาโน ผลการศึกษาในส่วนที่สามแสดงแนวโน้มของความ
ต้านทานการกัดกร่อนที่สอดคล้องกับผลการศึกษาในส่วนที่หนึ่งและสอง

ภาควิชา วิศวกรรมโลหการ.....ลายมือชื่อ นิสิต.....
สาขาวิชา วิศวกรรมโลหการ.....ลายมือชื่อ อ. ที่ปรึกษาวิทยานิพนธ์หลัก.....
ปีการศึกษา 2554.....ลายมือชื่อ อ.ที่ปรึกษาวิทยานิพนธ์ร่วม.....
ลายมือชื่อ อ.ที่ปรึกษาวิทยานิพนธ์ร่วม.....

4971880521 : MAJOR METALLURGICAL ENGINEERING

KEYWORDS : CORROSION / NANOCRYSTALLINE / NICKEL TUNGSTEN ALLOYS /
GRAIN BOUNDARY RELAXATION / SALINE ENVIRONMENTS

AMNUAYSAK CHIANPAIROT: CORROSION BEHAVIORS OF NANOCRYSTALLINE
Ni-W ALLOYS. ADVISOR : ASSOC. PROF. GOBBOON LOTHONGKUM,
Dr.-Ing., CO-ADVISOR : YUTTANANT BOONYONGMANEERAT, Ph.D., PROF.
CHRISTOPHER A. SCHUH, Ph.D., 135 pp.

Owing to the substantially enhanced hardness of the nanocrystalline (nc) grain size, nc Ni-W alloys show great promise as coating materials. However, the limited knowledge on corrosion of these materials has hindered their utilization in a range of industries. Thus, this research employs a systematic investigation, which is designed to address various factors influencing corrosion, namely, grain size, W content, crystallographic texture, surface composition, grain boundary relaxation, grain growth and pH, in 3.5 wt.% NaCl solution at room temperature. This research is divided into three parts. In part I, electrodeposited nc Ni-W alloys with a range of grain size were investigated. It was found that W content and crystallographic texture are the factors governing corrosion in alkaline condition, while W content is the factor governing corrosion in acidic condition. In Part II, the annealed nc Ni-W specimens were investigated to single out the effects of grain boundary relaxation and grain growth on corrosion. Both effects were found to have insignificant effect on corrosion rate. In part III, electrochemical impedance spectroscopy was utilized to examine the electrochemical corrosion phenomena at the sample/electrolyte interface. Corrosion of nc Ni-W alloys was controlled by capacitance (C_{dl}) and charge transfer resistance (R_{ct}), which indicates corrosion resistance of nc Ni-W alloys. The results in Part III show the similar trends in corrosion resistance to those shown in Parts I and II.

Department : Metallurgical Engineering..... Student's Signature

Field of Study : Metallurgical Engineering Advisor's Signature

Academic Year : 2011..... Co-advisor's Signature

Co-advisor's Signature

ACKNOWLEDGEMENTS

The research work in this Ph.D. thesis was completed under the supervision of Associate Professor Gobboon Lothongkum and Dr. Yuttanant Boonyongmaneerat. I would like to thank Associate Professor Gobboon Lothongkum and Dr. Yuttanant Boonyongmaneerat for continuous guidance, encouragement, and dedication for my academic and career growth. I am thankful to the thesis committee members including, Assistant Professor Ekasit Nisaratanaporn, Assistant Professor Patama Visuttipitukul, Dr. Boonrat Lohwongwatana, and Dr. Wanida Pongsaksawad, for their time and suggestions. My gratitude is also extended to the staff of Metal and Materials Research Institute, Chulalongkorn University, and the members of Poretege Research Group, headed by Dr. Yuttanant Boonyongmaneerat, for all their assistance during my graduate work.

A part of research work in this Ph.D. thesis was carried out under the supervision of Professor Christopher A. Schuh at MIT. I would like to express my gratitude to Professor Schuh and his research group members for their hospitality. I am thankful to Professor Schuh for supporting my experimental work at MIT through his research fund. My gratitude is conveyed to Dr. Chuang Deng, Assistant Professor Timothy Rupert, Dr. Shiyun Ruan, Schuh present and past group members, and Elisabeth Shaw, surface characterization specialist, whose assistance on experimental equipment and techniques is greatly appreciated.

I would like to note with appreciation for Thailand Research Fund through the Royal Golden Jubilee Ph.D. Program (Grant No. PHD/0203/2549), the Chulalongkorn University Centenary Academic Development Project (CIN2551-1.2) and National Metal and Materials Technology Center for financial support.

Finally, I am deeply grateful to my parents, brothers and sisters for their great support and inspiration.

CONTENTS

	Page
ABSTRACT (IN THAI).....	iv
ABSTRACT (IN ENGLISH).....	v
ACKNOWLEDGEMENTS.....	vi
CONTENTS.....	vii
LIST OF TABLES.....	xi
LIST OF FIGURES.....	xii
CHAPTER I INTRODUCTION.....	1
1.1 Motivation.....	1
1.2 Objective of Research.....	5
1.3 Scope of Research.....	5
1.4 Benefits of Research.....	7
CHAPTER II LITERATURE SURVEY.....	8
2.1 Structure of Nanocrystalline Materials.....	8
2.2 Processing of Nanocrystalline Materials.....	13
2.2.1 Gas Condensation and Other Techniques.....	13
2.2.2 Electrodeposition.....	14
2.3 Properties of Nanocrystalline Materials.....	20
2.3.1 Mechanical Behavior.....	20
2.3.2 Corrosion Behavior.....	23
2.4 Nanocrystalline Ni-W Alloys.....	29
2.4.1 A Potential Replacement for Hard Chrome Coating.....	29
2.4.2 Corrosion Behavior of Nanocrystalline Ni-W Alloys.....	31
CHAPTER III EXPERIMENTAL PROCEDURE.....	34
Part I – Corrosion of As-Deposited Nanocrystalline Ni-W.....	34

	Page
1 Electrodeposition.....	34
2 Characterization.....	36
2.1 Tungsten Content.....	37
2.2 Grain Size.....	38
2.3 Crystallographic Texture.....	41
2.4 Surface Morphology and Composition.....	41
3 Potentiodynamic Polarization.....	42
Part II – Corrosion of Annealed Nanocrystalline Ni-W.....	43
1 Heat Treatment.....	44
1.1 Grain Boundary Relaxation.....	44
1.2 Grain Growth.....	46
2 Characterization.....	49
2.1 Tungsten Content.....	49
2.2 Grain Size.....	50
2.3 Hardness.....	50
2.4 Crystallographic Texture.....	50
2.5 Surface Composition.....	51
3 Potentiodynamic Polarization.....	51
Part III – Interfacial Corrosion Phenomena of As-Deposited and Annealed Nanocrystalline Ni-W.....	52
1 Electrochemical Impedance Spectroscopy.....	52
CHAPTER IV EXPERIMENTAL RESULTS.....	55
Part I – Corrosion of As-Deposited Nanocrystalline Ni-W.....	55
1 Electrodeposited Microcrystalline Ni and Nanocrystalline Ni-W Alloys.....	55
2 Corrosion Behavior.....	62
2.1 3.5 wt.% NaCl at pH = 10.....	63

	Page
2.2 3.5 wt.% NaCl at pH = 3.....	66
Part II – Corrosion of Annealed Nanocrystalline Ni-W.....	67
1 Annealed Ni-W Specimens.....	67
2 Corrosion Behavior.....	79
2.1 3.5 wt.% NaCl at pH = 10.....	85
2.2 3.5 wt.% NaCl at pH = 3.....	88
Part III – Interfacial Corrosion Phenomena of As-Deposited and Annealed Nanocrystalline Ni-W.....	90
CHAPTER V DISCUSSION.....	96
Part I – Corrosion of As-Deposited Nanocrystalline Ni-W.....	96
1 As-Deposited Nanocrystalline Ni-W.....	96
2 Corrosion Behavior.....	98
2.1 3.5 wt.% NaCl at pH = 10.....	98
2.2 3.5 wt.% NaCl at pH = 3.....	100
3 Concluding Remarks.....	101
Part II – Corrosion of Annealed Nanocrystalline Ni-W.....	102
1 Annealed Ni-W Specimens.....	102
2 Corrosion Behavior.....	103
2.1 3.5 wt.% NaCl at pH = 10.....	103
2.2 3.5 wt.% NaCl at pH = 3.....	105
3 Concluding Remarks.....	105
Part III – Interfacial Corrosion Phenomena of As-Deposited and Annealed Nanocrystalline Ni-W.....	106
1 Circuit Analog and the Interfacial Model.....	106
2 Validation of the Interfacial Model.....	115
3 Corrosion Behavior.....	117

	Page
4 Structural Characteristics for Enhanced Corrosion and Wear Resistance.....	119
4.1 Grain Size.....	119
4.2 Crystallographic Texture.....	119
4.3 Grain Boundary Relaxation.....	120
5 Concluding Remarks.....	121
CHAPTER VI CONCLUSION.....	122
REFERENCES.....	124
BIOGRAPHY.....	135

LIST OF TABLES

Table		Page
2-1	The relation between the total number of atoms and the percentage of surface atoms (Schmidt, 2001: 23).....	9
2-2	Standard half-cell potentials for WO_4^{2-} , H^+ and Ni^{2+} ions. The equilibrium values suggest that W is preferentially removed from the deposit surface during the reverse (anodic) pulse (Detor, 2007c: 47).....	18
4-1	Physical characteristics of, and associated pulse plating parameters used to prepare, the microcrystalline Ni and nanocrystalline Ni-W deposits.....	56
4-2	I_{corr} and E_{corr} of as-deposited Ni and Ni-W specimens in pH=10 and 3 3.5 wt.% NaCl solutions	65
4-3	The annealing conditions, tungsten content and grain size of the test specimens investigated in Part II.....	68
4-4	Comparison of the hardness of as-deposited and grain-boundary-relaxed specimens.....	69
4-5	I_{corr} and E_{corr} of Ni-6W and Ni-18W specimen series in pH=10 and 3 3.5 wt.% NaCl solutions.....	85
5-1	List of oxidation and reduction reactions on the surfaces of Ni-W specimens in aerated alkaline and acidic saline environments (Vasko, 1985: 239; Anik, and Osseo-Asare, 2002: B224; Vanysek, 2006: 534).....	110
5-2	Electrochemical impedance data of Ni-6W and Ni-18W series in pH=10 and 3 3.5 wt.% NaCl solutions.....	111
5-3	Polarization resistance (R_p), anodic and cathodic Tafel slopes (β_a and β_c) of Ni-6W and Ni-18W specimen series in pH=10 and 3 3.5 wt% NaCl solutions.....	116

LIST OF FIGURES

Figure	Page
2-1 Two-dimensional hard-sphere model of a nanocrystalline solid. The open circles indicate the atoms located at grain boundaries and the solid circles refer to the atoms inside the grains (Gleiter, 1989: 223).....	10
2-2 Atomic probe tomography (APT) image showing segregation of tungsten to grain boundaries in a ~70 nm x 90 nm x 4 nm section of nanocrystalline Ni-W alloys (Detor, Miller, and Schuh, 2007b: 581).....	12
2-3 Definition of variables that control the shape of the applied current waveform used in electrodeposition experiments (Detor, 2007c: 45).....	17
2-4 Cross-sectional SEM micrographs of nanocrystalline Ni-W specimens prepared by (a) conventional D.C. electrodeposition and (b) reverse pulsing control; both specimens have nominally the same composition of ~8 at.%W (Detor, and Schuh, 2007a: 371).....	19
2-5 A graph showing the relationship between the hardness and grain size of Ni-W alloys (Detor, and Schuh, 2007a: 371).....	29
2-6 Polarization curves of nanocrystalline Ni-W alloys with different W content in 1 N sulfuric acid (Sriraman et al., 2007a: 39).....	31
3-1 Schematic diagram of the electrodeposition set-up used to produce nanocrystalline Ni-W alloys	35
3-2 The rectangular current waveform used for reverse pulsed electrodeposition of Ni and Ni-W alloys. The electrodeposition parameters include forward current density (Fwd C.D.), reverse current density (Rev C.D.), forward current on-time (Fwd t_{on}) and reverse current on-time (Rev t_{on}).....	36
3-3 Positions of EDS analysis and hardness measurement on each Ni-W specimen	37

Figure	Page	
3-4	Schematic diagram of the experimental setup used for potentiodynamic polarization and electrochemical impedance spectroscopy (EIS) tests of Ni-W samples. A platinum (Pt) rod was used as a counter electrode (CE) A saturated calomel electrode (SCE) was used as a reference electrode (RE). An as-deposited Ni-W sample was the working electrode.....	43
3-5	The Ni-W grain size quantified by X-ray diffraction analysis for 24-hr heat treatments of three different starting grain sizes (plotted at 25 °C), showing negligible grain growth up to ~300 °C (Detor, and Schuh, 2007d: 3233).....	45
3-6	Differential scanning calorimetry results showing the irreversible heat release in as-deposited 3, 20 and 70 nm grain size specimens. Exothermic signals, beginning at ~120 °C, are attributed to grain boundary relaxation of the as-deposited Ni-W specimens (Detor, and Schuh, 2007d: 3233).....	46
3-7	Nickel-Tungsten binary phase diagram (ASM Handbook V. 3, 1992: 253)	47
3-8	X-ray diffraction patterns for 24-hr heat treatments of an as-deposited (AD) 3 nm grain size specimen containing 21 at.%W. The structure remains fairly stable up to 450 °C followed by grain coarsening at 600°C and eventual precipitation of the equilibrium Ni ₄ W phase at higher temperatures (Detor, and Schuh, 2007d: 3233).....	48
3-9	The annealing scheme for grain growth	49
3-10	A typical Nyquist plot of impedance spectra of an electrochemical system The horizontal axis of the plot is the real part of impedance and the vertical axis is the imaginary part of impedance (Orazem, and Tribollet, 2008: 155).....	53

Figure	Page	
4-1	The interrelationship between reverse current density, tungsten content (solid triangle) and grain size (solid square) of Ni-W alloys. The decrease in reverse current density causes tungsten content in the alloys to increase, promoting the formation of smaller-sized grains through grain boundary segregation of tungsten atoms in Ni matrix.....	56
4-2	X-ray diffraction spectra of nc Ni-W alloys with average grain size ranging from 5 to 63 nm. The expected reflections for nickel are shown in the plot, and the solid diamonds indicate the peaks from the copper substrate.....	57
4-3	The representative {111} and {200} pole figures of electrodeposited (a) Ni-5W (grain size = 63 nm), (b) Ni-6W (grain size = 39 nm) and (c) Ni-18W (grain size = 6 nm) samples, with the surface normal vector coming out of the page. The pole figures of Ni-5W demonstrate preferential orientation of {111} planes at about 50° from the surface normal direction and that of {200} planes in the surface normal direction. However, the pole figures of Ni-6W show relatively uniform orientation of {111} and {200} crystallographic planes, while Ni-18W exhibits strong {111}-fiber texture with {200} crystallographic planes preferentially oriented at about 45° from the surface normal.....	58
4-4	Scanning electron micrographs revealing the surface morphology of (a) mc Ni, (b) Ni-6W and (c) Ni-18W. Relatively large grain structure is observed in mc Ni, whereas fine mesoscale structure, which is the characteristic of nanocrystalline materials, exists in both Ni-6W and Ni-18W.....	59

Figure	Page
4-5	61
<p>Ni 2p and W 4f XPS spectral lines of (a) Surface of as-deposited Ni-6W which contains mostly Ni (as indicated by Ni 2p peak at 852.1 eV) and W (as indicated by W 4f peaks at 31.0 and 33.1 eV) metals and (b) Surface of as-deposited Ni-18W which contains mostly NiWO₄ (as indicated by the combination of Ni 2p peak at 855.7 eV and W 4f peaks at 35.4 and 37.5 eV).....</p>	
4-6	62
<p>Potentiodynamic curves of mc Ni and various nc Ni-W alloys in 3.5 wt.% NaCl solution at pH = 10.....</p>	
4-7	63
<p>Potentiodynamic curves of mc Ni and various nc Ni-W alloys in 3.5 wt.% NaCl solution at pH = 3.....</p>	
4-8	64
<p>The corrosion potential (E_{corr}) (a) and corrosion current density (i_{corr}) (b) of the deposits of various grain sizes. The triangle and square signs represent the data of the deposits tested in 3.5 wt.% NaCl at pH = 3 and at pH = 10, respectively.....</p>	
4-9	66
<p>Morphology of specimens after potentiodynamic tests in 3.5 wt.% NaCl solution: (a) mc Ni and (b) Ni-18W tested in pH = 10 solution; and (c) mc Ni and (d) Ni-18W tested in pH = 3 solution. The large pits in mc Ni (a,c) are signatures of localised corrosion. No such pits are found in nc Ni-W; the small circles in (b,d) are surface nodules in the plated structure, and not corrosion sites.....</p>	
4-10	69
<p>The diagram showing the change of grain size upon annealing temperature of Ni-6W and Ni-18W specimen series.....</p>	
4-11	71
<p>X-ray diffraction spectra of Ni-6W specimen series including Ni-6W-AD (52 nm), Ni-6W-R (54 nm) and Ni-6W-GG (110 nm).....</p>	
4-12	71
<p>X-ray diffraction spectra of Ni-18W sample series including Ni-18W-AD (7 nm), Ni-18W-R (8 nm) and Ni-18W-GG (62 nm).....</p>	

Figure	Page	
4-13	The representative {111} and {200} X-ray diffraction pole figures of Ni-6W sample series (a) Ni-6W-AD (grain size = 52 nm), (b) Ni-6W-R (grain size = 54 nm) and (c) Ni-6W-GG (grain size = 110 nm) samples, with the surface normal vector coming out of the page. The pole figure of Ni-6W-AD specimen shows relatively uniform orientation of {111} and {200} crystallographic planes with slight {200}-fiber texture. There seems to be noticeable change in texture upon grain boundary relaxation. The texture, however, seems to shift back to the original state (Ni-6W-AD) upon grain growth.....	73
4-14	The representative {111} and {200} X-ray diffraction pole figures of Ni-18W sample series (a) Ni-18W-AD (grain size = 7 nm), (b) Ni-18W-R (grain size = 8 nm) and (c) Ni-18W-GG (grain size = 62 nm) samples, with the surface normal vector coming out of the page. The pole figure of the Ni-18W-AD specimen exhibits strong {111}-fiber texture with {200} crystallographic planes preferentially oriented at about 45° from the surface normal. Upon annealing, both Ni-18W-R and Ni-18W-GG samples exhibit different crystallographic textures from that of Ni-18W-AD.....	75
4-15	XPS spectra of Ni-6W specimen series including (a) Ni-6W-AD, (b) Ni-6W-R and (c) Ni-6W-GG, showing similar chemical species on the surface, namely, Ni metal, Ni(OH) ₂ , W metal and W oxide.....	77
4-16	XPS spectra of Ni-18W specimen series including (a) Ni-18W-AD, (b) Ni-18W-R and (c) Ni-18W-GG, showing similar chemical species on the surface, namely, Ni metal, Ni(OH) ₂ , W metal and W oxide.....	78
4-17	Polarization curves of Ni-6W sample series in pH=10 3.5 wt.% NaCl solution.....	79

Figure	Page
4-18 Polarization curves of Ni-18W sample series in pH=10 3.5 wt.% NaCl solution.....	81
4-19 Polarization curves of Ni-6W sample series in pH=3 3.5 wt.% NaCl solution	82
4-20 Polarization curves of Ni-18W sample series in pH=3 3.5 wt.% NaCl solution.....	84
4-21 The plots of E_{corr} (a) and i_{corr} (b) vs. grain size for Ni-6W and Ni-18W specimen series in pH=10 3.5 wt.% NaCl solution. AD denotes as-deposited. R denotes grain boundary relaxation. GG denotes grain growth.....	86
4-22 The plots of E_{corr} (a) and i_{corr} (b) vs. grain size for Ni-6W and Ni-18W specimen series in pH=3 3.5 wt.% NaCl solution. AD denotes as-deposited. R denotes grain boundary relaxation. GG denotes grain growth.....	89
4-23 Nyquist impedance plot of Ni-6W-AD, Ni-6W-R and Ni-6W-GG specimens in pH=10 3.5 wt.% NaCl solution	90
4-24 Nyquist impedance plot of Ni-18W-AD, Ni-18W-R and Ni-18W-GG specimens in pH=10 3.5 wt.% NaCl solution	92
4-25 Nyquist impedance plot of Ni-6W-AD, Ni-6W-R and Ni-6W-GG specimens in pH=3 3.5 wt.% NaCl solution	93
4-26 Nyquist impedance plot of Ni-18W-AD, Ni-18W-R and Ni-18W-GG specimens in pH=3 3.5 wt.% NaCl solution.....	94
5-1 The effect of grain size on calculated volume fractions for intercrystalline regions, grain boundaries, and triple junctions, assuming a grain boundary thickness of 1 nm (Palumbo, Thorpe, and Aust, 24(1990): 1347).....	104

Figure	Page
5-2	107
<p>The circuit analog of the corrosion process of Ni-6W and Ni-18W specimen series in aerated 3.5 wt.% NaCl solution at pH = 10 and 3. The circuit element, R_s, represents the resistance of test solution; R_{ct} represents the charge transfer resistance at the metal/electrolyte interface; C_{dl} represents the capacitance of the electrical double layer formed at the metal/electrolyte interface (Sriraman et al., 2007a: 39; Wang et al., 2006: 657).....</p>	
5-3	109
<p>Representative model of interfacial phenomena occurring during corrosion of nanocrystalline Ni-W alloys in aerated alkaline and acidic saline environments (Gileadi et al., 1975: 89, Jones, 1991: 101; Orazem, and Tribollet, 2008: 142).....</p>	
5-4	112
<p>The plot of double layer capacitance (C_{dl}) vs. grain size for Ni-6W and Ni-18W specimen series in pH=10 and 3 3.5wt.% NaCl solutions. AD denotes as-deposited. R denotes grain boundary relaxation. GG denotes grain growth.....</p>	
5-5	113
<p>The plot of charge transfer resistance (R_{ct}) vs. grain size for Ni-6W and Ni-18W series in pH=10 3.5 wt.% NaCl solution. AD denotes as-deposited. R denotes grain boundary relaxation. GG denotes grain growth.....</p>	
5-6	114
<p>The plot of charge transfer resistance (R_{ct}) vs. grain size for Ni-6W and Ni-18W series in pH=3 3.5 wt.% NaCl solution. AD denotes as-deposited. R denotes grain boundary relaxation. GG denotes grain growth.....</p>	
5-7	116
<p>The plot of polarization resistance (R_p) (derived from i_{corr}) vs. grain size for Ni-6W and Ni-18W series in pH=10 3.5 wt.% NaCl solution. AD denotes as-deposited. R denotes grain boundary relaxation. GG denotes grain growth.....</p>	

Figure		Page
5-8	The plot of polarization resistance (R_p) (derived from i_{corr}) vs. grain size for Ni-6W and Ni-18W series in pH=3 3.5 wt.% NaCl solution. AD denotes as-deposited. R denotes grain boundary relaxation. GG denotes grain growth.....	117

CHAPTER I

INTRODUCTION

1.1 Motivation

Nanocrystalline (nc) materials are normally categorized as the materials with grain size below 100 nm. Within this length scale, the materials can possess as high as 50% volume fraction of grain boundaries and triple junctions. Therefore, in contrast to its microcrystalline counterparts, grain boundaries and triple junctions, instead of grain interior, contribute significantly to the bulk properties of nanocrystalline materials. Consequently, the properties of nanocrystalline materials can hardly be predicted from the behaviors of the conventional coarse-grained polycrystalline materials (Gleiter, 2000:1).

Nanocrystalline materials exhibit numerous interesting properties not found in their bulk microcrystalline counterparts. For instance, nanocrystalline copper has a much higher electrical resistivity than microcrystalline copper (Huang, Menovsky, and de Boer, 1993: 505). This effect is attributed to the enhanced electron scattering effect of grain boundaries. Moreover, the high fraction of grain boundary atoms on the surface of nanocrystalline materials increases the materials' chemical reactivity. Thus, many nanocrystalline materials are used as catalysts for various chemical reactions (Tjong, and Chen, 2004: 1). Furthermore, nanocrystalline metals generally exhibit noticeably larger yield strength and Young's modulus relative to their microcrystalline analogs because of the hindering of dislocation motion by grain boundaries (Tjong, and Chen, 2004: 1).

Because of the unique properties not found in coarse-grained polycrystalline materials, nanocrystalline materials receive immense interest from the scientific community. Moreover, they are increasingly employed in a number of industrial applications in recent years. Thin coatings of nanocrystalline metal and alloys are increasingly used for protecting the underlying substrate or for functional purposes. In these applications, nanocrystalline coatings may inevitably be exposed to various corrosive environments. To employ coating materials effectively, it is therefore essential to examine and understand the corrosion behaviors of the materials. Compared to studies of other materials' properties, however, researches on corrosion of nanocrystalline materials were rarely reported in the literature. This limited knowledge on corrosion of nanocrystalline materials has placed a significant limitation on the utilization of the materials in various potential applications in a range of industries.

With high volume of grain boundaries, one may predict that nanometer structure should accelerate corrosion by forming numerous micro galvanic cells between the large grain boundary volume and the matrix. However, prior studies have hinted that the classical corrosion theory based on grain size alone may not always explain the corrosion behaviors of nanocrystalline materials. Instead, they suggested that to fully capture the corrosion behavior of nanocrystalline metals, the interrelationship between grain size, chemical composition, passive film and corrosion resistance must be understood. For example, it was reported that (Wang et al., 2007: 4342) in NaOH or NaCl solutions, nanocrystalline Co coating exhibited improved corrosion resistance relative to coarse-grained Co coating because the higher grain boundary density in

nanocrystalline Co favors the formation of a continuous and protective passive film. On the contrary, where no apparent passivation was observed, the corrosion rates of nanocrystalline Co coating were higher than coarse-grained Co coating in HCl and H₂SO₄ solutions because high density of grain boundary defects in nanocrystalline Co now act as the preferential sites for corrosion. This interrelationship was also suggested by Liu and colleagues (Liu, Li, and Wang, 2007: 7193), who investigated the electrochemical corrosion behavior of polycrystalline (cast alloy), single-crystalline {200}-fiber textured and nanocrystalline Ni-based superalloy in 3.5 wt.% NaCl solution. They found that nanocrystalline structure has the most compact passive film and that the microstructure affected both the composition and the initial growth of passive film, which determined the compact property of the film and resulted in the observed differences in the corrosion behavior of the three materials.

In addition to the insufficiency of corrosion theory based on grain size alone, only limited investigation of corrosion behavior of nanocrystalline metals were reported in the literature and discrepancy in the reported data were found among different authors. Such discrepancy most likely results from the variation of synthetic methods employed by different research groups, which introduce different structural defects inherent in each processing technique into the materials of identical composition. Many authors also produced coarser grained materials by annealing their nanocrystalline or ultra fine grained analogs, introducing thermally activated structural shift termed "grain boundary relaxation" (Jang, and Atzmon, 2006: 083504) into the materials' structure. Such variation in structural defects in the test specimens investigated by different

research groups must have rendered the reported corrosion data in literature inconclusive. To overcome this problem, in this dissertation, we investigate corrosion behavior of only one alloy system produced by only one processing route in order to keep the variation in structural defects, if any, in different test specimens to the minimum. Furthermore, whenever thermally annealed specimens are investigated, grain boundary relaxation is always accounted for during data analysis.

The Ni-W nanocrystalline alloys are selected as the system of investigation for a number of reasons. First, they possess high hardness (Detor, and Schuh, 2007a: 371), protective surface oxide film (Sriraman, Raman, and Seshadri, 2007a: 39) and surface luster. These are important criteria for protective and decorative coating materials. Second, they are more environmentally friendly and less detrimental to human health than chromium coatings. Thus, they are the potential candidates as a replacement of chromium coatings in automotive industry.

In this work, we select electrodeposition as the processing route because it is the potent processing method that allows active control of nanostructure, such that thorough and systematic scientific investigation can be conducted. Furthermore, it is also an industrially applicable processing method, as it can be implemented in a factory setting with minor alteration of the existing process equipment. The background studies relevant to this work will be discussed in the literature survey section.

1.2 Objective of Research

While there present some prior investigations on the corrosion behaviors of nanocrystalline Ni-W alloys, the corrosion tests were limited to certain conditions, and there still lacks a fundamental understanding of how process variables and contributing factor influence the corrosion properties of the materials. The objective of this proposed dissertation is therefore to investigate the correlation between process variables, nanostructure, chemical composition and corrosion properties of the alloys.

1.3 Scope of Research

To investigate the influence of these factors and understand the corrosion behaviors, particularly in the Ni-W alloy system, the research is designed into three major parts as the following:

1.3.1 Corrosion Behavior of As-Deposited Nanocrystalline Ni-W Alloys

As discussed thus far, it should be clear that there exists interrelationship between alloy composition, grain size, passive film and corrosion resistance. Alloy composition controls grain size and affects the composition of passive film. Grain size affects the nature of defects and kinetics of passive film formation. Finally, the nature of passive film determines the corrosion resistance of nanocrystalline alloys. To investigate this interrelationship, nanocrystalline Ni-W alloys of different grain sizes will be produced by controlling alloying composition via electrodeposition parameters, mainly, current density and temperature. The nature of passive film and corrosion behavior of

nanocrystalline Ni-W alloys will be studied as a function of grain size so as to obtain insight into the interrelationship between alloy composition, grain size, passive film and corrosion resistance of nanocrystalline Ni-W alloys.

1.3.2 Corrosion Behavior of Annealed Nanocrystalline Ni-W Alloys

With a view toward practical applications and fundamental studies, corrosion behavior of nanocrystalline Ni-W alloys exposed to high-temperature environments must be considered. The nanocrystalline structures are unstable and therefore subject to grain growth at elevated temperature. In addition, it has been suggested that the nanocrystalline specimens typically contain non-equilibrium grain boundaries, containing a large number of excess dislocations (Gleiter, 1995: 3; Sanders et al., 1997: 243; Zhang et al., 2001:3485; Hasnaoui, Van Swygenhoven, and Derlet, 2002: 3927). Upon heating, these defects are allowed to annihilate in a process termed “grain boundary relaxation”, which has been observed in coarse-grained (Pumphrey, and Gleiter, 1974: 593; Varin, and Romanowskahaftek, 1986: 1967) and nanocrystalline materials (Jang, and Atzmon, 2006: 083504) through high-resolution TEM. These thermally activated structural changes can potentially alter corrosion behavior of nanocrystalline Ni-W alloys. By careful experimental design, the effects of grain growth and grain boundary relaxation on corrosion behavior of nanocrystalline Ni-W alloys can be investigated.

1.3.3 Interfacial Corrosion Phenomena of As-Deposited and Annealed Nanocrystalline Ni-W Alloys

In this section, we aim to elucidate the interfacial phenomena occurring during corrosion of as-deposited and annealed nanocrystalline Ni-W alloys by means of electrochemical impedance spectroscopy. The insight gained from this section in combination with that from the previous two parts will cast mechanistic light into the corrosion behavior of nanocrystalline Ni-W alloys.

1.4 Benefits of Research

The benefits of this work consist of three main parts: (i) knowledge on corrosion behaviors of nanocrystalline Ni-W alloys will provide insight into the influence of nanometer grain size, crystallographic texture, grain boundary relaxation and alloying element on corrosion properties of nanocrystalline Ni-W alloys, and (ii) the knowledge obtained from this research will assist in the development of manufacturing process, materials selection, and may lead to the fabrication of nanocrystalline Ni-W coating materials with improved performance.

CHAPTER II







LITERATURE SURVEY

2.1 Structure of Nanocrystalline Materials

Nanocrystalline (nc) materials can be classified into nanoparticles and bulk materials. The former are the ultrafine particles with the diameters below 100 nm, while the latter refers to the bulk polycrystalline materials with the grain sizes below 100 nm. Nanoparticles are clusters of atoms built up from a central atom surrounded by full shells of neighboring atoms (Schmidt, 2001: 23). With the decreasing sizes of the nanoparticles, the fraction of surface atoms increases (Table 2-1). Thus, one of the most important characteristics of nanoparticles is their very high surface-to-volume ratios.

In analogy to nanoparticles, bulk nanocrystalline materials exhibit high volume fraction of interfacial atoms. These interfacial atoms are located at grain boundaries and triple junctions. The volume ratio between triple junctions and grain boundaries increases with decreasing grain sizes. Gleiter (Gleiter, 1989: 223) proposed a two-dimensional hard-sphere model for nanocrystalline solids as shown in Fig. 2-1. Two different types of atoms are illustrated in the model, namely, crystalline atoms with periodic lattice arrangement within the grain interior and boundary atoms with random interatomic distances. The crystalline atoms are arranged in a highly ordered configuration, but the boundary atoms are arranged in disordered configurations as evident from the wide variation of the coordination between the nearest neighbor atoms relative to that of atoms inside the grains (Brooks, 1998: 55; Gleiter, 1989: 223).

Table 2-1 The relation between the total number of atoms and the percentage of surface atoms (Schmidt, 2001: 23).

No. of Shell	Atom clusters	Total number of atoms	Surface atoms (%)
1		13	92
2		55	76
3		147	63
4		309	52
5		561	45
7		1415	35

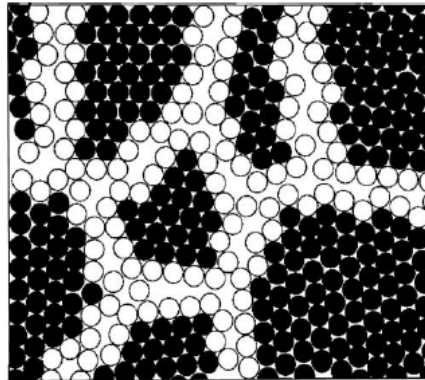


Fig. 2-1 Two-dimensional hard-sphere model of a nanocrystalline solid. The open circles indicate the atoms located at grain boundaries and the solid circles refer to the atoms inside the grains (Gleiter, 1989: 223).

The nanocrystalline structures are metastable structures which may remain stable at ambient temperature and become prone to grain coarsening at elevated temperatures (Klement et al., 1995: 177; Malow, and Koch, 1996: 595; Hibbard et al., 2001: 513; Hibbard et al., 2002: 387; da Silva, and Klement, 2005: 1009). However, the temperature range in which nanocrystalline solids remain stable can be expanded through the addition of suitable alloying elements (Detor, and Schuh, 2007a: 371). Detor et al. has shown that the nanostructure stabilization by alloying elements can be explained by the change in Gibbs free energy G as a function of the grain boundary area A (Detor, and Schuh, 2007a: 372):

$$dG = \gamma dA \quad \text{Eq. 2-1}$$

In a pure metal, the grain boundary energy γ is positive. Therefore, the pure metal lowers its free energy through grain coarsening (i.e., reducing the grain boundary area).

On the contrary, in binary alloys the system energy can be reduced by segregating solute atoms to the grain boundaries so that the boundary energy is lowered according to the following equation:

$$\gamma = \gamma_0 - \Gamma(G_{\text{seg}} + RT\ln X) \quad \text{Eq. 2-2}$$

where γ_0 is the grain boundary energy of pure metal, Γ the specific excess of solute at the grain boundary, G_{seg} the segregation energy, R the gas constant, T temperature and X the global solute composition (Detor, and Schuh, 2007a: 372). For sufficiently high G_{seg} and Γ , according to Eq. 2-2, the grain boundary energy can potentially be reduced to zero, and hence remove the driving force for grain coarsening (Detor, and Schuh, 2007a: 372).

In case of nanocrystalline Ni-W alloys, Detor et al. (Detor, and Schuh, 2007a: 372) has shown that tungsten atoms preferentially segregate to the grain boundaries of Ni-W alloys (Fig. 2-2), and thereby inhibit grain growth by reducing the grain boundary energy of the Ni-W alloys. They pointed out that the stable grain size depends on two competing factors—the grain size and the concentration of alloying element. When the grain size and the alloying element are in balance, we obtain a stable grain size (Detor, and Schuh, 2007a: 372). Based on this principle, it is possible to control nanocrystalline grain size by controlling the concentration of alloying element.

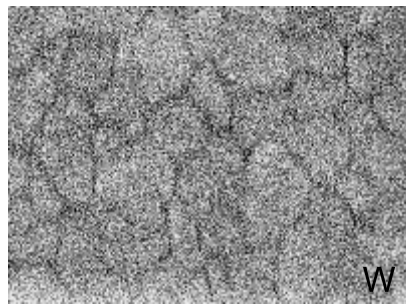


Fig. 2-2 Atomic probe tomography (APT) image showing segregation of tungsten (indicated by black dots) to grain boundaries in a ~ 70 nm x 90 nm x 4 nm section of nanocrystalline Ni-W alloys (Detor, Miller, and Schuh, 2007b: 581).

At elevated temperature, aside from grain growth, the rearrangement of grain boundary structure also commences. Several authors have suggested that the typical processing routes of nanocrystalline materials produce nanocrystalline specimens with metastable grain boundaries which contain high density of excess dislocations (Gleiter, 1995: 3; Sanders et al., 1997: 243; Zhang et al., 2001: 3485; Hasnaoui et al., 2002: 3927). During high temperature annealing, diffusion processes permit these excess boundary dislocations to annihilate in a process termed “grain boundary relaxation”, which has been observed in both coarse-grained (Pumphrey, and Gleiter, 1974: 593; Varin, and Romanowskahaftak, 1986: 1967) and nanocrystalline specimens (Jang, and Atzmon, 2006: 083504). Furthermore, the experimental observation of exothermic heat flow prior to grain growth in various nanocrystalline materials has been attributed to grain boundary relaxation (Eckert et al., 1992: 1751; Tschope, Birringer, and Gleiter, 1992: 5391; Klement et al., 1995: 177; Hibbard et al., 2002: 387; da Silva, and Klement, 2005: 1009).

2.2 Processing of Nanocrystalline Materials

At present, there are various processing methods available for the synthesis of nanocrystalline materials, which possess non-equilibrium structures. These processes include gas condensation, high-energy ball milling, rapid solidification and subsequent annealing, and electrodeposition. An overview of gas condensation and other techniques will be presented below. A discussion of electrodeposition, which is the processing route employed in this dissertation, its advantages over other processing techniques and induced codeposition of Ni-W alloys will be outlined.

2.2.1 Gas Condensation and Other Techniques

Inert gas condensation is the common method used to produce metallic powders with a narrow size distribution. There are, however, several disadvantages, namely, high operating cost, low production rate and highly porous products (75% - 95% density) (Brooks, 1998: 55). As a result, high energy ball-milling, which refines materials through heavy cold work, was developed as an alternative technique. Although this technique is relatively inexpensive and flexible for nanocrystalline materials production, the contamination from the milling media and the atmosphere is hardly avoidable (Brooks, 1998: 57). Another alternative processing method is to rapidly solidify a material into an amorphous structure and subsequently anneal it to obtain a nanocrystalline solid. This technique is, nonetheless, expensive and often produces mixed nanocrystalline and amorphous structures (Brooks, 1998: 59).

It is apparent that the synthesis methods we have discussed thus far all possess some major drawbacks that limit the quality of nanocrystalline materials. For the commercial utilization of nanocrystalline materials to be fully realized, we need to acquire thorough understanding of the relationship between processing, structure, properties and performance of nanocrystalline materials. To achieve this goal, we require an inexpensive and potent processing method that allows precise control of nanostructure and the production of materials with high and consistent quality so that thorough scientific investigation on the mentioned relationship can be conducted. Electrodeposition meets all such qualifications. The details of electrodeposition method will be presented as follows :

2.2.2 Electrodeposition

2.2.2.1 Principles and Advantages

Electrodeposition is an effective method for producing metallic coating on a conductive surface with the use of electrolyte and applied electric current. The deposition of a metallic coating onto a specimen is carried out by immersing the negatively charged specimen into an electrolyte containing a salt of the metal to be deposited, and the specimen becomes a cathode of an electrochemical cell. The metallic ions of the salt will move toward the negatively charged specimen. As the metallic ions arrive at the specimen to be coated, they are reduced into metallic form and deposited onto the specimen.

Compared with other techniques, the advantages of electrodeposition for forming dense nanocrystalline materials are the following. First, it requires simple operation, as the electrodeposition parameters can be tailored to achieve the required crystal grain size, microstructure and chemistry of products. Secondly, it can yield high production rates and be operated at relatively low temperature; hence, the technique is economically feasible. Finally, it possesses high industrial applicability because it involves little modification of existing electroplating technologies.

2.2.2.2 Induced Codeposition of Ni-W Alloys

The term “induced codeposition” was coined by Brenner in 1963, to describe the phenomena where “a metal, which cannot be deposited alone from its aqueous solution, is codeposited in the presence of another metal, forming an alloy”. It is well known that tungsten cannot be electrodeposited alone from an aqueous solution of its salts (Brenner, 1963; Vasko, 1985: 239; Younes, and Gileadi, 2000: 543; Moussa, Ibrahim, and Abd El Rehim, 2006: 333). However, if soluble compounds of iron-group transition metals, namely, Ni, Co or Fe, were added to the plating bath containing tungstate ions (WO_4^{2-}), induced codeposition of tungsten can take place, forming Ni-W, Co-W, or Fe-W alloys (Eliaz, and Gileadi, 2007: 339). A similar phenomenon of induced codeposition is also observed in the plating bath of Mo or Re containing Ni, Co or Fe cations (Brenner, 1963; Vasko, 1985: 239; Eliaz, and Gileadi, 2007: 339).

The ammoniacal citrate bath is widely used for electrodeposition of nanocrystalline Ni-W alloys (Yamasaki et al., 2000: 148; Younes et al., 2002: 100; Schuh,

Nieh, and Iwasaki, 2003a: 431; Somekawa, Nieh, and Higashi, 2004: 1361; Giga, Kimoto, and Takigawa, 2006: 143). The main components of Ni-W bath are nickel sulfate, sodium tungstate, sodium citrate, ammonium chloride, and sodium bromide (Detor, 2007c: 42). Nickel sulfate and sodium tungstate act as the sources of nickel and tungsten metals (Detor, 2007c: 42). Sodium citrate and ammonium chloride serve as complexing agents for Ni and W ions (Detor, 2007c: 42). Sodium bromide was added as the conductive ions that enhance the bath conductivity (Detor, 2007c: 42).

Electrodeposition can be achieved by employing direct (D.C.) or unipolar or bipolar pulsed currents. The advantage of pulsed current over D.C. current is that D.C. plating allows only two controlled variables, either current or voltage, but with pulsed plating, two additional processing parameters, current on-time and off-time, can be independently varied. The variations in pulsed plating parameters can be used to produce materials with structures and properties that are not obtainable by D.C. plating. For instance, pulsed plating significantly improves plating thickness distribution, adherence of deposit to substrate and the density of deposit (Puipe, 1980: 531). Most importantly, in case of nanocrystalline Ni-W alloys, bipolar pulsing can promote grain refinement via the control of tungsten content in the alloys (Detor, and Schuh, 2007a: 371).

Bipolar pulsing involves periodically applying the reverse current in the electrodeposition process. During the reverse current, the anode and cathode are in fact swapped (Detor, 2007c: 42). The variables of bipolar pulsing are illustrated in the bipolar waveform (Fig. 2-3), which includes forward and reverse current density (Fwd

C.D. and Rev C.D.), forward and reverse on-time (Fwd t_{on} and Rev t_{on} , respectively) and off-time (t_{off}). Reverse pulsed electrodeposition has several benefits. First, it may efficiently strip off contaminating elements such as hydrogen from the deposit (Chassaing, Roumegas, and Trichet, 1995: 667). Second, it may reduce the stress levels (Aroyo, and Tzonev, 2003: 50) and the surface roughness (Qu, Chan, and Zhu, 1997: 220; Aroyo, and Tzonev, 2002: 48) of the deposit.

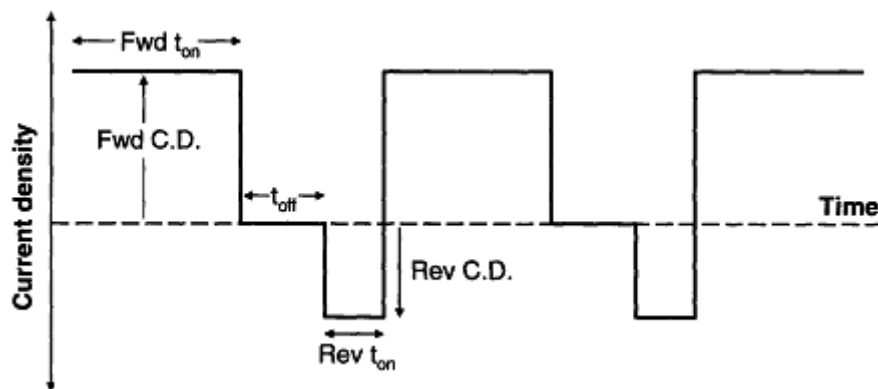


Fig. 2-3 Definition of variables that control the shape of the applied current waveform used in electrodeposition experiments (Detor, 2007c: 45).

Although the elucidation of electrochemical phenomena occurring during reverse pulsed electrodeposition is not the main focus of this thesis, referring to the standard half-cell potentials (Vasko, 1985: 239; Vanysek, 2006: 534) reported in the literature should offer some qualitative insight into the possible mechanisms taking place during reverse pulsing. The relevant half-cell potentials of the reactions expected for electrodeposition of Ni-W alloys (Vasko, 1985: 239; Vanysek, 2006: 534) are shown in Table 2-2. Consulting these standard half-cell potentials may cast some light into the

electrochemical phenomena during reverse pulsing. First, according to Table 2-2, during the forward pulse, pure Ni, which has a higher half-cell potential, should be preferentially deposited, and W, with its lower half-cell potential, will not be deposited in any appreciable amount (Detor, 2007c: 42). However, by adding sodium citrate and ammonium chloride as complexing agents, the half-cell potentials of Ni and W were brought close together, through the formation of Ni-W complex ions (Detor, 2007c: 42). The Ni-W complex ions were then reduced on the cathode surface and deposited as Ni-W alloys (Detor, 2007c: 42).

Table 2-2 Standard half-cell potentials for WO_4^{2-} , H^+ and Ni^{2+} ions. The equilibrium values suggest that W is preferentially removed from the deposit surface during the reverse (anodic) pulse (Detor, 2007c: 47).

Reaction	Standard potential, E° (volts vs. SHE)
$2\text{H}^+ + 2\text{e}^- \rightleftharpoons \text{H}_2$	0.0
$\text{Ni}^{2+} + 2\text{e}^- \rightleftharpoons \text{Ni}$	-0.257
$\text{WO}_4^{2-} + 4\text{H}_2\text{O} + 6\text{e}^- \rightleftharpoons \text{W} + 8\text{OH}^-$	-1.074

Second, during the reverse pulse, tungsten, which has a lower half-cell potential than Ni, is preferentially stripped off from the Ni-W deposit, leading to the reduction of tungsten content in Ni-W alloys (Detor, 2007c: 42). This suggests that the alloy composition and the structural characteristics affected by alloy composition can be tailored by controlling the reverse current. In fact, a group of researchers (Detor, and Schuh, 2007a: 371) have successfully employed reverse pulsing technique to produce Ni-W alloys with tailored

composition and grain size.

Moreover, the reverse pulsing technique can produce nanocrystalline Ni-W deposits of superior quality to those produced by conventional D.C. electrodeposition, as illustrated in the SEM micrographs of Fig. 2-4. It is evident that the D.C. technique produces defective electrodeposit with voids and cracks (Detor, 2007c: 48). In contrast, the deposit produced by reverse pulsing control is free from defects. Such high quality deposit is typical of those achieved through the reverse pulsing method.

With its aforementioned advantages, the reverse pulsing technique has been demonstrated as the synthetic method of choice for the production of Ni-W specimens with tailored composition. It should now become apparent that not only can a broad spectrum of W contents be achieved through proper selection of the applied current waveform, but the resulting deposits also possess high quality, fitting for the investigation of corrosion properties.

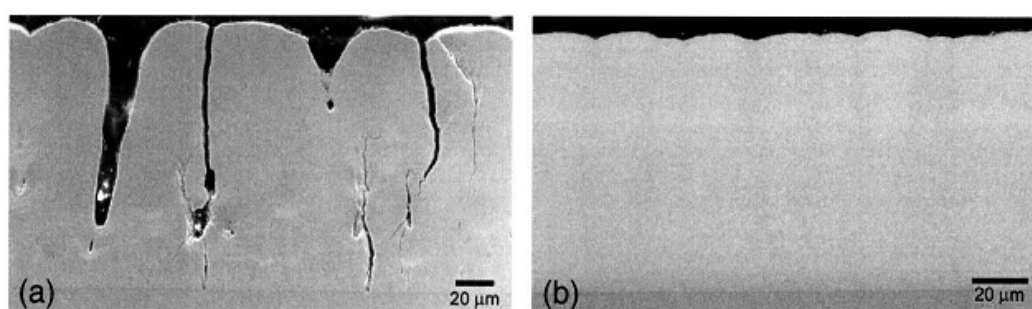


Fig. 2-4 Cross-sectional SEM micrographs of nanocrystalline Ni-W specimens prepared by (a) conventional D.C. electrodeposition and (b) reverse pulsing control; both specimens have nominally the same composition of ~8 at.%W (Detor, and Schuh, 2007a: 371).

2.3 Properties of Nanocrystalline Materials

The behavior of nanocrystalline materials generally deviate from those of microcrystalline counterparts. Their unique properties are normally attributed to the high surface-to-volume ratio or the large volume fraction of the grain boundaries and triple junctions. These properties may not be predictable from the understanding of the amorphous or the coarse-grained materials with the same chemical composition. In this section, we review some recent studies on properties of nanocrystalline materials that are pertinent to this work.

2.3.1 Mechanical Behavior

One of the outstanding properties of nanocrystalline materials is their improved mechanical strength. Polycrystalline metallic systems exhibit an increase in yield strength (σ_y) with the reduction of grain size (d) according to the Hall-Petch equation:

$$\sigma_y = \sigma_0 + kd^{-1/2} \quad \text{Eq. 2-3}$$

where σ_0 is the stress resisting the gliding movement of dislocations, and k is the Hall-Petch slope which indicates the hindering effect of the grain boundary to the dislocation motion (Tjong, and Chen, 2004: 22). Likewise, hardness (H_v), which is a measure of the resistance of a material to plastic deformation under the application of indenting load, can be related to the grain size by:

$$H_v = H_0 + k_H d^{-1/2} \quad \text{Eq. 2-4}$$

where H_0 and k_H are constants (Tjong, and Chen, 2004: 22). The Hall-Petch effect results from the grain boundaries acting as obstacles to the movement of dislocations.

Consequently, dislocations can be piled up against a grain boundary inside a grain. As grains shrink in size, the volume fraction of grain boundaries will increase and the dislocation pileup will be enhanced, leading to the increased strength and hardness relative to coarser-grained materials with the identical chemical composition. Trelewicz et al. (Trelewicz, and Schuh, 2007: 5948) pointed out that as the grain size decreases below ~500 nm, the dislocations are nucleated solely from grain boundary sources (Van Swygenhoven, Derlet, and Froseth, 2004: 399; Wu, Zhu, and Ma, 2006: 121905). They (Trelewicz, and Schuh, 2007: 5948) argued that at the very fine grain size below ~20 nm, the plasticity is confined at grain boundary (Schiotz et al., 1999: 11971; Van Swygenhoven et al. 1999: 22; Farkas et al., 2006: 695). They (Trelewicz, and Schuh, 2007: 5948) also noted that many researchers have connected this transition in deformation mechanisms with Hall-Petch breakdown (Schiotz, and Jacobsen, 2003: 1357; Yamokov et al., 2003: 385; Zhu, and Langdon, 2005: 234). In addition, as grain size is reduced further to the finest size approaching the amorphous limit, they (Trelewicz, and Schuh, 2007: 5949) have demonstrated that the breakdown in Hall-Petch strengthening now corresponds to a transition from grain-boundary confined mechanisms in fine-grained nanocrystalline metals to shear banding in amorphous metals.

The previous paragraph discussed mechanical behavior from micrometer to the finest nanometer length scale at ambient temperature. Nevertheless, with a view toward applications, mechanical behavior at elevated temperature should as well be discussed. It has been demonstrated that thermal annealing can alter mechanical

behavior of nanocrystalline metals through grain growth and grain boundary relaxation. The effect of grain growth can be explained by Hall-Petch relation as discussed in the previous paragraph. As for grain boundary relaxation, there are several groups of researchers showing the connection of this process with strengthening. Among them, Weertman (Weertman, 1993: 161) observed that thermally annealed samples frequently exhibit a much higher hardness than their as-processed counterparts. Asaro et al. proposed that at very fine grain size, plasticity is actually induced by the emission of dislocations from grain boundary sources (Asaro, and Suresh, 2005: 3369). Provided that this is true, Trelewicz (Trelewicz 2008: 93) has theorized that annihilation of excess grain boundary dislocations through thermal annealing should decrease the number of sources for nucleation of intragranular dislocations. He (Trelewicz 2008: 93) further suggested that without competing mechanisms, the reduction of nucleation sources would increase the critical shear stress that is required to initiate slip, leading to the enhanced strengthening observed upon grain boundary relaxation.

In this light, it is apparent that even in the absence of grain growth, the change in grain boundary structure upon relaxation, can have a significant impact on macroscopic properties of materials, especially for extremely fine-grained materials consisting of large intercrystalline volume. Consequently, grain boundary relaxation should be included as an additional variable in the investigation of corrosion properties of nanocrystalline materials.

2.3.2 Corrosion Behavior

Corrosion of various nanocrystalline metal systems have been investigated and reported in the literature; however, no conclusive trend of corrosion behavior can be drawn with different authors suggesting seemingly contradictory behaviors. Some authors reported the beneficial effect of large grain size on the corrosion resistance of materials. For example, El-Moneim and colleagues (El-Moneim et al., 2002a: 1097, 2002b: 1857, 2002c: 121) demonstrated that in deaerated 0.1 M H_2SO_4 solution, the corrosion rate of the hot-pressed 100-nm NdFeB magnet produced from melt-spun materials was significantly higher than that its annealed counterpart with a mean grain size of 600 nm. In the same manner, Luo and co-workers (Luo, Qian, and Wu, 2007: 524) suggested that in 0.1 M CuSO_4 + 0.05 M H_2SO_4 electrolyte, relative to coarse-grained copper, nanocrystalline copper produced by inert gas condensation and warm compress (IGCWC) showed a decreased corrosion resistance which was mainly attributed to the high activity of surface atoms and intergranular atoms. However, other groups of researchers demonstrated that nanocrystalline grain size actually enhances the corrosion resistance of materials. Among them are Lu and colleagues (Lu et al., 2006: 197) as well as Meng and co-workers (Meng, Li, and Wang, 2006: 4277). Lu et al. has shown that in 0.1-1.0 M aqueous HCl solutions, the magnetron sputtered nanocrystalline Cu-20Zr film has an improved corrosion resistance relative to the cast Cu-20Zr alloy due to the formation of Cu-rich layer at corrosion potential. While Meng et al. has demonstrated that in 0.05 M H_2SO_4 + 0.25 M Na_2SO_4 solution, the magnetron sputtered Fe-10Cr nanocrystalline coatings (20-30 nm grain size) has higher corrosion

resistance than cast Fe-10Cr alloy due to the enhanced formation of chrome oxide passive film through large number of intercrystalline diffusion paths for Cr. Finally, to make the corrosion trend even more inconclusive, Yu and co-workers (Yu, Wu, and Erb, 2007: 353) have shown that grain size reduction has little effect on the potentiodynamic polarization responses of electrodeposited nanocrystalline, ultra-fine grained and coarse-grained polycrystalline copper foils in 0.1 M NaOH solution.

The discrepancy in the corrosion behavior of nanocrystalline materials reported in the literature as mentioned above may be attributed to, first, the variation in processing methods among different research groups and, second, the failure to consider the effect of grain boundary relaxation upon annealing when annealed specimens are investigated. Aside from the different grain sizes, the different types of defects and microstructures inherent in each processing method may be introduced into the materials and cause the variation of corrosion behavior in the materials of identical composition. Moreover, the production of coarse-grained materials by annealing the fine-grained counterparts will produce grain boundary relaxation as well as grain growth. For nanocrystalline materials, the impact of grain boundary relaxation on properties can be significant due to their large intercrystalline volume fraction. Consequently, unless the effect of grain boundary relaxation is properly included in the analysis of corrosion data, the results of corrosion investigation can be misinterpreted, potentially causing the discrepancy in corrosion behavior of nanocrystalline materials reported in the literature.

To eliminate the potential sources of variation in corrosion data, in this thesis, we employ only one processing method, electrodeposition, for the synthesis of all test

specimens to ensure that the variation of defects and structural characteristics are kept to the minimum in all test specimens. Furthermore, the effect of grain boundary relaxation is included in the analysis of corrosion data when the test specimens are produced from thermal annealing of finer-grained nanocrystalline specimens.

As discussed previously, the corrosion behaviors of nanocrystalline alloys reported in the literature remain inconclusive. Nonetheless, several factors that could contribute to the corrosion properties of nanocrystalline materials can be highlighted. These factors include (i) passive film, (ii) grain size, (iii) alloying elements, (iv) crystallographic texture and (v) grain boundary relaxation. Of five factors, only the first four will be reviewed here because to the author's best knowledge, the effect of grain boundary relaxation on corrosion of nanocrystalline alloys has never been explicitly investigated in the literature.

2.3.2.1 Effect of Passive Film

The high fraction of grain boundaries in nanocrystalline materials provides an increased number of active sites for surface reactions. Wang et al. has demonstrated that in NaOH or NaCl solutions, where the passive process occurs on the surface, the nanocrystalline Co is more resistant to corrosion than coarse-grained Co coating because the high grain boundary density in nanocrystalline Co promotes the formation of a stable and protective surface film (Wang et al., 2007: 4342). Nevertheless, they also showed that in HCl or H₂SO₄ solutions, with no apparent passivation process, high grain boundary density in nanocrystalline Co helps accelerate corrosion by providing high

density of active sites for preferential attack.

Similar dependence of corrosion behavior on pH has also been demonstrated for electrodeposited Ni coating (16 nm to 2 μm). Results show that in NaOH or NaCl solutions, nanocrystalline Ni possesses enhanced corrosion resistance with the reduction of grain size (Qin, Lian, and Jian, 2010: 82). However, in H_2SO_4 solution, the higher grain boundary density accelerates corrosion due to the absence of passive process, leading to diminishing corrosion resistance with finer grain size (Qin, Lian, and Jian, 2010: 82).

As a result, the passive film formation seems to be a dominating factor that determines whether the higher grain boundary density will hinder or accelerate corrosion (Wang et al., 2007: 4342). Moreover, the passive film of nanocrystalline materials is attacked more uniformly. Consequently, nanocrystalline materials are more resistant to localized corrosion than the coarse-grained materials of similar alloy system.

The dominating influence of passive film on corrosion behaviors of nanocrystalline materials will become more apparent in the subsequent paragraphs as the readers see that even grain size and alloying element affect the corrosion behaviors of nanocrystalline materials mainly through their impact on the formation, the composition and the properties of passive film.

2.3.2.2 Effect of Grain Size

Wang and colleagues (Wang et al., 2006: 657) reported that the corrosion resistance of Ni coatings in alkaline solutions considerably increased as the grain size

decreased from microcrystalline to nanocrystalline regime. The higher corrosion resistance of nanocrystalline Ni may be due to the quicker formation of continuous Ni(OH)_2 passive film relative to coarse-grained Ni coatings. It is believed that nanocrystalline Ni coatings have a high density of nucleation sites and thereby possess a high fraction of passive layers and low corrosion rates. Moreover, according to Youssef and co-workers (Youssef, Koch, and Fedkiw, 2004: 51), the passive film formation on the corroded surface is diffusion controlled. Consequently, the passive layers on nanocrystalline materials are more continuous than those on the coarse-grained substances because nanocrystalline materials provide a large quantity of grain boundaries that serve as diffusion paths for elements to migrate to the surface.

2.3.2.3 Effect of Alloying Element

Sriraman et al. showed that in 3.5 wt.% NaCl solution, the corrosion resistance of nanocrystalline Ni-W alloys increased with tungsten concentration up to 7.54 at.% and then decreased (Sriraman et al., 2007a: 39). For nanocrystalline Ni-Fe-W alloys in the same solution, they demonstrated that the corrosion resistance increased with tungsten content up to 9.20 at.% and then decreased (Sriraman et al., 2007a: 39). Nanocrystalline Ni-Fe-W alloys exhibited poorer corrosion resistance due to preferential dissolution of Fe into the test solution. Regardless of composition, all the alloys showed passive behavior over a broad range of potentials due to the formation of W-rich film on the surface. The W-rich film protected the alloys from further corrosion (Sriraman et al., 2007a: 39).

2.3.2.4 Effect of Crystallographic Texture

Although crystallographic texture has been demonstrated to have an impact on corrosion behavior of many metallic systems (Park, and Szpunar, 1998: 525; Ramanauskas, 1999: 53; Garcia et al., 2003: 1173; Schuh et al., 2003b: 183; Ramanauskas et al., 2007: 1801; Hassini et al., 2009: 2371), with respect to theme of this thesis, the emphasis is put on the nickel alloy systems. Among many authors, Garcia and colleagues (Garcia et al., 2003: 1173) investigated the effect of texture modification on corrosion behavior of the electrodeposited Ni coating. The codeposition of 5-8 vol.% 0.3 μm SiC-particles during the nickel electrodeposition leads to the transition from the columnar nickel grains with mixed $\{211\}$ and $\{100\}$ fiber texture to the fine equiaxed nickel grains with random crystallographic texture. This randomly oriented equiaxed microstructure leads to a better corrosion resistance and a lower internal stress in nickel coatings. Moreover, crystallographic texture can be modified from $\{200\}$ to $\{111\}$ through addition of saccharin into the Ni electroplating bath (Hassani et al., 2009: 2371). In combination with the smoothed surface due to finer grain size, this transition of texture can potentially increase the corrosion resistance of electrodeposited Ni coatings (Hassani et al., 2009: 2371). Casting more light on the impact of crystallographic texture on corrosion, Schuh and co-workers (Schuh et al., 2003b: 183) showed that the corrosion rate of Inconel 600 in diluted HCl solution increases as the crystallographic texture diverges from close-packed $\{111\}$. This anisotropy in corrosion rate is the net consequence of anisotropic dissolution and anisotropic oxide composition, thickness, and stability of different crystallographic planes (Schuh et al., 2003b: 183).

2.4 Nanocrystalline Ni-W Alloys

2.4.1 A Potential Replacement for Hard Chrome Coating

Chromium coatings have been used in a wide range of industries— aerospace, automotive, and others—because of the high hardness and good corrosion resistance. However, the chromium plating industry has encountered increasing difficulty in recent years. Increasing number of regulations, which has been designed to protect the population against the health and environmental hazards of hexavalent chromium, have increased the burdens for the factories offering plating services (Tjong, and Chen, 2004: 22). The quest for chromium replacement thus becomes an active research topic in both industrial and scientific communities (Tjong, and Chen, 2004: 22).

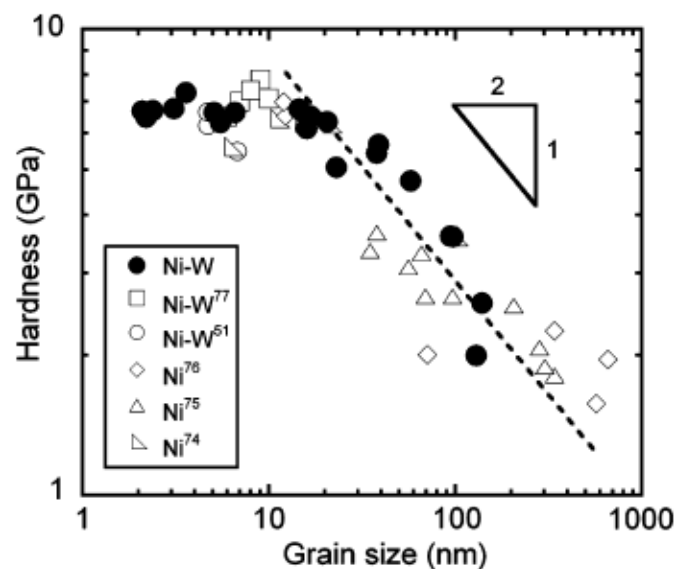


Fig. 2-5 A graph showing the relationship between the hardness and grain size of Ni-W alloys (Detor, and Schuh, 2007a: 371).

Nanocrystalline Ni-W alloy coatings possess the high hardness and protective surface oxide film, but less environmental and health hazards, and thereby become the potential replacement for chromium coatings. Fig. 2-5 shows the relationship between the hardness and grain size of Ni-W alloys. As the grain size decreases from 1 μm to 10 nm, the hardness increases from 1 GPa to 7 GPa, a sevenfold increase in hardness due to nanocrystallization. Upon thermal annealing, the impact of grain boundary relaxation further increases the hardness of annealed Ni-W alloys approaching that of chromium coating, making nanocrystalline Ni-W coating a strong candidate as the substitute for chromium coating in industrial applications (Detor, 2007c; de Lima-Neto et al., 2010: 2078).

In addition to high hardness, nanocrystalline Ni-W alloys also exhibit promising corrosion properties. Fig. 2-6 shows the polarization curves of nanocrystalline Ni-W alloys with the following W concentrations and corresponding grain sizes: 2.43 at.% (20 nm), 7.54 at.% (15 nm), 9.82 at.% (10 nm), 16.06 at.% (5 nm). It is apparent that the grain size of Ni-W alloys decreases as the concentration of W increases. It is also evident from Fig. 2-6 that the passive current density decreases with increasing W concentration (or decreasing grain size). Consequently, it can be inferred that the protectiveness of passive film of nanocrystalline Ni-W alloys increases as the grain size decreases.

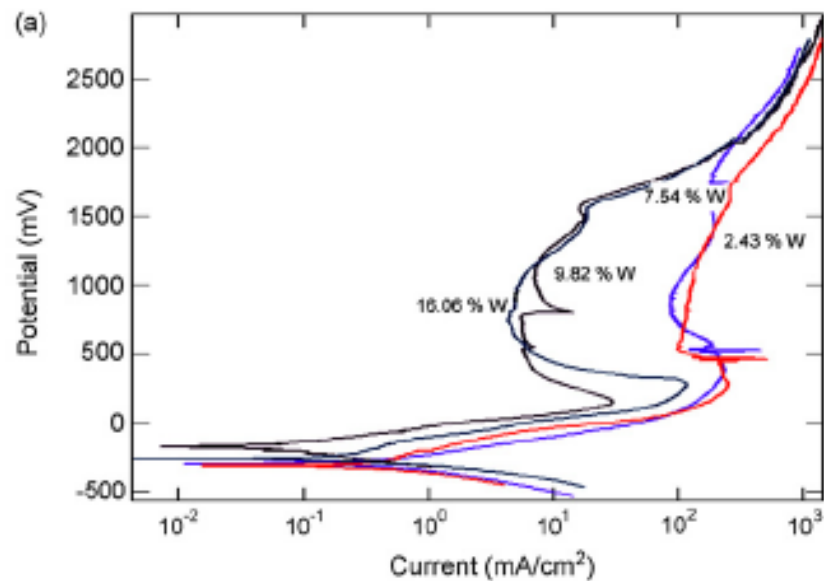


Fig. 2-6 Polarization curves of nanocrystalline Ni-W alloys with different W contents in 1 N sulfuric acid (Sriraman et al., 2007a: 39).

From the above discussion, it is evident that nc Ni-W alloys show promise as an industrial coating. Before this alloy can be applied as coating effectively, however, its mechanical and corrosion properties need to be fully characterized. While large amount of works have concentrated on mechanical properties of nanocrystalline alloys, the study on corrosion properties is still limited.

2.4.2 Corrosion Behavior of Nanocrystalline Ni-W Alloys

Recently, nc Ni alloys containing tungsten (W) as an alloying element for grain size control were developed (Yamasaki et al., 2000: 148; Detor, and Schuh, 2007a: 371; Boonyongmaneerat et al., 2009: 3590). They have found increasing use in several applications, including as barrier coatings in electronics and for wear protection on

engineering components, owing to their superior strength and thermal stability, as well as ease of grain size control during processing (Slavcheva et al., 2005: 5573; Sriraman et al., 2006: 303; Detor, and Schuh, 2007d: 3233; Sriraman et al., 2007b: 715; Haseeb et al., Wear 2008: 106). While mechanical integrity has been a main subject of attention, more interest has recently been placed on the corrosion behaviour of nc Ni and related alloys. For many applications, such as protective automotive coatings and electrical contact components, corrosion damage of the Ni layers can result in cosmetic defects, development of cracks or pores, and ultimately malfunction of the components (Erb et al., 2007: 235). Since even minimal corrosion can have adverse effects, understanding the corrosion behaviour of nc Ni and nc alloys in general, is of immediate practical importance.

Prior studies have shown that the corrosion behaviour of nc Ni is rather distinct from that of its microcrystalline (mc) nickel counterpart, although the number of systematic studies on this topic is relatively few, and no broad agreement has yet emerged. For example, Wang and co-workers (Wang et al., 2006: 657) found that unlike mc Ni, nc Ni was passivated in 10 wt.% NaOH solution. Moreover, Ni showed an increasing corrosion current density (i_{corr}) with an increase of grain size from 16 nm to 3 μm . In 1 M H_2SO_4 , Mishra and colleague (Mishra, and Balasubramaniam, 2004: 3019) also reported that the corrosion rate of Ni decreased as grain size was decreased to the nanometer regime. Qin and co-workers (Qin et al., 2010: 82), however, recorded somewhat different responses; while finding that in 10 wt.% NaOH and 3 wt.% NaCl solutions nc Ni (16 - 258 nm grain size) exhibited lower values of both i_{corr} and the

passive current density (i_{pass}) as compared to mc Ni, the authors suggested that in 1 wt.% H_2SO_4 solution, the corrosion rate of nc Ni increased with decreasing grain size, which was not found to promote the passivation process. Although the overall picture of corrosion behaviour of nc Ni remains inconclusive from such works, it is certainly interesting that every study described above reports significant effects of a nanocrystalline structure.

In the case of nc Ni-W alloys, we again find only a limited number of published studies on corrosion behaviour (Yang et al., 2004: 228; Sriraman et al., 2007a: 39; Alimadadi et al., 2009: 1356). Sriraman and co-workers (Sriraman et al., 2007a: 39) focused their study on the effect of nanocrystalline grain size on corrosion of Ni-W alloys. They reported that, in 3.5 wt.% NaCl solution, the i_{corr} of nc Ni-W (5-40 nm) decreased as the grain size decreased to 15 nm, and then increased again slightly as the grain size reduced further to 5 nm. Alimadadi et al. (Alimadadi et al., 2009: 1356) showed that in 3.5 wt.% NaCl, the polarisation resistance of Ni-W alloys generally decreased with W content (0-25.7at.%) and with the reduction of crack density. Yang et al. (Yang et al., 2004: 228) reported that an application of heat treatment at 400 °C for 1 hour increased i_{corr} and the corrosion potential (E_{corr}) of nc Ni-W alloy in 3 wt.% NaCl, presumably due to grain boundary relaxation upon heat treatment. In a more engineering-oriented work, Jones et al. (Jones et al., 2010: 52) reported that nc Ni-W coatings could effectively shield steel substrates from corrosion in standard neutral salt spray testing.

CHAPTER III

EXPERIMENTAL PROCEDURE

This section is divided into three parts including Part I – Corrosion of As-Deposited Nanocrystalline Ni-W, Part II – Corrosion of Annealed Nanocrystalline Ni-W and Part III – Interfacial Corrosion Phenomena of As-Deposited and Annealed Nanocrystalline Ni-W.

Part I – Corrosion of As-Deposited Nanocrystalline Ni-W

In this part, the corrosion properties of as-deposited nanocrystalline Ni-W alloys were investigated in 3.5 wt.% NaCl solutions with pH of 10 and 3, which are representative of corrosive environments of relevance to many engineering applications. Reverse pulse electrodeposition is employed as a technique to systematically fabricate nanocrystalline Ni-W alloys of various grain sizes and tungsten content. For comparison purposes, the corrosion behaviour of as-deposited microcrystalline (mc) Ni is also examined under the same conditions by potentiodynamic polarization technique.

1 Electrodeposition

Electrodeposition is one of the most promising methods for the production of nanocrystalline alloys, owing to its ability to synthesize homogeneous, high-quality specimens with controllable grain size and alloy composition (Detor, and Schuh, 2007a: 371). In this part, Ni and Ni-W alloy specimens were prepared on copper substrate by electrodeposition using a pulse rectifier (DuPR10-3-6w/M-2 μ STAR) in an experimental

setup as shown in Fig. 3-1. Platinum and a resin mounted copper coupon ($1.5 \times 2 \text{ cm}^2$), polished to a mirror-like finish and activated by 10 vol.% H_2SO_4 , were used as an anode

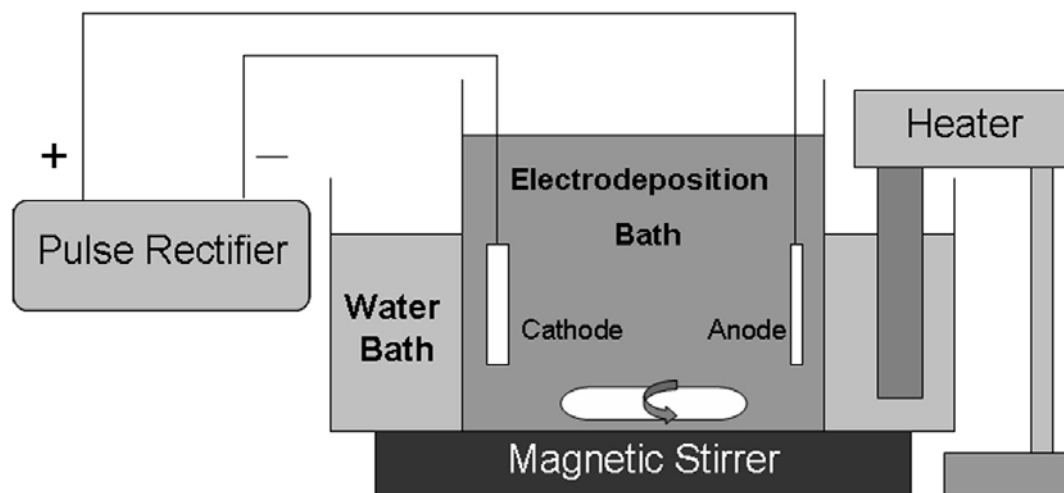


Fig. 3-1 Schematic diagram of the electrodeposition set-up used to produce nanocrystalline Ni-W alloys (Detor, 2007c: 42).

and a cathode, respectively. The Ni bath consisted of 300 g/l $\text{NiSO}_4 \cdot 6\text{H}_2\text{O}$, 45 g/l NiCl_2 and 45 g/l H_3BO_3 (Sa-nguanmoo et al., 2011: 122), and the Ni-W bath contained 147 g/l $\text{Na}_3\text{C}_6\text{H}_5\text{O}_7 \cdot 2\text{H}_2\text{O}$, 26.7 g/l NH_4Cl , 15.8 g/l $\text{NiSO}_4 \cdot 6\text{H}_2\text{O}$, 46.2 g/l $\text{Na}_2\text{WO}_4 \cdot 2\text{H}_2\text{O}$ and 15.5 g/l NaBr (Detor, 2007c: 45). The bath temperature was 75°C in each case, and the plating duration was controlled at 60 minutes. Plating was conducted in a 400 cm^3 beaker, with a magnetic bar stirrer continuously rotating at 250 rpm. Ni-W alloys were fabricated using the bipolar pulsed current (reverse pulsing mode) to control the content of tungsten and thus the grain size (Detor, and Schuh, 2007a: 371; Obradovic et al., 2006: 4201). Here, a forward current density (Fwd C.D.) of 0.20 A/cm^2 and reverse current densities (Rev C.D.) of 0, 0.10, 0.15, 0.20 and 0.30 A/cm^2 were employed. The

forward (Fwd t_{on}) and reverse current on-times (Rev t_{on}) were maintained at 20 ms and 3 ms, respectively, followed the same procedure as Detor and colleagues (Detor, and Schuh, 2007: 371). Ni was also electrodeposited using the same rectangular current waveform, having a 20-ms forward current density of 0.10 A/cm^2 , and 3-ms reverse current density of 0 A/cm^2 . The rectangular current waveform for electrodeposition of Ni and Ni-W alloys is shown in Fig. 3-2.

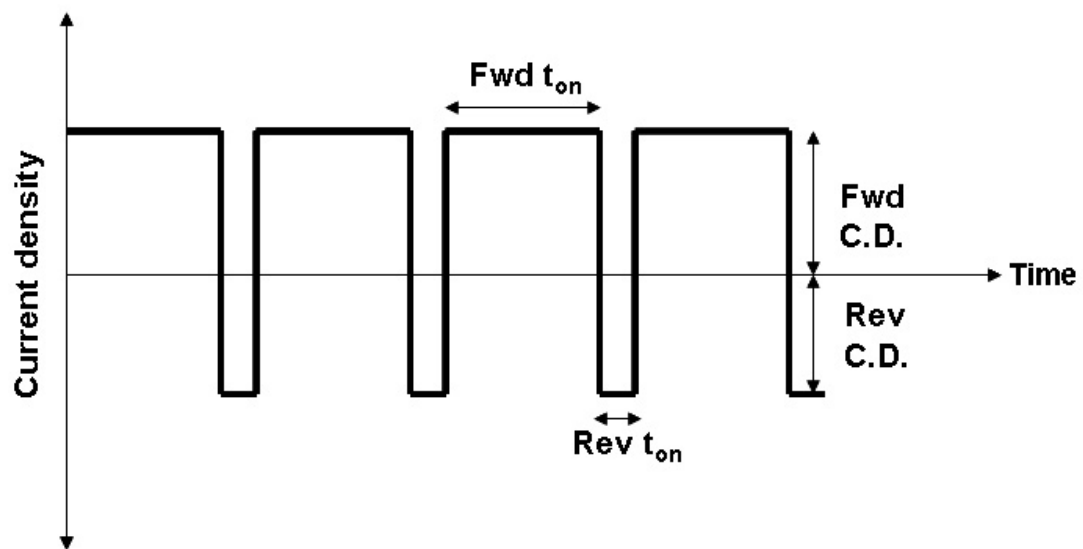


Fig. 3-2 The rectangular current waveform used for reverse pulsed electrodeposition of Ni and Ni-W alloys. The electrodeposition parameters include forward current density (Fwd C.D.), reverse current density (Rev C.D.), forward current on-time (Fwd t_{on}) and reverse current on-time (Rev t_{on}).

2 Characterization

In Part I, the goal is to investigate the interrelationships between tungsten content, grain size, crystallographic texture, surface morphology and composition on the

corrosion properties of as-deposited nanocrystalline Ni-W. Energy dispersive spectroscopy (EDS) was employed to measure tungsten content. X-ray Integral Breadth and Line Intercept Methods were used to determine the grain size in nanometer and micrometer regimes. The crystallographic textures of selected Ni-W specimens were characterized by XRD pole figures. Finally, the surface morphology and composition of selected Ni-W specimens were characterized by scanning electron microscopy (SEM) and X-ray photoelectron spectroscopy (XPS). All characterization procedures were performed on selected specimens prior to corrosion test.

2.1 Tungsten Content

Tungsten contents of representative specimens were the average value of nine EDS (EDAX LEAP) measurements taken at nine positions on each sample as shown in Fig. 3-3. All EDS spectra were acquired for 60 seconds at 1000x magnification and electron beam energy of 20 keV.

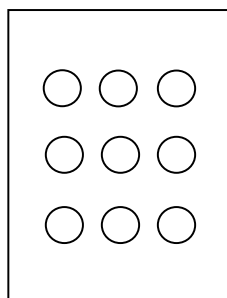


Fig. 3-3 Positions of EDS analysis and hardness measurement on each Ni-W specimen.

2.2 Grain Size

2.2.1 Measurement of Nanocrystalline Grain Size

The grain size in nanometer regime was calculated from XRD peak broadening by Integral Breadth Method (Zhang, Zhou, and Lavernia, 2003: 1349) which is capable to measuring extremely small grain size up to 100 nm. The steps of X-ray Integral Breadth Method are given as follows:

a) Perform continuous XRD scan on a Ni-W specimen in the 2θ range from 20° - 100° with the step size of 0.02° per second at the X-ray wavelength of 0.154 nm.

b) Perform continuous XRD scan on coarse-grained LaB_6 powder standard in the 2θ range from 20° - 100° with the step size of 0.02° per second at the X-ray wavelength of 0.154 nm.

c) Measure the FWHM (full width half maximum) values of each X-ray peak of a Ni-W specimen. This yields a set of experimental broadening values, B_{exp} , associated with each characteristic diffracting angle (θ_0) of the Ni-W specimen.

d) Measure the FWHM (full width half maximum) values of each X-ray peak of coarse-grained LaB_6 powder standard. Calculate the equation describing the relationship between FWHM values and associated characteristic diffracting angles of the standard. From the equation just determined, calculate the FWHM values with respect to each characteristic diffracting angle (θ_0) of the Ni-W specimen. This yields a set of instrumental broadening values, B_{ins} , of the XRD instrument with respect to θ_0 of the Ni-W specimen.

e) The integral breadth, β , can be calculated using Cauchy-Gaussian (CG) relationship as follows:

$$\text{CG relationship: } \beta = B_{\text{exp}} - [(B_{\text{ins}})^2 / B_{\text{exp}}] \quad \text{Eq. 3-1}$$

f) Plot the following equation in linear form

$$\beta^2 / \tan^2 \theta_0 = (1 / L)(K\lambda\beta / \tan \theta_0 \sin \theta_0) + C \quad \text{Eq. 3-2}$$

by equating

$$y = \beta^2 / \tan^2 \theta_0$$

$$m = 1 / L$$

$$x = K\lambda\beta / \tan \theta_0 \sin \theta_0$$

$$C = C$$

Where

$$K = 0.94 \text{ (Klug et al., 1974: 618)}$$

$$\lambda = \text{X-ray wavelength} = 0.154 \text{ nm}$$

$$L = \text{grain size or crystallite size}$$

g) Grain size can be obtained by taking the inverse value of linear slope, m , of Equation 3-2.

2.2.2 Measurement of Microcrystalline Grain Size

SEM (Phillips XL30CP) and line intercept method are used to measure microcrystalline grain size. The steps to this procedure, which are derived from ASTM E112 Standard, are given here:

a) On a single field of view, randomly place one or more straight test lines of known combined total length, L . The total length of the test lines in a single field of view should be such that at least 50 intersections can be counted. An intersection is the point

where the test line cuts a grain boundary.

b) Count the total number of intersections, 1 for each intersection, 1 for each tangential intersection, $\frac{1}{2}$ when an end of the test line ends exactly on a grain boundary and $1\frac{1}{2}$ when the intersection occurs at a triple point.

c) Make counts on 5 randomly selected and widely separate fields of view to obtain a reasonable average for the specimen.

d) For equiaxed grains, the average grain size can be obtained from Equation 3-3.

$$\text{Average grain size} = (1.5 \times L_T) / (P \times M) \quad \text{Eq. 3-3}$$

where L_T is the combined total length of the test lines from all fields of view, P is the total number of intersections and M is the magnification.

Example

Suppose that 5 fields of view, at 1,000x, were used for the measurements resulting in the following data.

Field of view	Test line length (mm)	Number of intercepts
1	337	71
2	216	55
3	402	89
4	529	113
5	395	81
Total	1879	409

From the table, calculate the average grain size:

$$\text{Average grain size} = (1.5 \times 1879 \text{ mm}) / (409 \times 1,000) = 6.9 \times 10^{-3} \text{ mm} = 6.9 \mu\text{m}$$

2.3 Crystallographic Texture

The x-ray diffraction pole figures of selected as-deposited and annealed Ni-W specimens were measured in polar angles from 0° to 90° and angular angles from 0° to 360° with 5° sampling intervals using the reflection technique (Rigaku x-ray diffractometer model TTRAX-III). The x-ray diffraction data of {111} and {200} poles of selected as-deposited Ni-W samples were collected.

2.4 Surface Morphology and Composition

Optical microscope (Carl Zeiss) was used to image the surface morphology of Ni-W specimens before and after potentiodynamic test. Scanning electron microscope (Phillips XL30CP) was employed to image the surface morphology of Ni-W specimens before potentiodynamic test.

For characterization of surface film composition, the as-deposited Ni-W specimens were ultrasonically cleaned in soap solution, then double distilled water and in acetone and exposed to ambient atmosphere for at least 48 hours to allow new surface film to form. After that, prior to any electrochemical test, an Axis Ultra x-ray photoelectron spectroscopy (XPS) system (Kratos Analytical of Manchester, England) using monochromatic Al K_{α} radiation was used to characterise the surface film on annealed Ni-W specimens.

3 Potentiodynamic Polarization

Electrochemical corrosion behaviours of as-deposited nanocrystalline Ni-W alloys were examined by means of potentiodynamic polarization technique. The schematic diagram for the experimental setup is illustrated in Fig. 3-4. All electrodeposited specimens were ultrasonically cleaned in double distilled water, rinsed in acetone and exposed to ambient atmosphere for at least 48 hours before potentiodynamic test. The potentiodynamic tests were performed by a μ Autolab/FRA2 potentiostat in aerated 3.5 wt.% NaCl solutions with pH of 10 and 3, which were adjusted by addition of NaOH and H₂SO₄. Potentiodynamic scans were conducted from -0.25 to 0.75 V vs. E_{corr} at room temperature and 0.166 mV/s scan rate. A saturated calomel electrode (SCE) and platinum were used as reference and counter electrodes, respectively. All samples were immersed in the test solution for 1 hour prior to potentiodynamic testing. The Tafel regions \pm 50 mV with respect to the tip of polarization curves were selected for the evaluation of E_{corr} and i_{corr} by Tafel extrapolation.

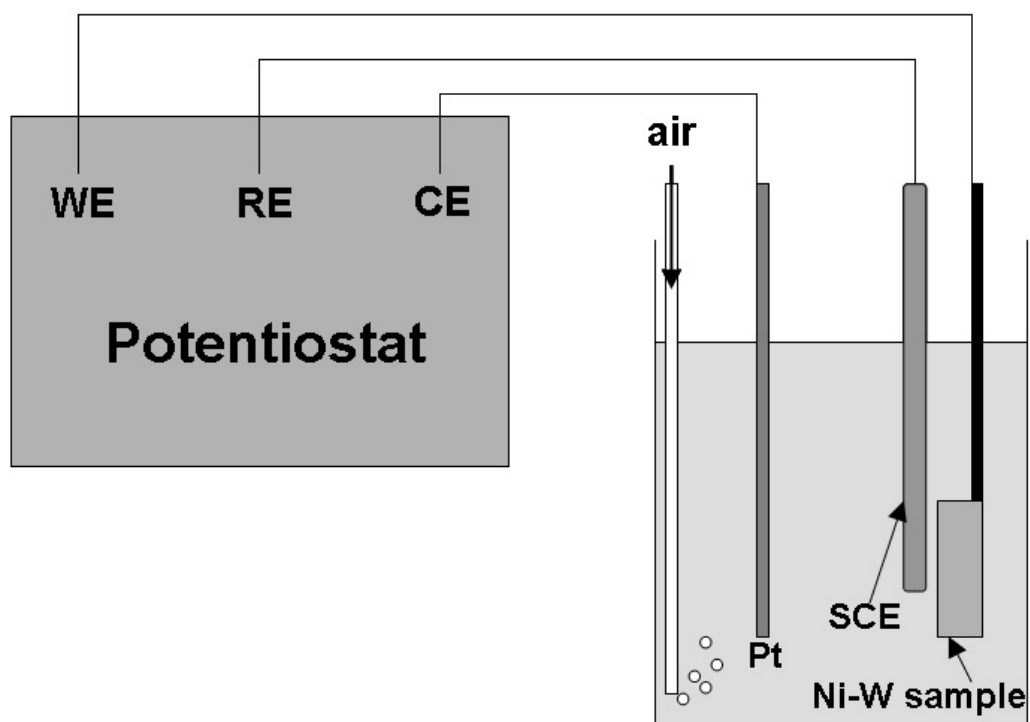


Fig. 3-4 Schematic diagram of the experimental setup used for potentiodynamic polarization and electrochemical impedance spectroscopy (EIS) tests of Ni-W samples. A platinum (Pt) rod was used as a counter electrode (CE). A saturated calomel electrode (SCE) was used as a reference electrode (RE). An as-deposited Ni-W sample was the working electrode.

Part II – Corrosion of Annealed Nanocrystalline Ni-W

With a view toward application, in this part, we investigate the corrosion properties of annealed nanocrystalline Ni-W alloys in 3.5 wt.% NaCl solutions with pH of 10 and 3, which are representative of corrosive environments of relevance to many engineering applications. Reverse pulse electrodeposition is employed as a technique to systematically fabricate nanocrystalline Ni-W alloys of two grain sizes and tungsten

content. Following electrodeposition, the Ni-W specimens were annealed to grain growth and grain boundary relaxation. The annealed Ni-W specimens were polished to remove any oxide layers formed during annealing before evaluation of electrochemical corrosion behavior by potentiodynamic polarization test. For comparison purposes, the corrosion behaviour of starting as-deposited Ni-W specimens with polished surface were also examined under the same conditions by potentiodynamic polarization technique.

1 Heat Treatment

In this part, as-deposited Ni-W specimens produced from reverse current density of 0.10 and 0.20 A/cm² were selected for grain growth and grain boundary relaxation thermal annealing. All as-deposited Ni-W specimens to be heat treated were prepared on Ni substrate by the same procedure as described in Part I.

1.1 Grain Boundary Relaxation

Grain boundary relaxation of nanocrystalline Ni-W alloys can be achieved through thermal annealing. To examine the effect of grain boundary relaxation on corrosion behavior, the appropriate annealing temperature must be selected such that grain boundary relaxation is achieved with negligible grain growth. It is evident that negligible grain growth in nanocrystalline Ni-W alloys is observed for heat treatment temperature up to ~300 °C (Fig. 3-5), while the grain boundary relaxation commences at ~120 °C (Fig. 3-6). Consequently, the temperature selected for grain boundary

relaxation is 200 °C, which lies within the range of 120-300 °C. To achieve grain boundary relaxation, as-deposited Ni-W specimens were isothermally annealed at 200 °C for 24 hours in 99.999% purity N₂ inert atmosphere with the N₂ gas flow rate of 2,000 cm³/min.

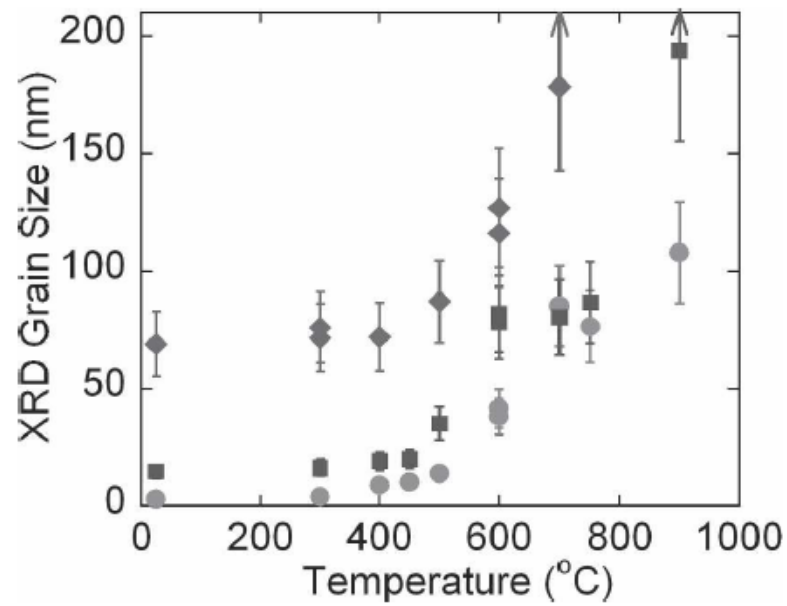


Fig. 3-5 The Ni-W grain size quantified by X-ray diffraction analysis for 24-hr heat treatments of three different starting grain sizes (plotted at 25 °C), showing negligible grain growth up to ~300 °C (Detor, and Schuh, 2007d: 3233).

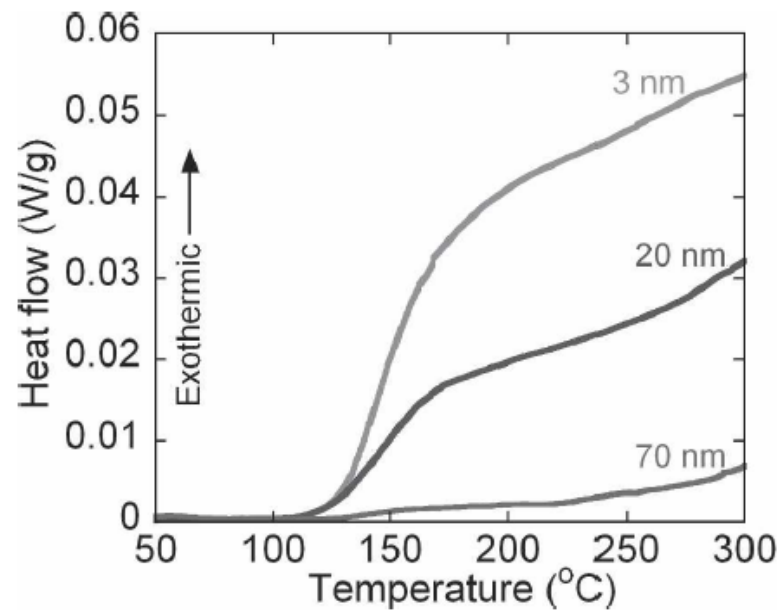


Fig. 3-6 Differential scanning calorimetry results showing the irreversible heat release in as-deposited 3, 20 and 70 nm grain size specimens. Exothermic signals, beginning at ~ 120 °C, are attributed to grain boundary relaxation of the as-deposited Ni-W specimens (Detor, and Schuh, 2007d: 3233).

1.2 Grain Growth

The samples with grain growth were obtained from annealing the samples with grain boundary relaxation at a suitable temperature. In order to examine the effect of grain growth on corrosion behavior, the temperature for grain growth must be selected such that no precipitation of second phase occurs. Nevertheless, nanocrystalline structure is a metastable state of solid. Thus the thermodynamic behavior of Ni-W alloys with nanocrystalline structure cannot be predicted by a Ni-W binary phase diagram (Fig.3-7) which is constructed for the equilibrium or the stable state of the alloy. For instance, the phase diagram (Fig. 3-7) predicts that at temperature below 100 °C we

cannot input tungsten content higher than ~12 at.% into the Ni matrix without precipitation of Ni_4W intermetallic phase. Nonetheless, the precipitate-free nanocrystalline Ni matrix containing as high as 21 at.% W has been successfully electrodeposited at 75 °C (Detor, and Schuh, 2007d: 3233). Consequently, instead of Ni-W binary phase diagram, the literature of thermal stability of nanocrystalline Ni-W alloys was consulted for the selection of suitable annealing temperature for grain growth (Detor, and Schuh, 2007d: 3233).

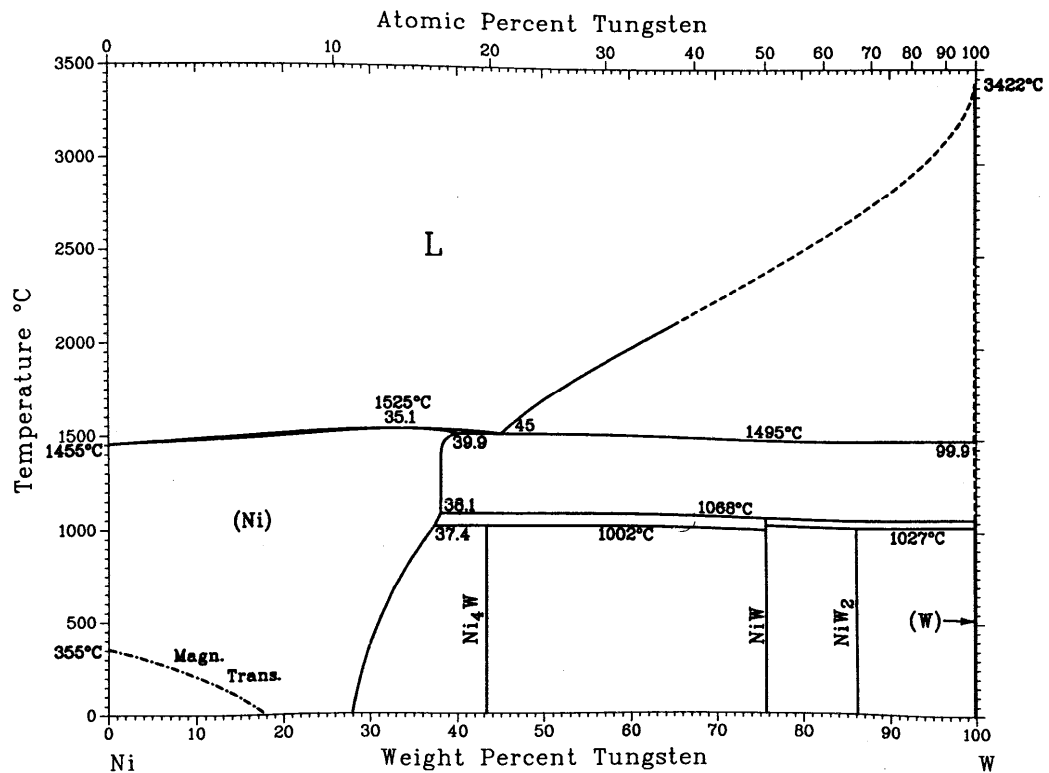


Fig. 3-7 Nickel-Tungsten binary phase diagram (ASM Handbook V. 3, 1992: 253).

Fig. 3-8 shows that annealing as-deposited nanocrystalline Ni-W alloys containing 21 at.%W at the temperature up to 600 °C prevents the precipitation of Ni_4W intermetallic phase. Based on this data from the literature, we devise the following

annealing scheme (Fig. 3-9) to achieve grain growth without precipitation of Ni_4W : first, ramping from 25 to 400 °C at the rate of 4.4 °C/min, second, after reaching 400 °C, immediately ramping from 400 to 600 °C at the rate of 8.8 °C/min, third, isothermal annealing at 600 °C for 3 hours, finally, cool down from 600 to 200 °C. The whole annealing procedure was carried out in 99.999% purity N_2 atmosphere with the N_2 gas flow rate of 2,000 cm^3/min .

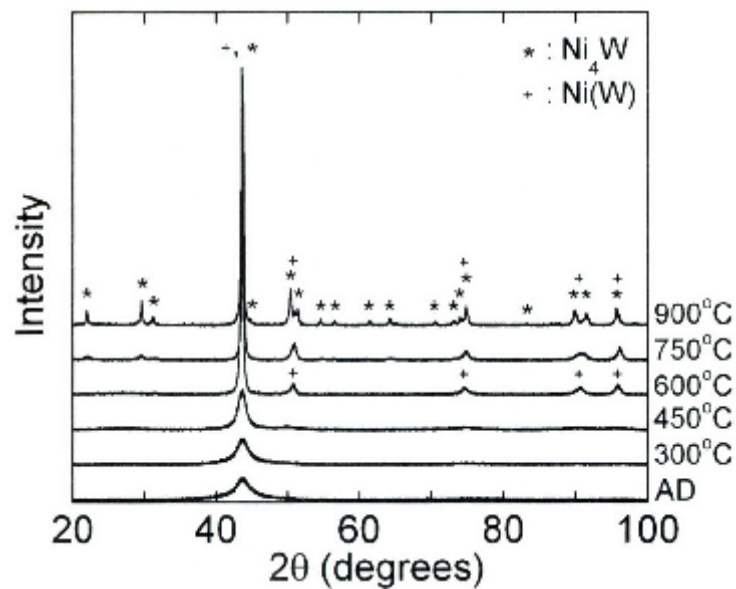


Fig. 3-8 X-ray diffraction patterns for 24-hr heat treatments of an as-deposited (AD) 3 nm grain size specimen containing 21 at.%W. The structure remains fairly stable up to 450 °C followed by grain coarsening at 600 °C and eventual precipitation of the equilibrium Ni_4W phase at higher temperatures (Detor, and Schuh, 2007d: 3233).

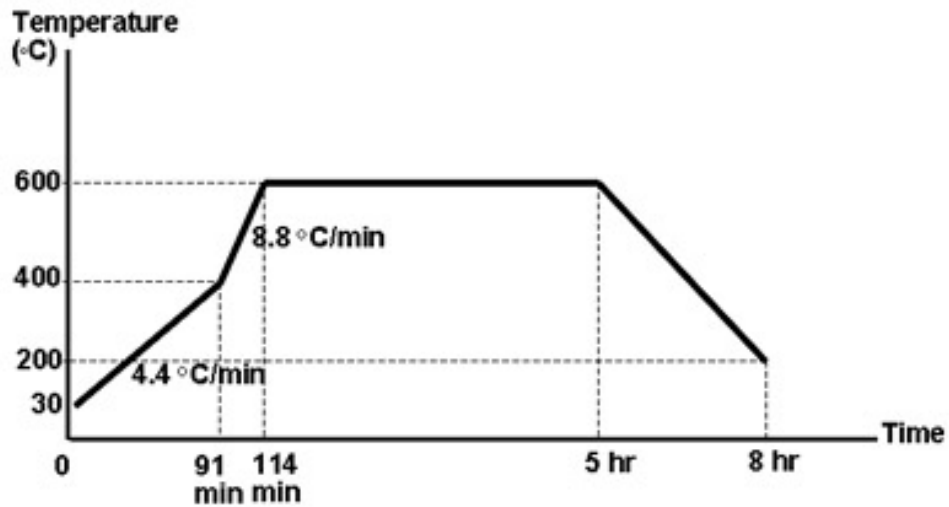


Fig. 3-9 The annealing scheme for grain growth.

2 Characterization

In Part II, the major goal is to investigate the impact of grain boundary relaxation and grain growth on corrosion properties of nanocrystalline Ni-W alloys. However, aside from grain boundary relaxation and grain growth, the same factors as in Part I, namely, tungsten content, grain size, crystallographic texture and surface composition should still play a role on the corrosion properties of annealed Ni-W. Thus, the same characterization techniques employed in Part I were also used here in Part II. All characterization procedures were performed on selected specimens prior to corrosion test.

2.1 Tungsten Content

Tungsten contents of representative specimens were measured by EDS technique using the same procedure and parameters described in Part I.

2.2 Grain Size

2.2.1 Measurement of Nanocrystalline Grain Size

The measurement of nanocrystalline grain size follows the same procedure and parameters as described in Part I.

2.2.2 Measurement of Microcrystalline Grain Size

None. Experiments in Part II do not involve any samples with microcrystalline grain size.

2.3 Hardness

To assess grain boundary relaxation, the hardness values of as-deposited and grain boundary relaxed specimens were measured by Mitutoyo micro Vickers hardness tester using 100 g load. The hardness value is computed from the average of nine measurements taken at nine positions on each sample as shown in Fig. 3-3.

2.4 Crystallographic Texture

The characterization of crystallographic texture by x-ray diffraction pole figures follows the same parameters as described in Part I.

2.5 Surface Composition

Since the surface oxide layer formed during annealing was removed from annealed Ni-W specimens by mechanical polishing, the surface morphology was also removed in the process. Consequently, no surface morphology characterization was performed in Part II.

For characterization of surface film composition, the annealed and selected as-deposited Ni-W specimens were first cut into tiny coupons ($0.5 \times 0.5 \text{ cm}^2$), mechanically polished to $6 \mu\text{m}$, ultrasonically cleaned in soap solution, ultrasonically cleaned in doubly distilled water, ultrasonically cleaned in acetone and exposed to ambient atmosphere for at least 48 hours to allow new surface film to form. After that, prior to any electrochemical test, an Axis Ultra x-ray photoelectron spectroscopy (XPS) system (Kratos Analytical of Manchester, England) using monochromatic Al K_{α} radiation was used to characterise the surface film on annealed Ni-W specimens.

3 Potentiodynamic Polarization

Electrochemical corrosion behaviours of selected as-deposited and annealed nanocrystalline Ni-W alloys were examined by means of potentiodynamic polarization technique. The schematic diagram for the experimental setup is illustrated in Fig. 3-4. All as-deposited and annealed specimens were ultrasonically cleaned in soap solution and doubly distilled water, rinsed in acetone and exposed to ambient atmosphere for at least 48 hours before potentiodynamic test. The potentiodynamic tests followed the experimental procedure and parameters as described in Part I.

Part III – Interfacial Corrosion Phenomena of As-Deposited and Annealed Nanocrystalline Ni-W

In this part, we aim to elucidate the interfacial phenomena occurring during corrosion of as-deposited and annealed nanocrystalline Ni-W alloys by means of electrochemical impedance spectroscopy. The insight gained from this section in combination with that from the previous two parts will cast mechanistic light into corrosion behavior of as-deposited and annealed nanocrystalline Ni-W alloys. The same sets of specimens in Part II were investigated in Part III.

1 Electrochemical Impedance Spectroscopy (EIS)

Electrochemical impedance spectroscopy (EIS) is the technique used to probe the electrochemical phenomena at the solid / electrolyte interface. During EIS measurement, very small amplitude of sinusoidal electrical signal (normally 1 – 10 mV) spanning a range of frequency is applied to an electrochemical system of interest (Barsoukov, and Macdonald, 2005: 192; Orazem, and Tribollet, 2008: 133). At different frequencies of applied signal, the electrochemical phenomena at metal / electrolyte interface will generate different sinusoidal impedance responses. Each impedance response can be expressed in term of a complex number which can be plotted in a real and imaginary impedance plane (Nyquist plot) as shown in Fig. 3-10.

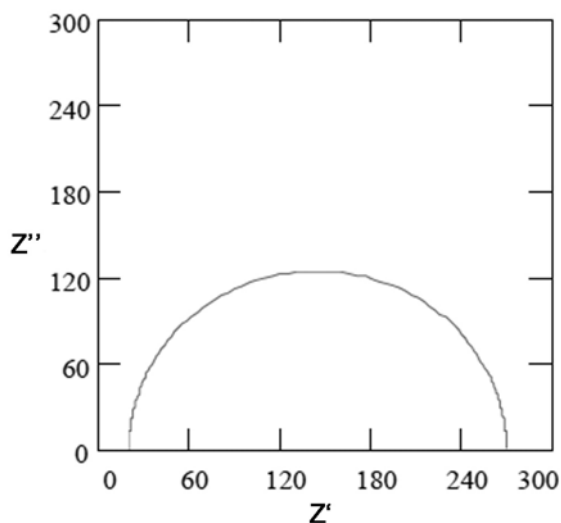


Fig. 3-10 A typical Nyquist plot of impedance spectra of an electrochemical system. The horizontal axis of the plot is the real part of impedance and the vertical axis is the imaginary part of impedance (Orazem, and Tribollet, 2008: 155).

However, not only electrochemical systems generate impedance responses from sinusoidal voltage perturbation, but so do electrical circuits. Consequently, it is possible to find an electrical circuit analog that mimics the electrochemical phenomena at metal / electrolyte interface by identifying the electrical circuit that generates similar impedance response to that of the electrochemical system of interest (Mansfeld, 1990: 1533; Macdonald, 2006: 1376). Generally, the identification a proper circuit analog involves the method of trial and error and the consultation of previous work reported in the literature. Simulation of impedance response of a circuit analog can be achieved through several software programs available in the market. In this thesis, the simulation of the circuit analog is achieved through the application of Autolab FRA software. Each circuit element in the circuit analog corresponds to each electrochemical parameter

governing the electrochemical phenomena at the metal / electrolyte interface. However, EIS technique also has its limitation. Since EIS mainly involves pattern recognition of the impedance responses of the circuit analog and the electrochemical system, it is not a standalone technique (Macdonald, 2006: 1376; Orazem, and Tribollet, 2008: 357). Other observations are required to validate a given interpretation of the impedance spectra. Consequently, the EIS results presented in Part III are validated through the agreement with corresponding potentiodynamic results in Parts I and II.

In this thesis, interfacial corrosion phenomena of as-deposited and annealed nanocrystalline Ni-W alloys were examined by means of electrochemical impedance spectroscopy. All as-deposited and annealed specimens were ultrasonically cleaned in soap solution and doubly distilled water, rinsed in acetone and exposed to ambient atmosphere for at least 48 hours before EIS test. The schematic diagram for the experimental setup is illustrated in Fig. 3-4. EIS scan was performed at 10 mV amplitude and $3 \times 10^{-2} - 3 \times 10^4$ Hz frequency range in aerated 3.5 wt.% NaCl solutions with pH of 10 and 3, which were adjusted by addition of NaOH and H₂SO₄ at room temperature. A saturated calomel electrode (SCE) and platinum were used as reference and counter electrodes, respectively. Prior to EIS tests, samples were immersed in aerated test solution for 1 hour. The impedance spectra from EIS investigation will be reported in Part III of Chapter 4, while the interpretation of the impedance spectra and the circuit analog from the investigation of Ni-W alloys will be presented in Part III of Chapter 5.

CHAPTER IV

EXPERIMENTAL RESULTS

This section is divided into three parts including Part I – Corrosion of As-Deposited Nanocrystalline Ni-W, Part II – Corrosion of Annealed Nanocrystalline Ni-W and Part III – Interfacial Corrosion Phenomena of As-Deposited and Annealed Nanocrystalline Ni-W.

Part I – Corrosion of As-Deposited Nanocrystalline Ni-W

1 Electrodeposited Microcrystalline Ni and Nanocrystalline Ni-W alloys

In Part I, we investigated the electrodeposited Ni and five sets of Ni-W alloy specimens which were fabricated with a uniform and crack-free morphology. Their processing parameters and the corresponding characteristics are tabulated in Table 4-1. The average grain size of the Ni deposit was determined to be 7 μm by SEM and line intercept method. In line with prior literature for Ni-W plating (Detor, and Schuh, 2007a: 371], the increase of reverse current density upon deposition from 0 to 0.30 A/cm^2 leads to a reduction in the W content in Ni-W deposits from 21.8 to 4.9 at.% as illustrated in Fig. 4-1. Since in this system W content controls grain size (via a slight tendency for W to segregate to grain boundaries), the change in applied current waveform results in a change in grain size as suggested by XRD peak broadening, as shown in Fig. 4-2. Particularly, the average grain size of the alloys ranges from about 63 to 5 nm (Fig. 4-1).

Table 4-1 Physical characteristics of, and associated pulse plating parameters used to prepare, the microcrystalline Ni and nanocrystalline Ni-W deposits.

Sample	Reverse pulse current (A/cm^2)	Tungsten content (at.%)	XRD grain size (nm)
mc Ni	0	0	7 μm
Ni-5W	0.30	4.9	63
Ni-6W	0.20	6.0	39
Ni-11W	0.15	10.7	10
Ni-18W	0.10	17.8	6
Ni-22W	0	21.8	5

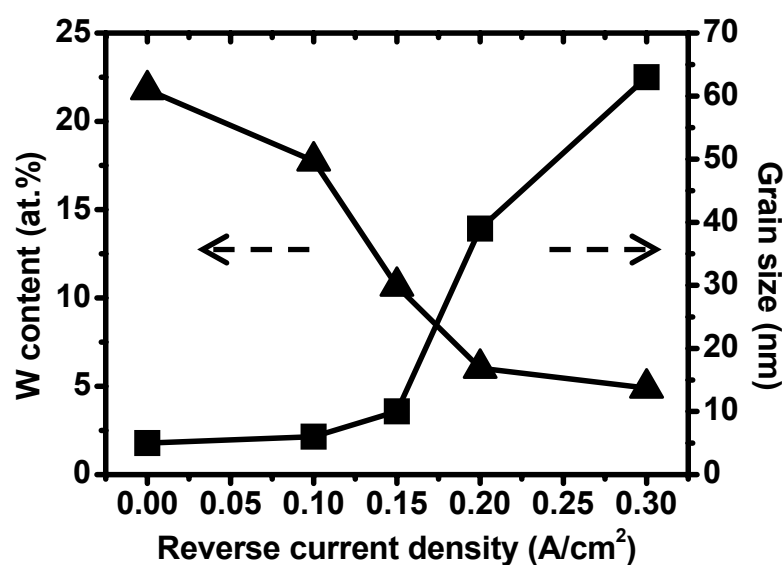


Fig. 4-1 The interrelationship between reverse current density, tungsten content (solid triangle) and grain size (solid square) of Ni-W alloys. The decrease in reverse current density causes tungsten content in the alloys to increase, promoting the formation of smaller-sized grains through grain boundary segregation of tungsten atoms in Ni matrix.

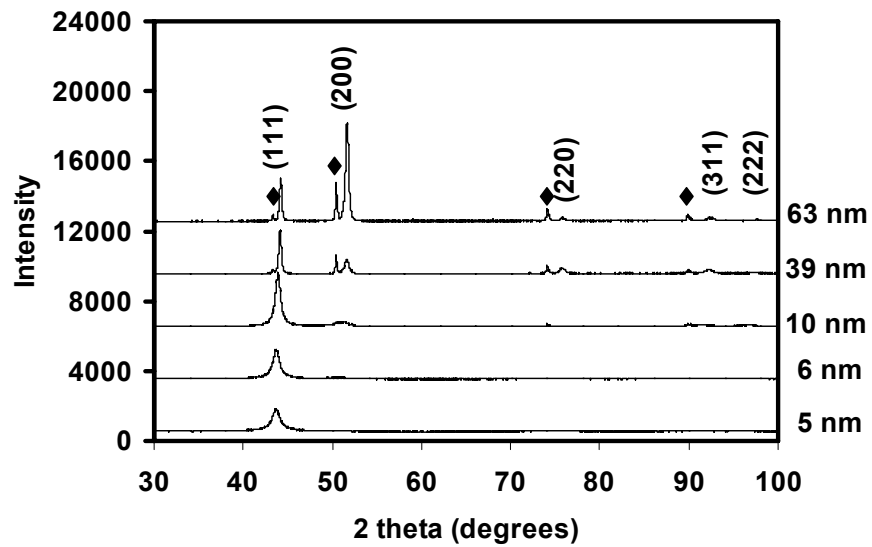


Fig. 4-2 X-ray diffraction spectra of nc Ni-W alloys with average grain size ranging from 5 to 63 nm. The expected reflections for nickel are shown in the plot, and the solid diamonds indicate the peaks from the copper substrate.

The XRD profiles in Fig. 4-2 also seem to suggest that the nc Ni-W specimens with relatively large grain size may exhibit texture with preferred orientation in the direction of $\{200\}$ planes. This speculation is clarified by the XRD pole figures, shown in Fig. 4-3, which illustrate that, in Ni-5W (63 nm), $\{200\}$ planes are preferentially oriented perpendicular to the surface normal direction, whereas $\{111\}$ planes are preferentially oriented at about 50° from the surface normal direction. Interestingly, this sample does not exhibit a simple fiber texture, but has a tendency for in-plane alignment of grains as indicated by the discontinuous ring of preferred $\{111\}$ positions in Fig. 4-3a. On the other hand, both Ni-6W and Ni-18W exhibit $\{111\}$ dominant crystallographic texture. In Ni-6W which exhibits smaller grain size (39 nm), the $\{111\}$ and $\{200\}$ crystallographic planes

become more randomly distributed (although with a slight suggestion of a weak {200} fiber). In Ni-18W of which grain size is extremely fine (6 nm), the texture is predominantly {111} fiber with {200} crystallographic planes preferentially oriented at 45° with respect to the surface normal.

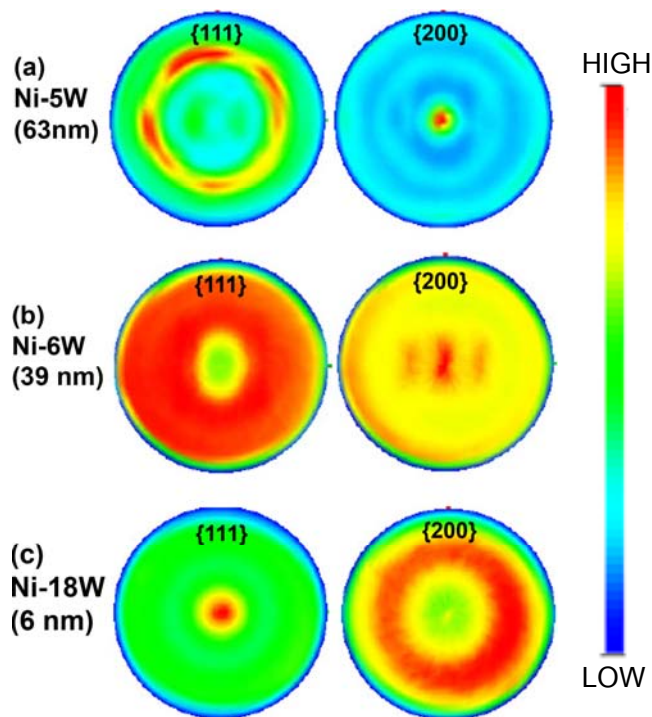


Fig. 4-3 The representative {111} and {200} pole figures of electrodeposited (a) Ni-5W (grain size = 63 nm), (b) Ni-6W (grain size = 39 nm) and (c) Ni-18W (grain size = 6 nm) samples, with the surface normal vector coming out of the page. The pole figures of Ni-5W demonstrate preferential orientation of {111} planes at about 50° from the surface normal direction and that of {200} planes in the surface normal direction. However, the pole figures of Ni-6W show relatively uniform orientation of {111} and {200} crystallographic planes, while Ni-18W exhibits strong {111}-fiber texture with {200} crystallographic planes preferentially oriented at about 45° from the surface normal.

In addition to the transition in texture, Fig. 4-4 presents the transition in surface morphology of some prepared deposits, including Ni, Ni-6W (39 nm), and Ni-18W (6 nm). As shown, when the W content is increased and grain size is reduced below ~ 10 nm, the surface morphology of nanocrystalline Ni-W transforms from angular to nodular morphology; this is in line with prior discussion on the effects of grain size on the surface structure of such deposits (Ruan, and Schuh, 2008: 1218).

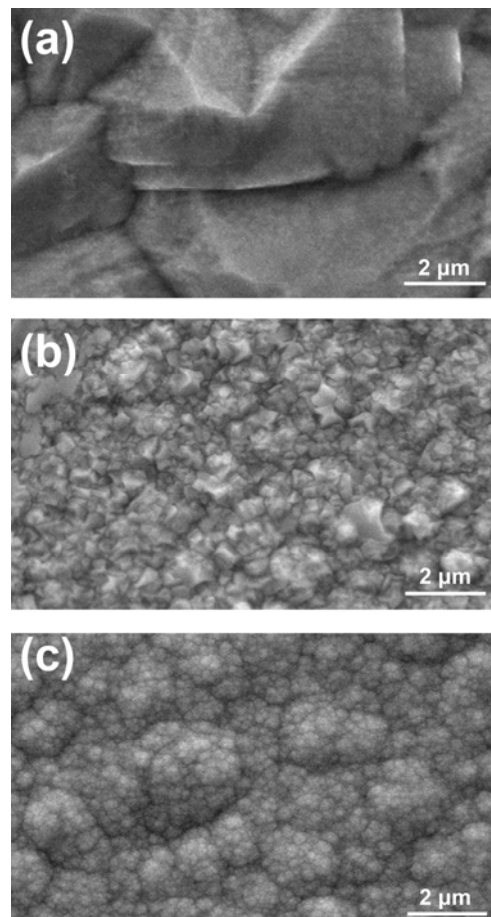


Fig. 4-4 Scanning electron micrographs revealing the surface morphology of (a) mc Ni, (b) Ni-6W and (c) Ni-18W. Relatively large grain structure is observed in mc Ni, whereas fine mesoscale structure, which is the characteristic of nanocrystalline materials, exists in both Ni-6W and Ni-18W.

Figure 4-5 (a-b) shows the XPS profiles of as-deposited Ni-6W and Ni-18W. The XPS analysis suggests that the surface of Ni-6W (Fig. 5a) contains mostly Ni (852.1 eV) (Furstenau et al., 1985: 55) and W (31.0 and 33.1 eV) (Takano et al., 1989: 25) metals with tungsten oxide as secondary component, having the oxidation state of tungsten (35.0 eV) between that of $W_{18}O_{49}$ (34.3 eV) and WO_3 (35.8 eV) (Zhang, and Macdonald, 1998: 2661). On the other hand, the surface film of Ni-18W (Fig. 5b) is comprised primarily of $NiWO_4$, as indicated by Ni 2p peak at 855.7 eV and W 4f peaks at 35.4 and 37.5 eV (Ng, and Hercules, 1976: 2094), with W as a minor component.

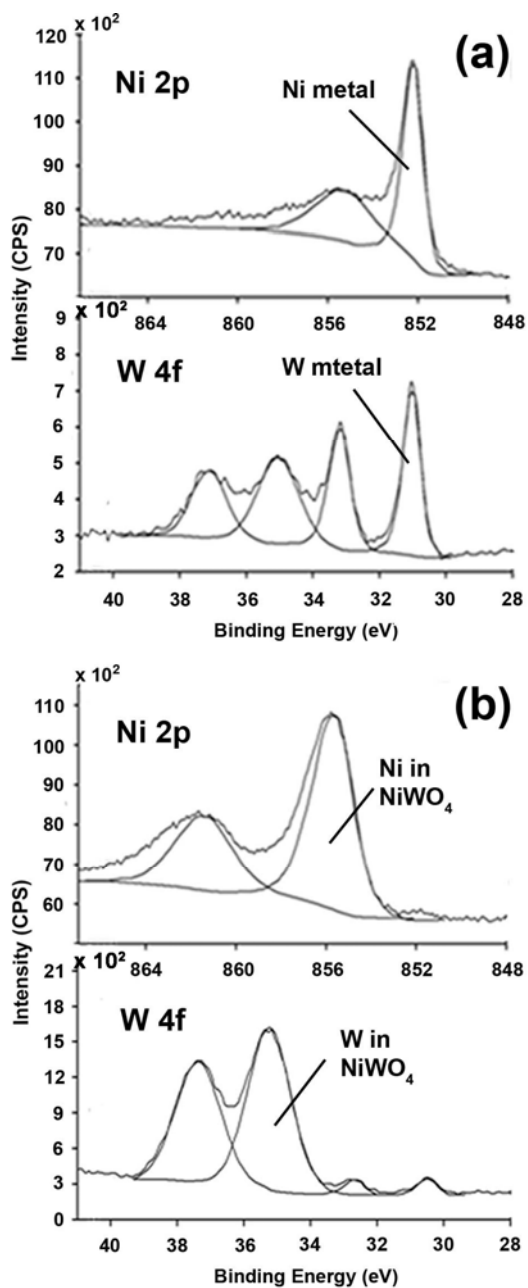


Fig. 4-5 Ni 2p and W 4f XPS spectral lines of (a) Surface of as-deposited Ni-6W which contains mostly Ni (as indicated by Ni 2p peak at 852.1 eV) and W (as indicated by W 4f peaks at 31.0 and 33.1 eV) metals and (b) Surface of as-deposited Ni-18W which contains mostly NiWO₄ (as indicated by the combination of Ni 2p peak at 855.7 eV and W 4f peaks at 35.4 and 37.5 eV).

2 Corrosion Behavior

Polarization curves of the specimens tested in 3.5 wt.% NaCl electrolyte with pH = 10 and pH = 3 are shown in Fig. 4-6 and 4-7, respectively. The polarization curves can be summarized in terms of E_{corr} and i_{corr} , examined with respect to the grain size as shown in Fig. 4-8 and Table 4-2. The plot of i_{corr} vs. grain size (Fig. 4-8) has demonstrated that nc Ni-W alloys with an average grain size between 5 and 63 nm generally exhibited higher corrosion rates in acidic pH = 3 than in alkaline pH = 10 3.5wt.% NaCl environments.

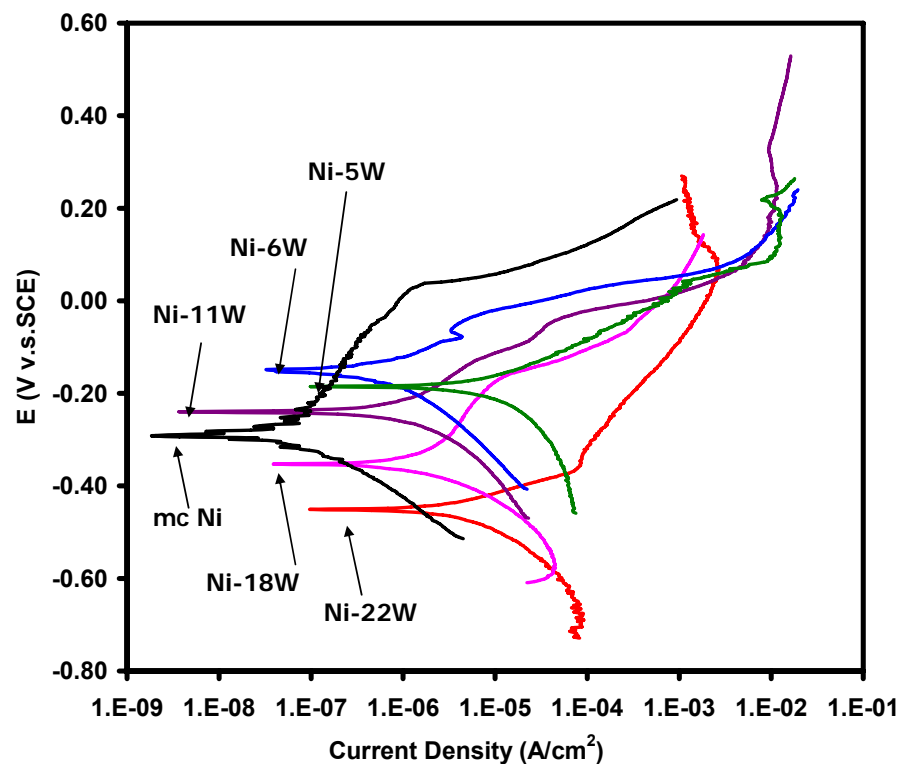


Fig. 4-6 Potentiodynamic curves of mc Ni and various nc Ni-W alloys in 3.5 wt.% NaCl solution at pH = 10.

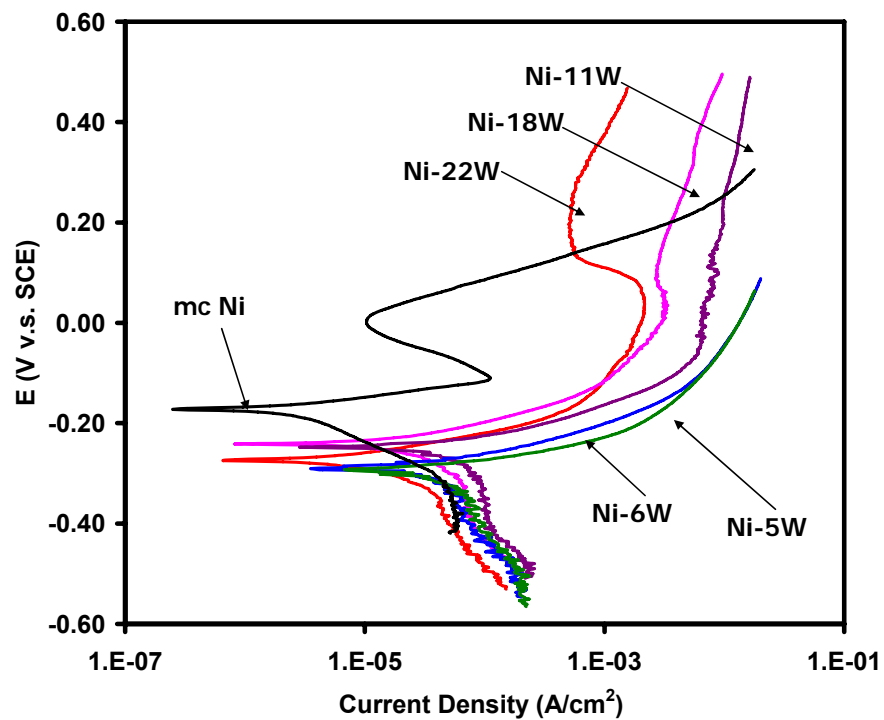


Fig. 4-7 Potentiodynamic curves of mc Ni and various nc Ni-W alloys in 3.5 wt.% NaCl solution at pH = 3.

2.1 3.5 wt.% NaCl at pH = 10

For the pH = 10 condition, as grain size decreases from 63 to 39 nm (Fig. 4-8), E_{corr} noticeably increases from -0.186 to -0.137 V vs. SCE and i_{corr} noticeably decreases from 3.10 to 0.143 $\mu\text{A}/\text{cm}^2$ (Table 4-2), but these trends then reverse as grain size further decreases to 5 nm ($i_{\text{corr}} = 4.67 \mu\text{A}/\text{cm}^2$). No sign of pitting was detected in any of the nanocrystalline specimens. The mc Ni exhibits the lowest corrosion rate ($i_{\text{corr}} = 0.067 \mu\text{A}/\text{cm}^2$), however it was susceptible to pitting corrosion, as shown in Fig. 4-9 (a-b).

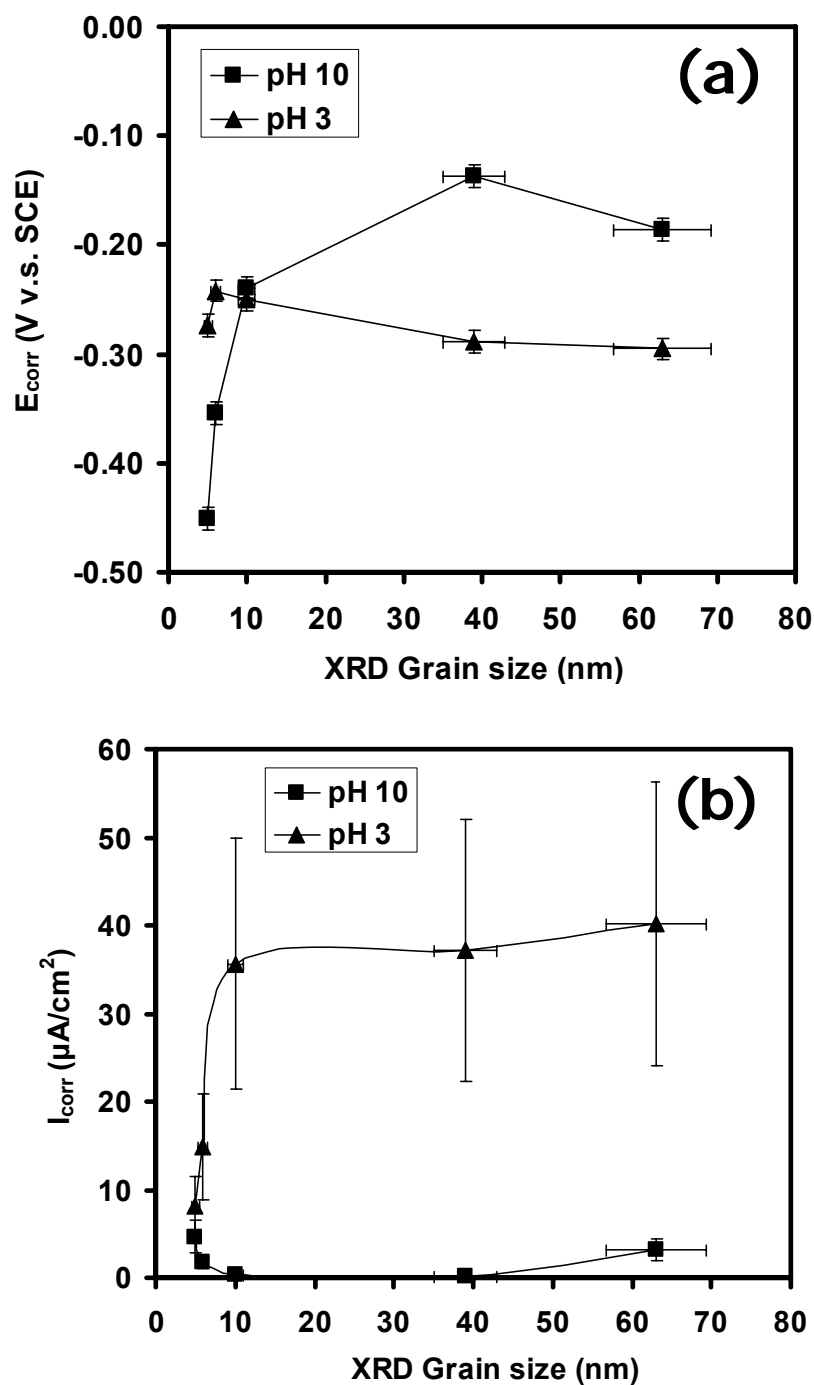


Fig. 4-8 The corrosion potential (E_{corr}) (a) and corrosion current density (i_{corr}) (b) of the deposits of various grain sizes. The triangle and square signs represent the data of the deposits tested in 3.5 wt.% NaCl at pH = 3 and at pH = 10, respectively.

Table 4-2 i_{corr} and E_{corr} of as-deposited Ni and Ni-W specimens in pH=10 and 3 3.5 wt.% NaCl solutions

Sample	Grain size (nm)	pH = 10		pH = 3	
		i_{corr} ($\mu\text{A}/\text{cm}^2$)	E_{corr} (V vs. SCE)	i_{corr} ($\mu\text{A}/\text{cm}^2$)	E_{corr} (V vs. SCE)
mc Ni	7 μm	0.0671	-0.294	3.35	-0.172
Ni-5W	63	3.10	--0.186	40.2	-0.295
Ni-6W	39	0.143	-0.137	37.2	-0.289
Ni-11W	10	0.324	-0.239	35.6	-0.250
Ni-18W	6	1.70	-0.354	14.9	-0.242
Ni-22W	5	4.67	-0.451	8.20	-0.274

Figure 4-6 provides some hints as to the film formation characteristics of nc Ni-W. While there is no apparent process of passivation in Ni-5W (grain size of 63 nm), the degree of film formation is observed to be more noticeable with the reduction of grain size (and the concurrent increase in W content). For the Ni-18W deposit (grain size of 6 nm), the film formation tendency is the strongest among Ni-W samples, with i_{pass} of $\sim 4 \times 10^{-6} \text{ A/cm}^2$ and pitting potential (E_{pit}) of -0.162 V vs. SCE. The film formation tendency, however, completely disappears as the grain size decreases further to 5 nm (Ni-22W). Relative to all of the nc Ni-W samples, mc Ni exhibited apparent passivation with i_{pass} of $\sim 3 \times 10^{-7} \text{ A/cm}^2$ and E_{pit} of 0.038 V vs. SCE.

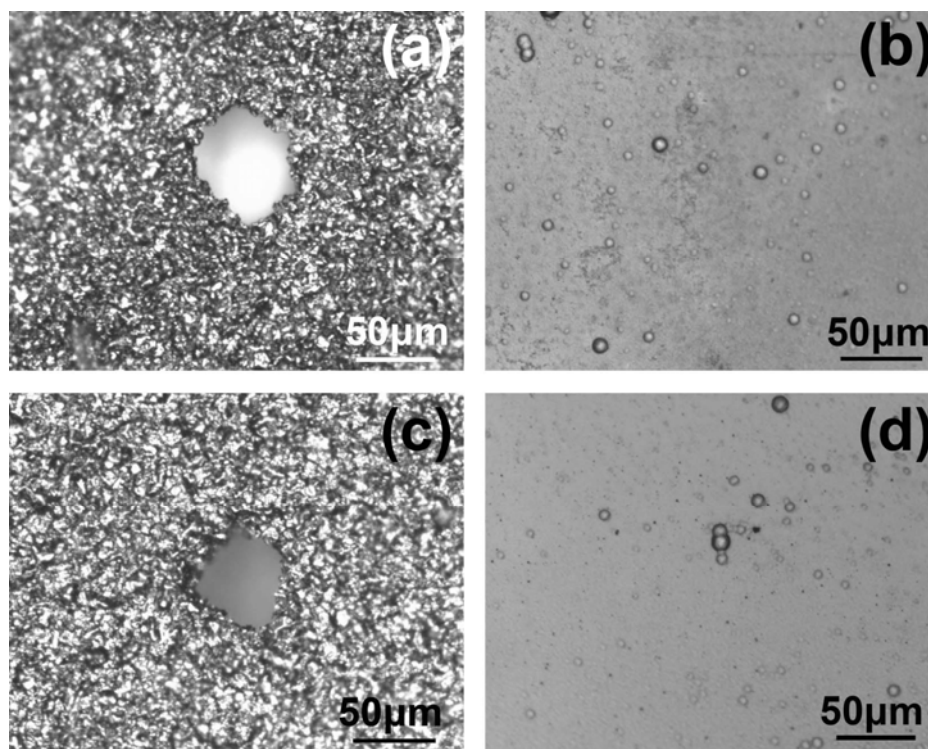


Fig. 4-9 Morphology of specimens after potentiodynamic tests in 3.5 wt.% NaCl solution: (a) mc Ni and (b) Ni-18W tested in pH = 10 solution; and (c) mc Ni and (d) Ni-18W tested in pH = 3 solution. The large pits in mc Ni (a,c) are signatures of localised corrosion. No such pits are found in nc Ni-W; the small circles in (b,d) are surface nodules in the plated structure, and not corrosion sites.

2.2 3.5 wt.% NaCl at pH = 3

Figure 4-7 shows the polarization curves of the specimens tested in 3.5 wt.% NaCl with pH = 3, and Fig. 4-8 summarizes the corresponding E_{corr} and i_{corr} results. The various nc Ni-W specimens exhibit similar E_{corr} , and exhibit no passivation (Fig. 4-7). The mc Ni specimen, on the other hand, exhibits fairly low i_{corr} ($3.35 \mu\text{A}/\text{cm}^2$) and high E_{corr} (0.172 V vs. SCE) in relation to the nc Ni-W specimens ($8.20 - 40.2 \mu\text{A}/\text{cm}^2$). This

agrees well with the observed passivation of mc Ni with i_{pass} of $\sim 1 \times 10^{-5} \text{ A/cm}^2$. It should be noted that the i_{corr} values of all nc Ni-W alloys in pH = 10 NaCl are lower than those in pH = 3 NaCl, implying higher uniform corrosion resistance of nc Ni-W in the alkaline condition. Fig. 4-9 (c-d) shows that, in the acidic saline environment, mc Ni experienced pitting corrosion, while the corrosion of nc Ni-W is uniform.

Part II – Corrosion of Annealed Nanocrystalline Ni-W

1 Annealed Ni-W Specimens

In Part II, we investigated the two sets of as-deposited Ni-W and four sets of annealed Ni-W alloy specimens. The annealing conditions and the corresponding tungsten content and grain size are tabulated in Table 4-3. The nomenclature of the specimens includes Ni-6W-AD standing for as-deposited Ni-6W, Ni-6W-R standing for annealed Ni-6W with grain boundary (GB) relaxation, and Ni-6W-GG standing for annealed Ni-6W with grain growth. The nomenclature of Ni-18W specimen series follows the same system as that of Ni-6W specimen series.

Table 4-3 The annealing conditions, tungsten content and grain size of the test specimens investigated in Part II.

Sample	Annealing condition	Tungsten content (at.%)	XRD grain size (nm)
Ni-6W-AD	None	5.5	52
Ni-6W-R	GB relaxation	5.5	54
Ni-6W-GG	Grain growth	5.5	110
Ni-18W-AD	None	17.6	7
Ni-18W-R	GB relaxation	17.6	8
Ni-18W-GG	Grain growth	17.6	62

In line with previous work (Detor, and Schuh, 2007d: 3233), nanocrystalline Ni-W alloys with distinct grain size exhibit different increment in hardness upon grain boundary relaxation and grain growth due to their significant difference in intercrystalline volume fraction (Table 4-4). In analogy, Ni-W alloys with different starting grain sizes may demonstrate different corrosion behaviors upon grain boundary relaxation and grain growth. Consequently, Ni-6W-AD (52 nm) and Ni-18W-AD (7 nm) were selected as the starting materials for the production of two specimen series with distinct grain sizes for the investigation of corrosion behaviour. Furthermore, in order to aid the visualization of the change in grain size upon grain boundary relaxation and grain growth (Table 4-3), the relationship between grain size vs. annealing temperature was presented in Fig. 4-10.

Table 4-4 Comparison of the hardness of as-deposited and grain-boundary-relaxed specimens.

Sample	Grain boundary relaxation	Hardness (GPa)
Ni-6W-AD	No	4.2
Ni-6W-R	Yes	4.7
Ni-18W-AD	No	6.9
Ni-18W-R	Yes	8.7

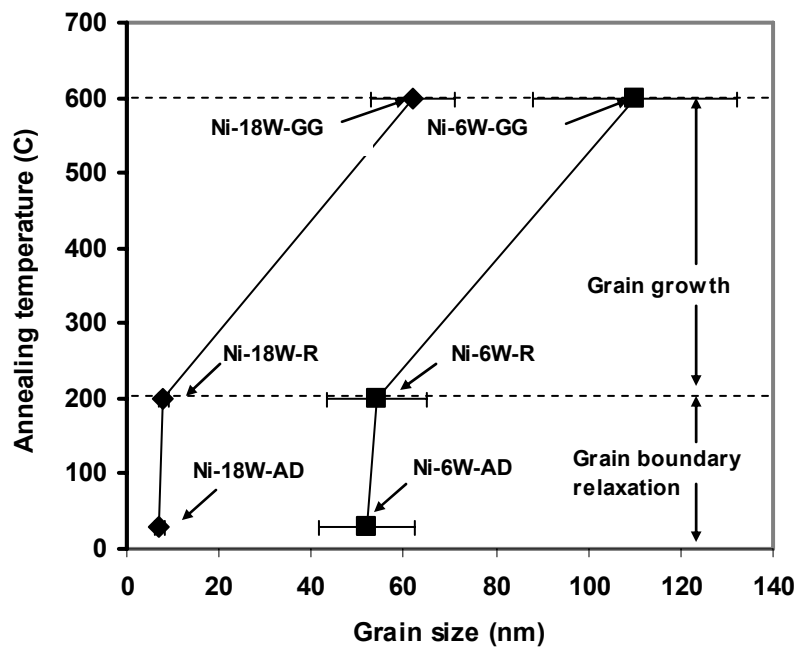


Fig. 4-10 The diagram showing the change of grain size upon annealing temperature of Ni-6W and Ni-18W specimen series.

According to Table 4-3 and Fig. 4-10, the average grain size of the Ni-6W-AD was determined to be 52 nm by X-ray integral breadth method. However, the data in Part I (Table 4-1) show that average grain size of as-deposited Ni-6W determined by the

same method is 39 nm. For Ni-W alloys containing relatively low tungsten content, a minor variation in tungsten content may cause a noticeable change in grain size. Thus, the larger grain size of Ni-6W-AD (52 nm, 5.5 at.%W) in Part II relative to as-deposited Ni-6W specimen (39 nm, 6.0 at.%W) in Part I must be attributed the slight variation in tungsten content.

Upon annealing Ni-6W-AD (52 nm) at 200 °C for 24 hours to produce Ni-6W-R (54 nm), the change in grain size is minimal. However, the increase in hardness (Table 4-4), indicative of grain boundary relaxation, occurs at this annealing condition. During thermal annealing at 200 °C for 24 hours, annihilation of excess grain boundary dislocations decreases the number of nucleation sources for intragranular partial and/or unit dislocations, leading to the increasing critical shear stress required to initiate slip (Trelewicz, 2008: 91). This phenomenon is termed “grain boundary relaxation,” (Jang, and Atzmon, 2006: 083504) which accounts for the observed strengthening upon annealing. Thus, for Ni-6W-R specimens, grain boundary relaxation is achieved with negligible grain growth.

In contrast, upon annealing Ni-6W-AD (52 nm) at maximum 600 °C, according to the heat treatment procedure described in Part II of Chapter 3, to produce Ni-6W-GG (110 nm), the grain size of the annealed specimen increases over 100%. In addition to grain growth, heat treatment of nanocrystalline Ni-W alloys at 600 °C also leads to grain boundary relaxation (Detor, 2007c: 81). Thus, Ni-6W-GG specimens must undergo both significant grain growth and grain boundary relaxation. Along the same line of argument, upon annealing Ni-18W-AD (7 nm), Ni-18W-R (8 nm) also experienced grain boundary

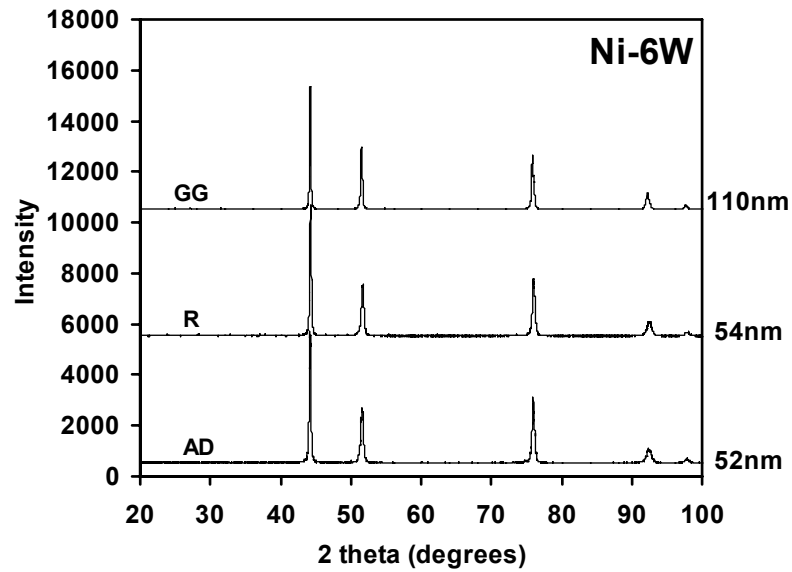


Fig. 4-11 X-ray diffraction spectra of Ni-6W specimen series including Ni-6W-AD (52 nm), Ni-6W-R (54 nm) and Ni-6W-GG (110 nm). AD denotes as-deposited. R denotes grain boundary relaxation. GG denotes grain growth.

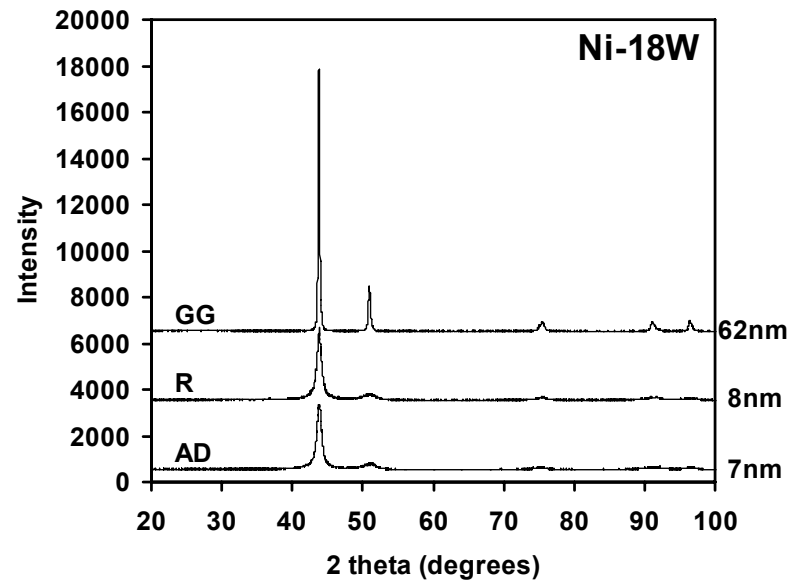


Fig. 4-12 X-ray diffraction spectra of Ni-18W sample series including Ni-18W-AD (7 nm), Ni-18W-R (8 nm) and Ni-18W-GG (62 nm). AD denotes as-deposited. R denotes grain boundary relaxation. GG denotes grain growth.

relaxation with negligible grain growth, while Ni-18W-GG (62 nm) underwent both grain growth and grain boundary relaxation.

X-ray diffraction spectra in Fig. 4-11 and 4-12 correspond to Ni-6W and Ni-18W specimen series, respectively. These X-ray spectra were used to determine grain size of the specimens by X-ray integral breadth method which is capable of determining nanometer grain size up to ~100 nm. Fig. 4-11 shows that although XRD peak broadenings of Ni-6W-AD, Ni-6W-R and Ni-6W-GG are actually different, with Ni-6W-AD being the largest and Ni-6W-GG being the smallest, they look indistinguishable to bare eyes. On the contrary, XRD peak broadenings of Ni-18W specimen series are apparently visible, with Ni-18W-AD being the largest and Ni-18W-GG being the smallest, conforming to the grain size determined by X-ray integral breadth method. In general, it may thus be concluded that the XRD peak broadening effect of nanometer grain size is not clearly distinguishable to naked eyes for grain size larger than ~50 nm. Most importantly, the XRD spectra shown in Fig. 4-11 and 4-12 show no precipitation of second phase.

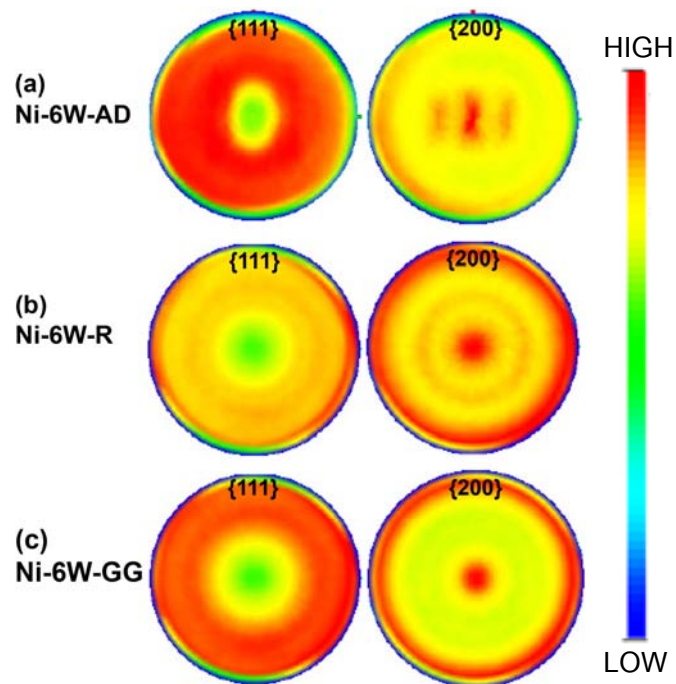


Fig. 4-13 The representative $\{111\}$ and $\{200\}$ X-ray diffraction pole figures of Ni-6W sample series (a) Ni-6W-AD (grain size = 52 nm), (b) Ni-6W-R (grain size = 54 nm) and (c) Ni-6W-GG (grain size = 110 nm) samples, with the surface normal vector coming out of the page. The pole figure of Ni-6W-AD specimen shows relatively uniform orientation of $\{111\}$ and $\{200\}$ crystallographic planes with slight $\{200\}$ -fiber texture. There seems to be noticeable change in texture upon grain boundary relaxation. The texture, however, seems to shift back to the original state (Ni-6W-AD) upon grain growth.

As shown in Fig. 4-13, the Ni-6W-AD specimen shows relatively uniform orientation of $\{111\}$ and $\{200\}$ crystallographic planes with relatively weak $\{200\}$ fiber texture. After thermal annealing, as compared to electrodeposited Ni-6W-AD, Ni-6W-R exhibit a shift in crystallographic texture for both $\{111\}$ and $\{200\}$ poles. However, upon grain growth the crystallographic texture of Ni-6W-GG seems to shift to resemble that of

Ni-6W-AD.

The pole figures of Ni-18W specimen series as illustrated in Figure 4-14 also show different trend of observation. The pole figure of the Ni-18W-AD specimen exhibits strong {111}-fiber texture with {200} crystallographic planes preferentially oriented at about 45° from the surface normal vector. Upon grain boundary relaxation, {111} pole remains the same, but the noticeable textural shift is observed for {200} pole. Upon grain growth, the crystallographic texture exhibits further diversion from the original texture of Ni-18-AD.

As discussed thus far, both XRD spectra (Fig. 4-11 and 4-12) show that none of the samples contains precipitated second phase. Furthermore, Fig. 4-13 and 4-14 demonstrate that the whole set of Ni-W specimens investigated in Part II exhibits noticeable shift in crystallographic texture upon grain boundary relaxation and grain growth.

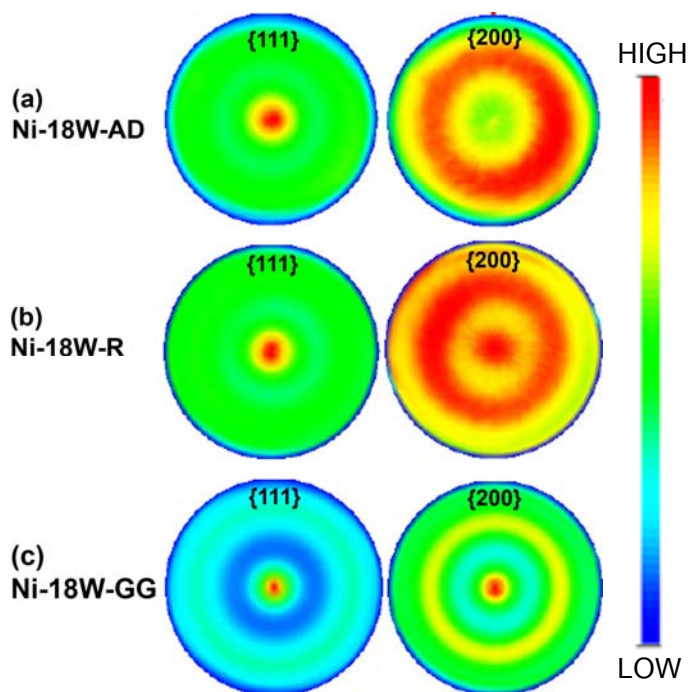


Fig. 4-14 The representative {111} and {200} X-ray diffraction pole figures of Ni-18W sample series (a) Ni-18W-AD (grain size = 7 nm), (b) Ni-18W-R (grain size = 8 nm) and (c) Ni-18W-GG (grain size = 62 nm) samples, with the surface normal vector coming out of the page. The pole figure of the Ni-18W-AD specimen exhibits strong {111}-fiber texture with {200} crystallographic planes preferentially oriented at about 45° from the surface normal. Upon annealing, both Ni-18W-R and Ni-18W-GG samples exhibit different crystallographic textures from that of Ni-18W-AD.

Figures 4-15 and 4-16 show the XPS profiles of Ni-6W and Ni-18W specimen series. The XPS analysis suggests that the surfaces of specimens in both Ni-6W (Fig. 4-15) and Ni-18W series (Fig. 4-16) contain four identical chemical species, namely, Ni metal (as indicated by Ni 2p peaks at 852.1 and 869.5 eV) (Furstenau et al., 1985: 55), Ni(OH)₂ (as indicated by Ni 2p peaks at 855.6 and 873.2 eV) (Liu et al., 2010: 083919),

W metal (as indicated by W 4f peaks at 31.0 and 33.1 eV) (Takano et al., 1989: 25) and W oxide having the oxidation state of tungsten (35.0 eV) between that of $W_{18}O_{49}$ (34.3 eV) and WO_3 (35.8 eV) (Zhang, and Macdonald, 1998: 2661). However, the relative quantity of the surface species of the specimens in Ni-6W series differs from that in Ni-18W series. The relative quantity between oxide/hydroxide and metal is comparable among different specimens in Ni-6W series. On the other hand, the relative quantity of oxide/hydroxide to metal in Ni-18W series differs noticeably from specimen to specimen.

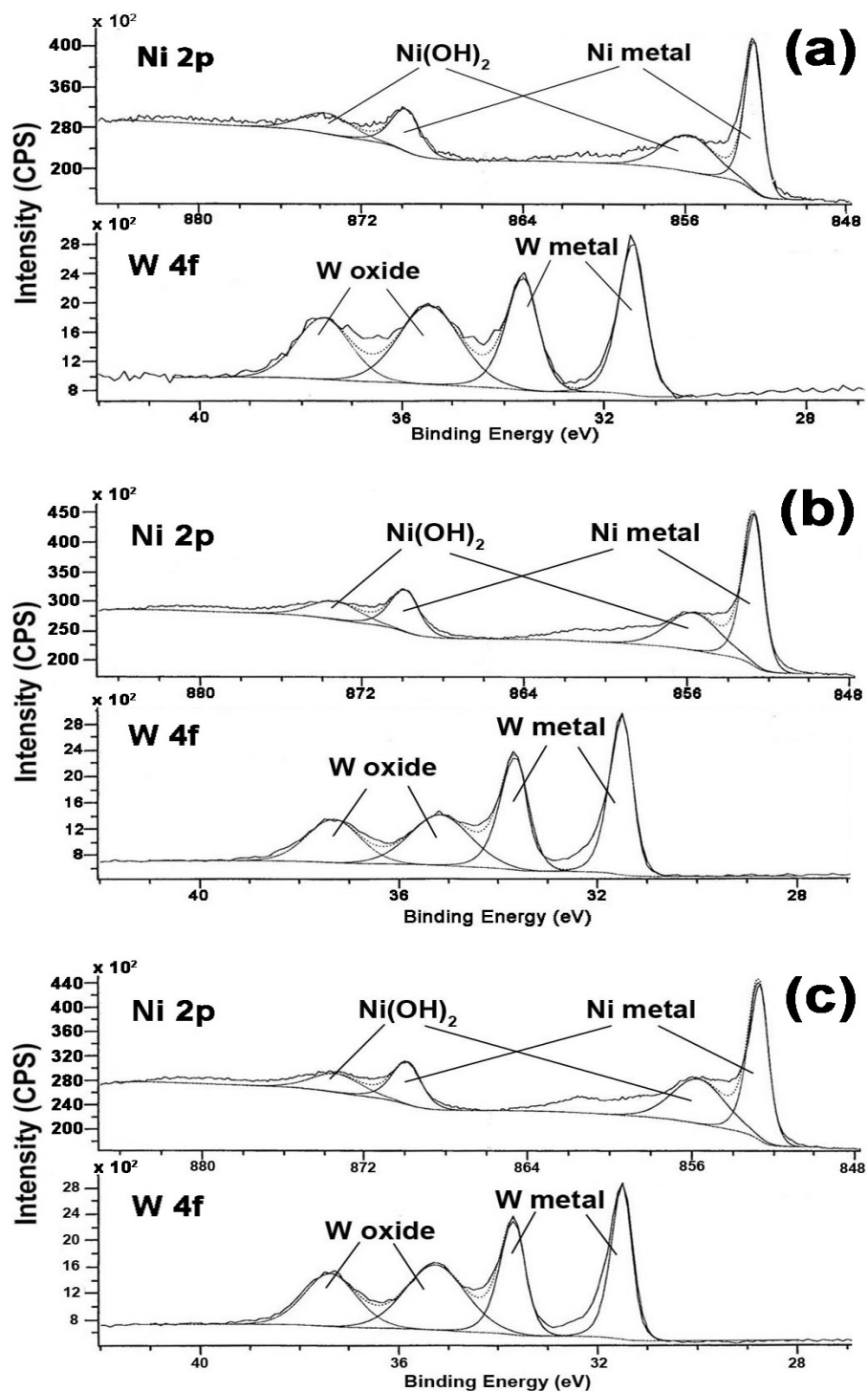


Fig. 4-15 XPS spectra of Ni-6W specimen series including (a) Ni-6W-AD, (b) Ni-6W-R and (c) Ni-6W-GG, showing similar chemical species on the surface, namely, Ni metal, Ni(OH)₂, W metal and W oxide.

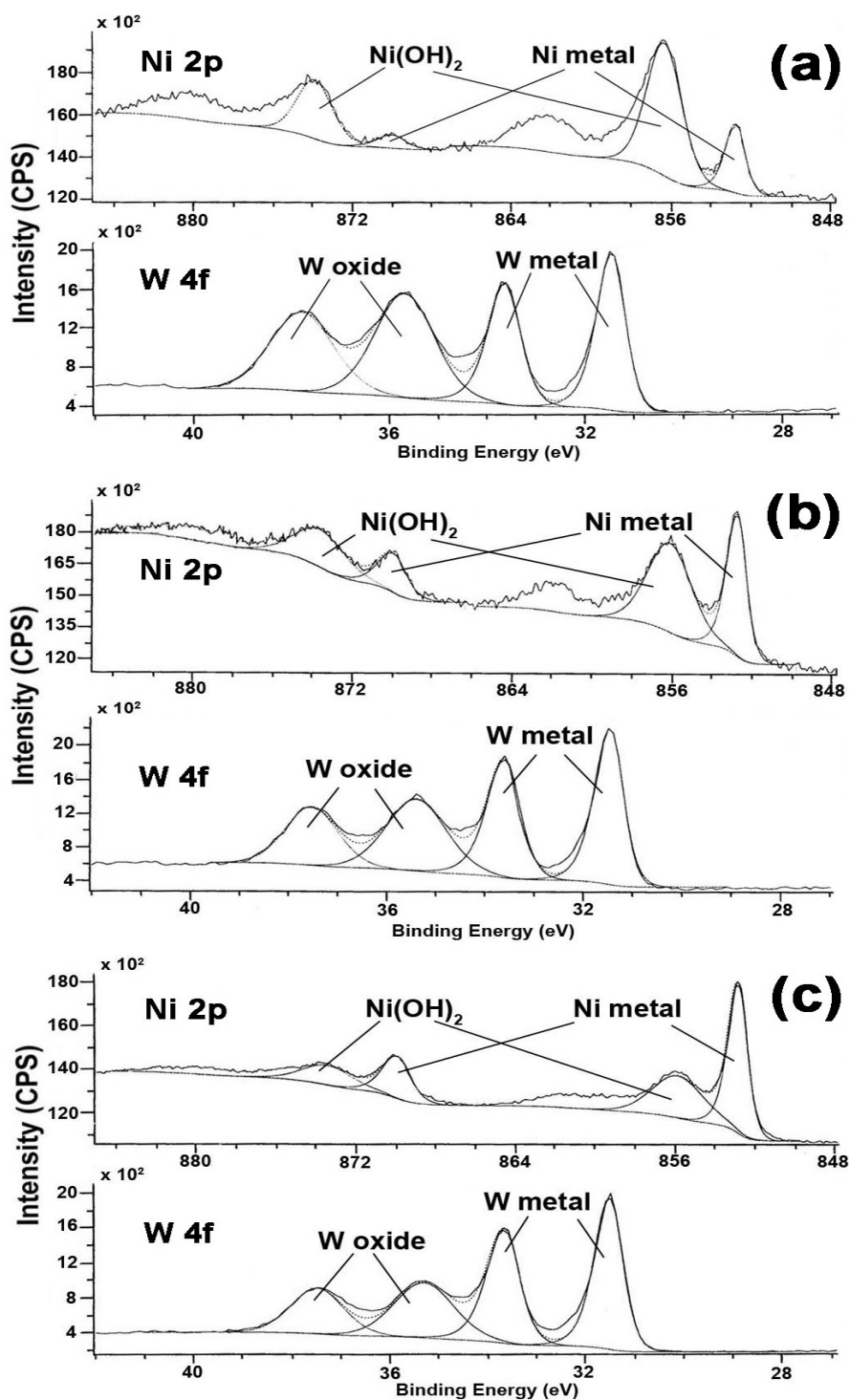


Fig. 4-16 XPS spectra of Ni-18W specimen series including (a) Ni-18W-AD, (b) Ni-18W-R and (c) Ni-18W-GG, showing similar chemical species on the surface, namely, Ni metal, Ni(OH)₂, W metal and W oxide.

2 Corrosion Behavior

Polarization curves of the Ni-6W and Ni-18W specimen series tested in 3.5 wt.% NaCl electrolyte at pH = 10 are shown in Fig. 4-17 and 4-18 and those with pH = 3 shown in Fig. 4-19 and 4-20, respectively. The polarization curves at pH = 10 and 3 are summarized in terms of i_{corr} and E_{corr} with respect to the grain size as shown in Table 4-5. The data in Table 4-5 has demonstrated that Ni-6W sample series exhibited significantly lower corrosion rates than Ni-18W series in alkaline pH = 10 and slightly higher corrosion rates than Ni-18W series in acidic pH = 3 3.5wt.% NaCl environments, conforming to the results in Part I (Fig. 4-8). In addition, the i_{corr} and E_{corr} data were also plotted as a function of grain size in order to demonstrate the impact of heat treatment (which changes the grain size of specimens) on corrosion of Ni-6W and Ni-18W specimen series in alkaline pH = 10 (Fig. 4-21 a-b) and acidic pH = 3 (Fig. 4-22 a-b) NaCl environments.

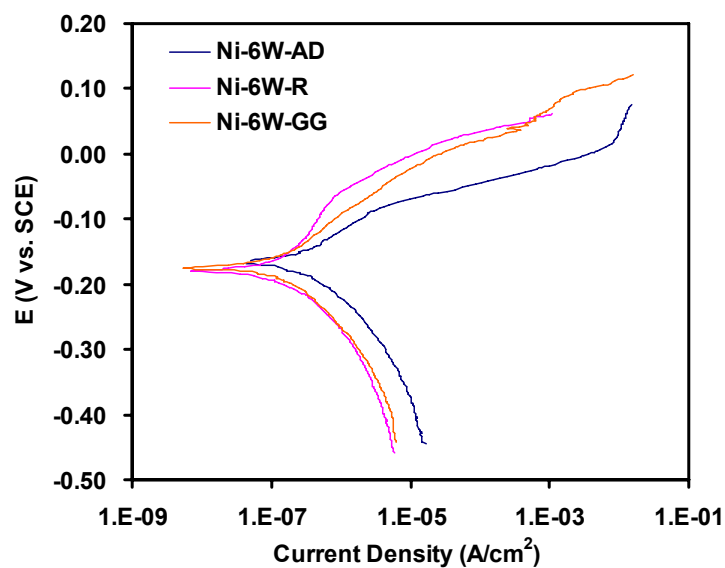


Fig. 4-17 Polarization curves of Ni-6W sample series in pH=10 3.5 wt.% NaCl solution.

Visual observation of polarization curves in Fig. 4-17 demonstrates that corrosion potentials of Ni-6W-AD, Ni-6W-R and Ni-6W-GG specimens in pH = 10 3.5 wt.% NaCl solution are similar (Table 4-5). The same observation holds true for similar corrosion rates of Ni-6W-AD and Ni-6W-GG except for the distinct corrosion rate of Ni-6W-R which is the lowest among the three specimens in Ni-6W series (Table 4-5).

Considering the cathodic parts (potential range below E_{corr}) of polarization curves in Fig. 4-17, it is evident that all the cathodic curves share similar slope, implying the same mechanism of cathodic reaction of the three specimens in pH = 10 3.5 wt.% NaCl solution (Jones, 1991: 85). However, the shift in each cathodic curve with respect to the current density axis demonstrates the different rates of cathodic reaction with Ni-6W-GG the highest and Ni-6W-AD the lowest (Jones, 1991: 89). Although the difference in cathodic reaction rates is noticeable from the polarization curves, it is less than one order of magnitude, render this difference relatively insignificant.

Considering the anodic parts (potential range above E_{corr}) of polarization curves in Fig. 4-17, it is evident that all the anodic curves indicate active corrosion process. The shift of anodic curves with respect to the current density axis indicates that the rate of anodic reaction of each specimen differs (Jones, 1991: 89).

The polarization curves in Fig. 4-18 show that Ni-18W-AD, Ni-18W-R and Ni-18W-GG exhibit active corrosion process in pH = 10 3.5 wt.% NaCl solution. Observation of polarization curves in Fig. 4-18 demonstrates that both corrosion potentials and corrosion rates of Ni-18W-AD, Ni-18W-R and Ni-18W-GG specimens in pH = 10 3.5 wt.% NaCl solution are comparable with the numerical data clearly spelled

out in Table 4-5.

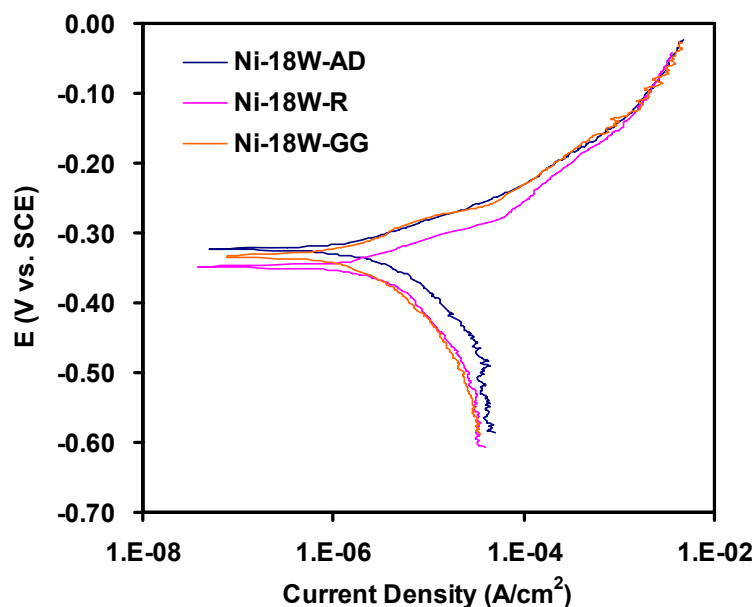


Fig. 4-18 Polarization curves of Ni-18W sample series in pH=10 3.5 wt.% NaCl solution.

Considering the cathodic parts (potential range below E_{corr}) of polarization curves of Ni-18W series in Fig. 4-18, similar to those of Ni-6W series in Fig. 4-17, it is evident that all the cathodic curves share similar slope, implying the same mechanism of cathodic reaction in pH = 10 3.5 wt.% NaCl solution (Jones, 1991: 85). However, the shift in each cathodic curve with respect to the current density axis demonstrates the different rates of cathodic reaction (Jones, 1991: 89) in pH = 10 3.5 wt.% NaCl solution with Ni-18W-GG and Ni-18W-R having the same rate and Ni-18W-AD the highest. Although the cathodic reaction rate of Ni-18W-AD differs from the rest, the distinction is less than one order of magnitude, render it relatively insignificant.

Considering the anodic parts (potential range above E_{corr}) of polarization curves of Ni-18W series in Fig. 4-18, unlike those of Ni-6W series in Fig. 4-17, it is evident that

the anodic curves of Ni-18W-AD, Ni-18W-R and Ni-18W-GG specimens possess similar slopes, imply similar anodic phenomena on each specimen in pH = 10 3.5 wt.% NaCl solution (Jones, 1991: 85). Nevertheless, the shift of anodic curves with respect to the current density axis indicates that the rate of anodic reaction of each specimen differs (Jones, 1991: 89) with that of Ni-18W-AD and Ni-18W-GG being the same and Ni-18W-R the lowest.

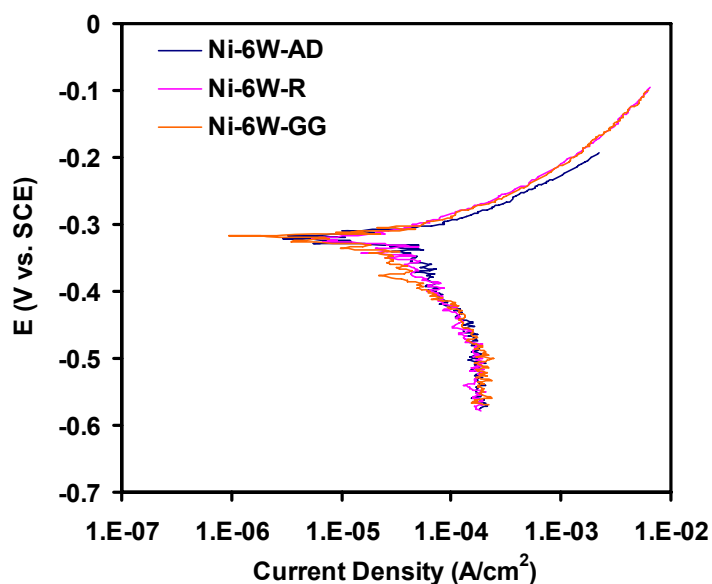


Fig. 4-19 Polarization curves of Ni-6W sample series in pH=3 3.5 wt.% NaCl solution.

The polarization curves in Fig. 4-19 show that Ni-6W-AD, Ni-6W-R and Ni-6W-GG exhibit active corrosion in pH = 3 3.5 wt.% NaCl solution without any noticeable passive process. Observation of polarization curves in Fig. 4-19 demonstrates that both corrosion potentials and corrosion rates of Ni-6W-AD, Ni-6W-R and Ni-6W-GG specimens in pH = 3 3.5 wt.% NaCl solution are comparable with the numerical data clearly tabulated in Table 4-5.

Considering the cathodic parts (potential range below E_{corr}) of polarization curves of Ni-6W series in Fig. 4-19, it is apparent that the cathodic curves of Ni-6W-AD, Ni-6W-R and Ni-6W-GG specimens overlay on top of one another and possess similar shape and slope, implying similar cathodic interfacial phenomena in pH = 3 3.5 wt.% NaCl solution at comparable rates.

Similarly, the anodic parts (potential range above E_{corr}) of polarization curves of Ni-6W series in Fig. 4-19 share similar slope, implying the same mechanism of anodic reaction in pH = 3 3.5 wt.% NaCl solution. Moreover, the anodic curves of Ni-6W-R and Ni-6W-GG overlay on top of each other with the anodic part of Ni-6W-AD shifting slightly toward lower current density. This observation implies that not only the anodic reaction mechanism is similar among the three specimens, but the rate of each is also comparable.

In line with Fig. 4-19, the polarization curves in Fig. 4-20 show that Ni-18W-AD, Ni-18W-R and Ni-18W-GG exhibit active corrosion in pH = 3 3.5 wt.% NaCl solution without any noticeable passive process. Observation of polarization curves in Fig. 4-20 also demonstrates comparable corrosion potentials and corrosion rates of Ni-18W-AD, Ni-18W-R and Ni-18W-GG specimens in pH = 3 3.5 wt.% NaCl solution as clearly shown in Table 4-5.

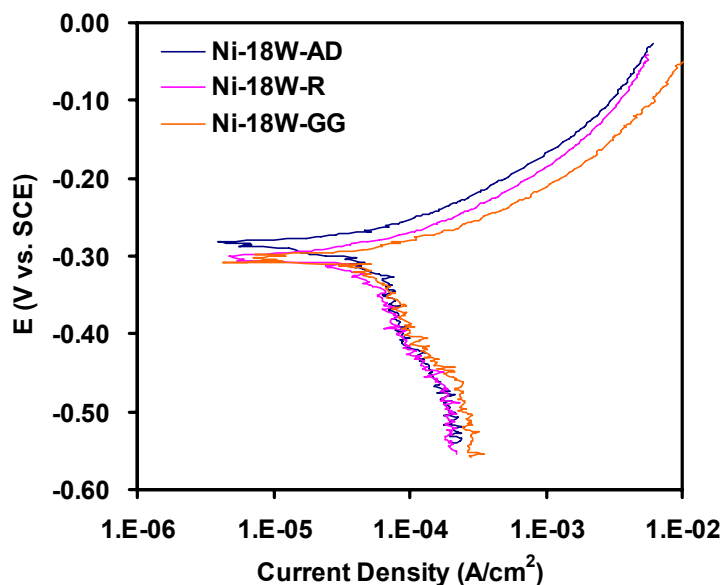


Fig. 4-20 Polarization curves of Ni-18W sample series in pH=3 3.5 wt.% NaCl solution.

Similar to what observed for Ni-6W series (Fig. 4-19), the cathodic parts (potential range below E_{corr}) of polarization curves of Ni-18W-AD, Ni-18W-R and Ni-18W-GG specimens in Fig. 4-20 overlay on top of one another and possess similar shape and slope, implying similar interfacial cathodic reaction proceeding at comparable rates in pH = 3 3.5 wt.% NaCl solution.

Likewise, the anodic parts (potential range above E_{corr}) of polarization curves of Ni-18W specimen series in Fig. 4-20 share similar shape and slope, implying the same anodic reaction in pH = 3 3.5 wt.% NaCl solution for all Ni-18W specimens. Although the anodic curves of Ni-18W-AD, Ni-18W-R and Ni-18W-GG do not overlay on top of each other, the deviation from one another is not significant, rendering the anodic reaction rate of each specimen comparable.

Table 4-5 i_{corr} and E_{corr} of Ni-6W and Ni-18W specimen series in pH=10 and 3 3.5 wt.% NaCl solutions.

Sample	Grain size (nm)	pH = 10		pH = 3	
		i_{corr} ($\mu\text{A}/\text{cm}^2$)	E_{corr} (V vs. SCE)	i_{corr} ($\mu\text{A}/\text{cm}^2$)	E_{corr} (V vs. SCE)
Ni-6W-AD	52	0.144	-0.171	26.7	-0.320
Ni-6W-R	54	0.0517	-0.172	25.7	-0.323
Ni-6W-GG	110	0.145	-0.176	26.1	-0.326
Ni-18W-AD	7	2.45	-0.322	8.86	-0.281
Ni-18W-R	8	3.45	-0.347	14.6	-0.303
Ni-18W-GG	62	1.99	-0.334	8.53	-0.301

2.1 3.5 wt.% NaCl at pH = 10

Here, the E_{corr} and i_{corr} data (Table 4-5) of annealed Ni-W specimens in pH = 10 3.5 wt.% NaCl solution were plotted as a function of grain size in order to demonstrate the impact of heat treatment (which changes the grain size of specimens) on corrosion of Ni-6W and Ni-18W specimen series in alkaline pH = 10 NaCl environments (Fig. 4-21 a-b).

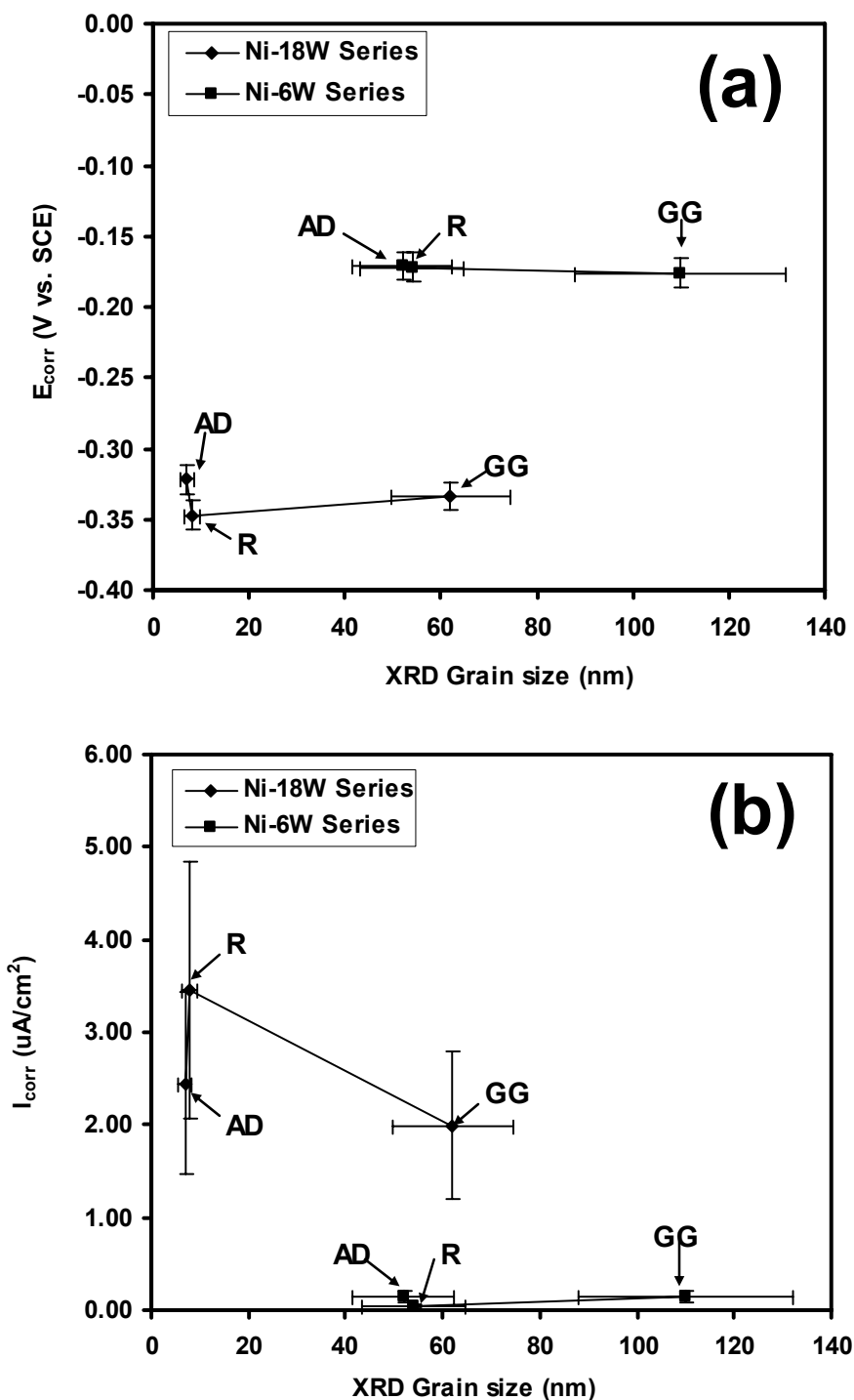


Fig. 4-21 The plots of E_{corr} (a) and i_{corr} (b) vs. grain size for Ni-6W and Ni-18W specimen series in pH=10 3.5 wt.% NaCl solution. AD denotes as-deposited. R denotes grain boundary relaxation. GG denotes grain growth.

First, consider the corrosion potentials, E_{corr} , of three specimens of Ni-6W series in pH = 10 3.5 wt.% NaCl solution (Fig. 4-21a). It is apparent that the E_{corr} values of Ni-6W-AD (grain size = 52 nm), Ni-6W-R (grain size = 54 nm) and Ni-6W-GG (grain size = 110 nm) are similar, implying the negligible effect of grain boundary relaxation in Ni-6W-R and grain growth in Ni-6W-GG on the values of E_{corr} in alkaline saline environments. A similar flat trend was also observed for corrosion potentials of the specimens in Ni-18W series in pH = 10 3.5 wt.% NaCl solution (Fig. 4-21a), implying the negligible effect of grain boundary relaxation and grain growth on the values of E_{corr} of Ni-18W sample series in alkaline saline environments. Finally, Fig. 4-21a clearly demonstrates that as a group, Ni-6W specimen series exhibit higher corrosion potentials than those of Ni-18W series.

In alkaline pH = 10 NaCl solution, the lower corrosion rates of Ni-6W sample group relative to those of Ni-18W sample series (Fig. 4-21b) are in agreement with the higher corrosion potentials of the former group relative to the latter (Fig. 4-21a). Moreover, the results here (Fig. 4-22) are also in line with the results in Part I (Fig.4-8), which demonstrate that i_{corr} of as-deposited Ni-6W is lower than that of as-deposited Ni-18W in alkaline condition. From Fig. 4-21b, the comparable i_{corr} values of samples within Ni-6W and Ni-18W series are in line with their comparable E_{corr} values as shown in Fig. 4-21a. This implies the negligible effect of grain boundary relaxation and grain growth on corrosion of Ni-6W and Ni-18W specimens in alkaline saline environments.

2.2 3.5 wt.% NaCl at pH = 3

Here, the E_{corr} and i_{corr} data (Table 4-5) of annealed Ni-W specimens in pH = 3 3.5 wt.% NaCl solution were plotted as a function of grain size in order to demonstrate the impact of heat treatment (which changes the grain size of specimens) on corrosion of Ni-6W and Ni-18W specimen series in pH = 3 NaCl environments (Fig. 4-22 a-b).

In line with the observation at pH = 10 (Fig. 21a), the E_{corr} values of three specimens within Ni-6W series in pH = 3 3.5 wt.% NaCl solution (Fig. 4-22a), namely, Ni-6W-AD (grain size = 52 nm), Ni-6W-R (grain size = 54 nm) and Ni-6W-GG (grain size = 110 nm), are similar, implying the negligible effect of grain boundary relaxation (Ni-6W-R) and grain growth (Ni-6W-GG) on E_{corr} in acidic saline environments. Similarly, a flat trend was also observed for corrosion potentials of Ni-18W specimens at pH = 3 (Fig. 4-22a), implying the negligible effect of grain boundary relaxation and grain growth on E_{corr} of Ni-18W specimens as well.

In acidic pH = 3 NaCl solution, the higher corrosion rates of Ni-6W series relative to those of Ni-18W group (Fig. 4-22b) are in agreement with the lower corrosion potentials of Ni-6W series in the same environment (Fig. 4-22a). Moreover, the results here (Fig. 4-22b) are also in line with the results in Part I (Fig.4-8), which show that as-deposited Ni-6W has higher corrosion rate than as-deposited Ni-18W in acidic saline condition. The comparable i_{corr} values of samples in Ni-6W and Ni-18W series are in line with their similar E_{corr} values shown in Fig. 4-22a. This implies the insignificant effect of grain boundary relaxation and grain growth on corrosion of Ni-6W specimens in acidic saline environments.

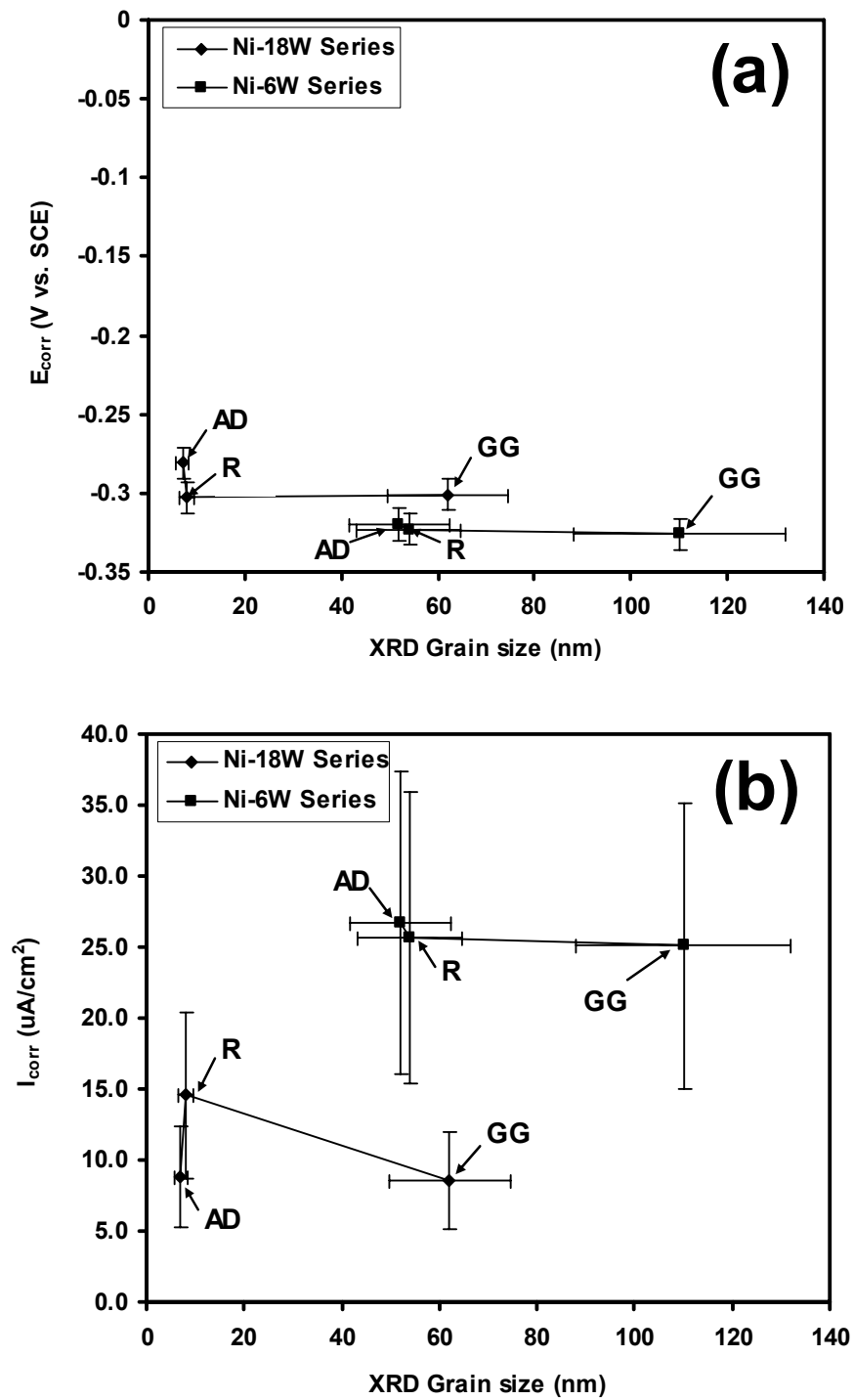


Fig. 4-22 The plots of E_{corr} (a) and i_{corr} (b) vs. grain size for Ni-6W and Ni-18W specimen series in pH=3 3.5 wt.% NaCl solution. AD denotes as-deposited. R denotes grain boundary relaxation. GG denotes grain growth.

Part III – Interfacial Corrosion Phenomena of As-Deposited and Annealed Nanocrystalline Ni-W

Now that we have seen the trends in corrosion behaviour of as-deposited Ni-W and annealed Ni-W alloys in alkaline and acidic saline environments as described in Parts I and II, respectively. In Part III, we investigate the mechanisms that govern these trends of corrosion behaviour by means of electrochemical impedance spectroscopy (EIS). The investigation was conducted in both alkaline and acidic saline environments.

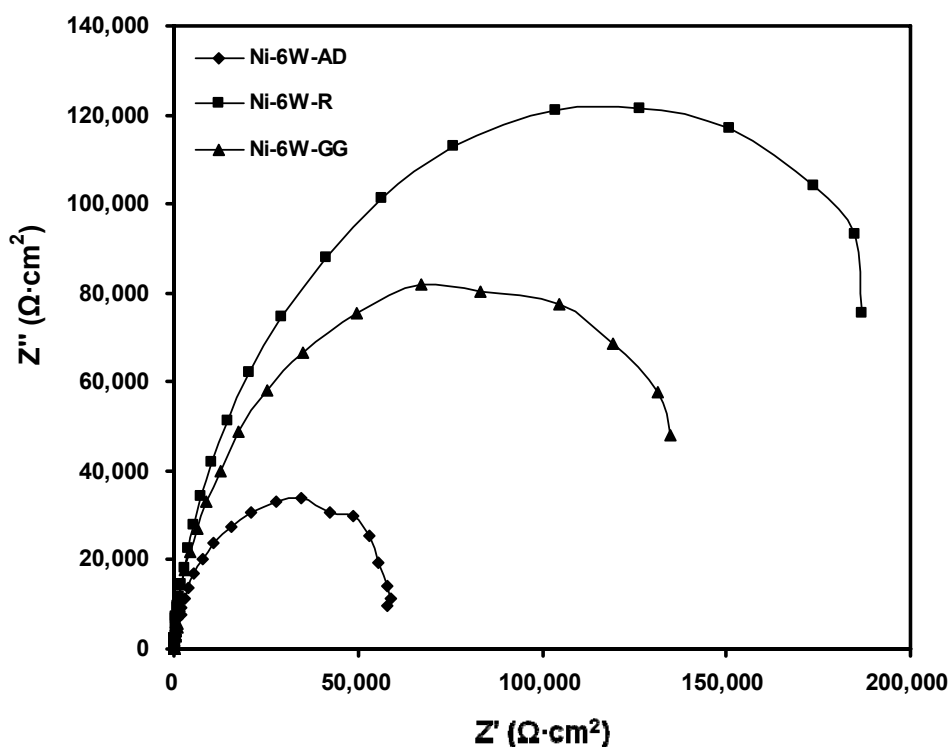


Fig. 4-23 Nyquist impedance plot of Ni-6W-AD, Ni-6W-R and Ni-6W-GG specimens in pH=10 3.5 wt.% NaCl solution.

Starting with the impedance response of Ni-6W specimen series in pH = 10 3.5 wt.% NaCl solution as shown in Fig. 4-23, the Nyquist impedance plots show clearly

distinguishable curves corresponding to each Ni-6W specimens. The similar shape of these curves suggests the similar corrosion mechanism for each specimen, while the difference in diameter of each curve indicates the variation in the magnitude of certain electrochemical parameters governing corrosion. These electrochemical parameters and their magnitudes, which can be quantified by proper analysis, will be presented later in Chapter 5. Nonetheless, despite the lack of quantitative data at this point, it can be qualitatively inferred from the Nyquist plots in Fig. 4-23 that Ni-6W-GG, which possesses the highest real impedance, should have the greatest corrosion resistance, Ni-6W-AD, which shows the lowest real impedance, should demonstrate the greatest corrosion susceptibility and the corrosion resistance of Ni-6W-R should stay between those of the former two. This observation clearly demonstrates the significant impact of grain boundary relaxation and grain growth on corrosion of Ni-6W specimens in alkaline saline environment.

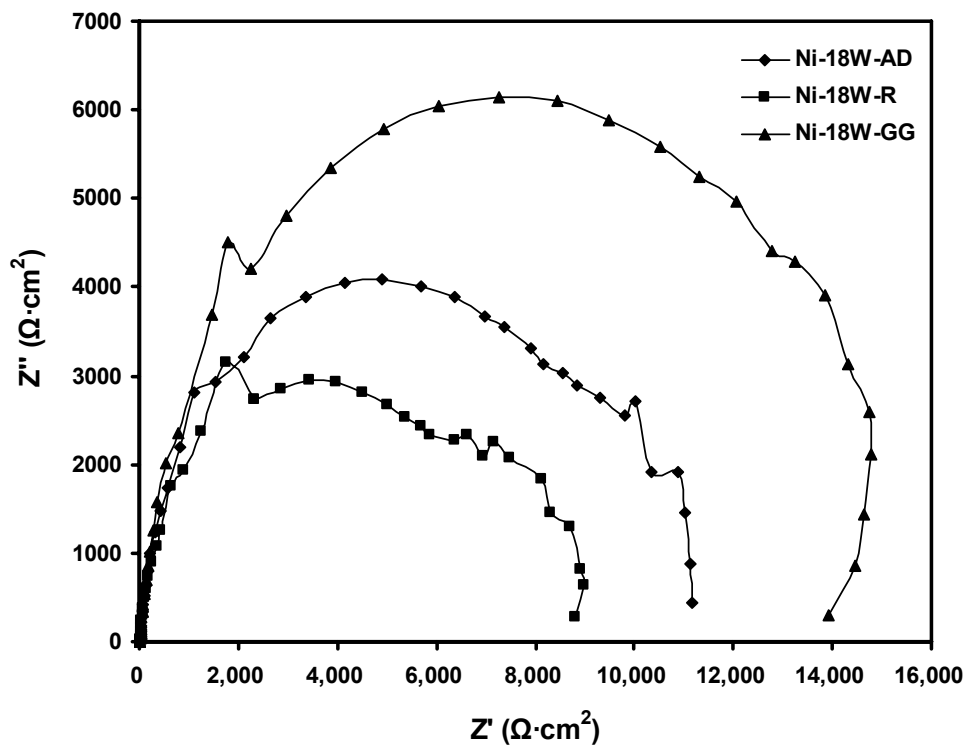


Fig. 4-24 Nyquist impedance plot of Ni-18W-AD, Ni-18W-R and Ni-18W-GG specimens in pH=10 3.5 wt.% NaCl solution.

Similar to Ni-6W specimen series, the Nyquist impedance plots of Ni-18W series in pH = 10 3.5 wt.% NaCl solution as shown in Fig. 4-24 show clearly distinct curves of similar shape, suggesting the similar corrosion phenomena occurring at the solid/electrolyte interface of each specimen. The difference in the diameter of each curve also indicates the different magnitude of certain electrochemical parameters of each specimen, which will be quantified later in Chapter 5. However, the trend in corrosion resistance of Ni-18W specimens as suggested from Fig. 4-24 differs from what observed for Ni-6W samples in the same test environment. Here, Ni-18W-GG, which possesses the highest real impedance, should remain the most resistant to corrosion.

Ni-18W-R, the specimen with grain boundary relaxation, instead of the as-deposited specimen as in the investigation of Ni-6W series, now exhibits the lowest real impedance, suggesting the lowest corrosion resistance. This observation also demonstrates the noticeable influence of grain boundary relaxation and grain growth on corrosion of Ni-18W specimens in alkaline saline environment.

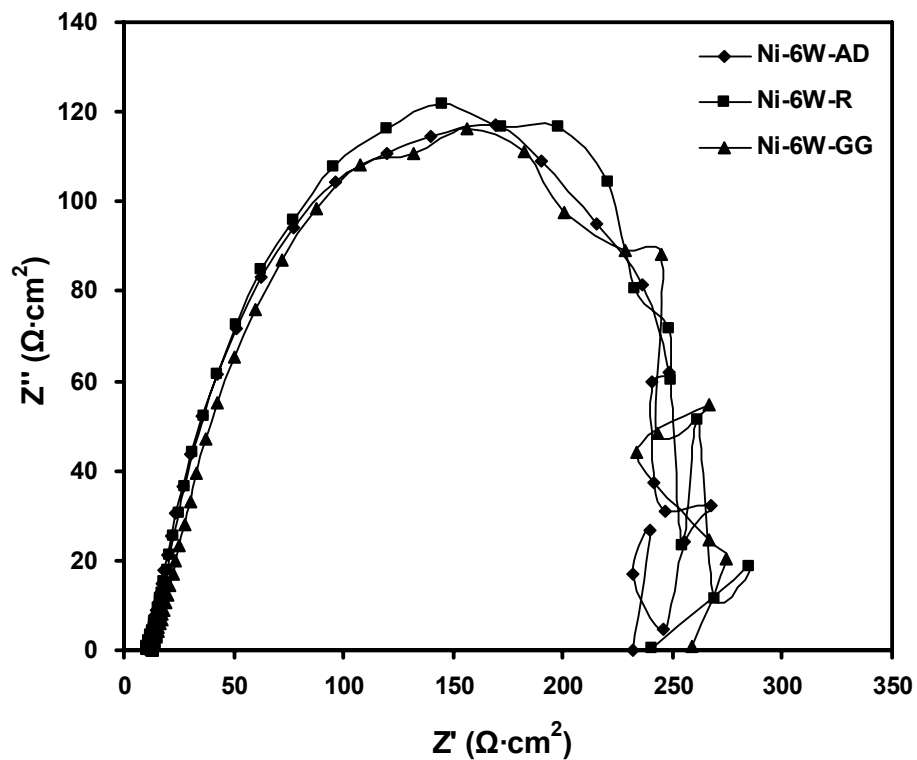


Fig. 4-25 Nyquist impedance plot of Ni-6W-AD, Ni-6W-R and Ni-6W-GG specimens in pH=3 3.5 wt.% NaCl solution.

Instead of the clearly separate impedance curves as in pH = 10 3.5 wt.% NaCl (Fig. 4-23), the Nyquist impedance plots of the Ni-6W specimens in pH = 3 3.5 wt.% NaCl solution (Fig. 4-25) nearly overlay on top of one another, suggesting both the same corrosion mechanism and similar magnitude of corrosion resistance for each Ni-6W

specimen in the acidic condition. This observation demonstrates the insignificant influence of grain boundary relaxation and grain growth on corrosion of Ni-6W specimens in acidic saline environment. Moreover, the real impedance value of each specimen in acidic saline environment (Fig. 4-25) is significantly lower than the value of the same specimen in alkaline condition (Fig. 4-23), signifying much more severe corrosion attack in the acidic environment. The great extent of corrosion of Ni-6W specimens in acidic condition may render the specimens so unstable that the measurement noise, which is absent in alkaline condition, appears noticeable in the Nyquist impedance plots (Fig. 4-25) of Ni-6W specimens in acidic condition.

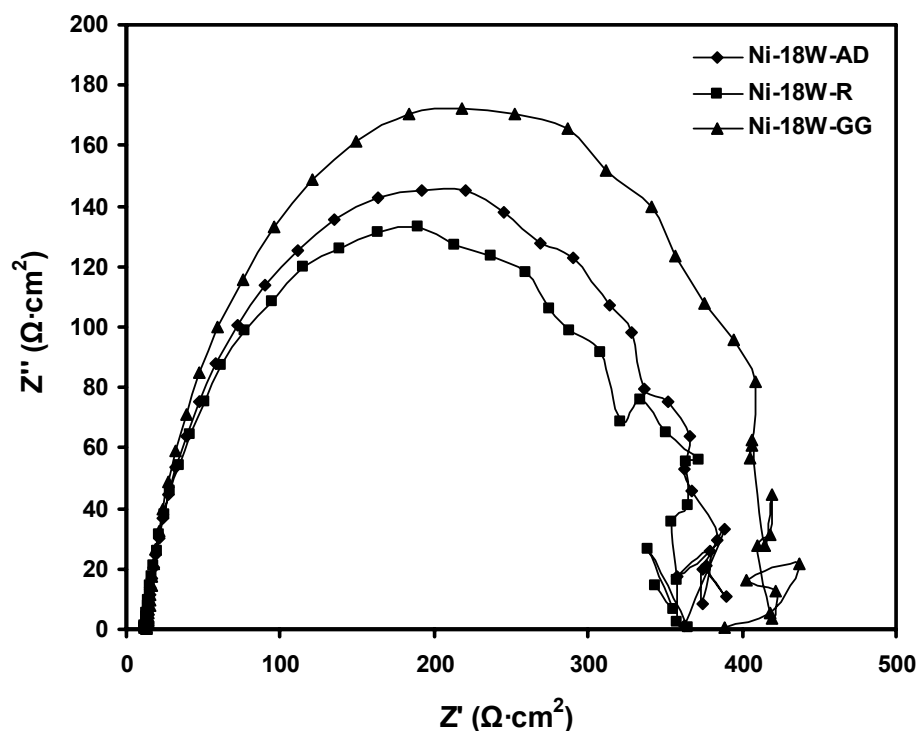


Fig. 4-26 Nyquist impedance plot of Ni-18W-AD, Ni-18W-R and Ni-18W-GG specimens in pH=3 3.5 wt.% NaCl solution.

In comparison to the impedance response in pH = 10 3.5 wt.% NaCl (Fig. 4-24), the Nyquist impedance plots of the Ni-18W specimens in pH =3 3.5 wt.% NaCl solution (Fig. 4-26) still have similar shape, but spread out to a relatively insignificant extent, suggesting the same corrosion mechanism and comparable magnitude of corrosion resistance for each Ni-6W specimen in acidic condition. This observation demonstrates the minor impact of grain boundary relaxation and grain growth on corrosion of Ni-18W specimens in acidic saline environment. Moreover, the real impedance value of each specimen in acidic saline environment (Fig. 4-26) is significantly lower than the value of the same specimen in alkaline condition (Fig. 4-24), suggesting much greater corrosion susceptibility in the acidic environment. The relative large extent of corrosion of Ni-18W specimens in acidic condition may cause some measurement noise to appear in the Nyquist impedance plots (Fig. 4-26).

CHAPTER V

DISCUSSION

This chapter is divided into three parts including Part I – Corrosion of As-Deposited Nanocrystalline Ni-W, Part II – Corrosion of Annealed Nanocrystalline Ni-W and Part III – Interfacial Corrosion Phenomena of As-Deposited and Annealed Nanocrystalline Ni-W.

Part I – Corrosion of As-Deposited Nanocrystalline Ni-W

1 As-Deposited Nanocrystalline Ni-W

An increase of W solute content in Ni generally leads to grain size reduction, as the incorporated W atoms segregate to the grain boundaries of Ni and stabilize the grain structure (Detor, and Schuh, 2007a: 371). In the pulse current electrodeposition, during the forward pulse, the substrate is a cathode, on which nickel ions and nickel tungstate complex are concurrently reduced and co-deposited to form Ni-W alloys (Eliaz, Sridhar, and Gileadi, 2005: 2893; Eliaz, and Gileadi, 2007: 337). During the reverse pulse, the substrate becomes an anode, where electroactive W atoms are preferentially stripped off from the deposit and dissolve back into the electroplating bath (Detor, and Schuh, 2007a: 371). As a result, as shown in Fig. 4-1, the increase of reverse current density leads to a reduction of W content in the Ni-W alloys and consequently an increase in grain size. Using the reverse pulsing technique, a spectrum of grain sizes is therefore effectively achieved for the subsequent corrosion study.

The corrosion test results reveal some key insights concerning the relationship between the characteristics of the nickel alloys and their corrosion resistance in alkaline and acidic NaCl solutions. Several factors could contribute to the corrosion resistance of nanocrystalline Ni-W, including tungsten solute content, grain size, and crystallographic texture, and these parameters vary together in the present set of experiments. While an increase of tungsten content in nickel has been noted to promote the formation of a mixed oxide film that increases corrosion resistance (Sriraman et al., 2007a: 39), it also leads to finer grains (more grain boundaries) (Detor, and Schuh, 2007a: 371), providing more active surface sites for corrosion reactions (Rofagha et al., 1991: 2867, 1993: 1; Wang et al., 1995: 224). Thus the competing effects of W content and grain size evidently govern the corrosion behaviour of nanocrystalline Ni-W alloys. Furthermore, corrosive attack may be facilitated in a structure textured to promote off-{111}. The {111}-oriented grains generally show relatively higher corrosion resistance than other orientations in Ni, not only because of the tight binding along close packed directions (Park, and Szpunar, 1998: 525; Schuh et al. 2003b: 183; Asgari, Toroghinejad, and Golozar, 2007: 6769), but also due to the tenacity of the oxide layer in this orientation (Schuh et al., 2003b: 183). With these relevant contributions, the corrosion behaviours of nanocrystalline Ni-W and microcrystalline Ni in the acidic and alkaline saline environments may be elucidated as follows.

2 Corrosion Behavior

2.1 3.5 wt.% NaCl at pH = 10

The results (Fig. 4-8) show that the corrosion rate of nanocrystalline Ni-W in pH = 10 NaCl initially decreases with the reduction of grain size from 63 to 39 nm. This may be attributed to a transition of the crystallographic texture from a principal {200} fiber (with some in-plane alignment as well) in Ni-5W (63 nm) to more uniformly-distributed components in Ni-6W (39 nm) (Fig. 4-3); this shift brings a higher density of {111} poles into alignment with the surface normal, which improves corrosion resistance. Thereafter, i_{corr} increases with the simultaneous increase in tungsten content (~6 to 22 at.%) and decrease in grain size (from 39 to 5 nm.) Over this range we expect the texture to remain predominantly {111} fiber based on the pole figures of Ni-18W (6 nm) in Fig. 4-3, so the change in corrosion properties could more likely be attributed to the increasing tungsten content and the reduction of grain size.

To understand the corrosion trend and the factors controlling corrosion for the grain size ranging from 39 to 5 nm (~6 to 22 at.%W), first, consider the effect of grain size on corrosion of as-deposited nanocrystalline Ni-W. As grain size decreases, the grain boundary volume fraction serving as active sites for corrosion reaction becomes increasing and thereby leads to higher i_{corr} . The effect of tungsten content on corrosion of as-deposited nanocrystalline Ni-W also follows the similar trend. Since tungsten has poor corrosion resistance in alkaline condition (Pourbaix, 1974: 555), addition of tungsten alloying element tends to increase i_{corr} . Fig. 4-8 shows that as-deposited

nanocrystalline Ni-W with increasing tungsten content and decreasing grain size has increasing i_{corr} . This corrosion trend is in line with the effect of grain size and tungsten content on corrosion in alkaline condition. Consequently, based on the evidence thus far, both grain size and tungsten content must be the factors controlling corrosion of as-deposited nanocrystalline Ni-W alloys in alkaline condition.

It is also informative to compare the corrosion behaviours of nanocrystalline Ni-W and microcrystalline Ni. The major distinctions between the two are best shown by i_{corr} and i_{pass} . In prior studies, the lower i_{corr} and i_{pass} of microcrystalline Ni have been attributed to its smaller number of active grain boundary sites on the surface for the corrosion reaction (Rofagha et al., 1991: 2867). The lower i_{corr} of microcrystalline Ni indicates that the uniform corrosion rate of microcrystalline Ni is lower than those of nanocrystalline Ni-W alloys (Fig. 4-8). However, this is not the case for the localized corrosion resistance. The optical micrographs of microcrystalline Ni and Ni-18W after the potentiodynamic scans as shown in Fig. 4-9 show superior localized corrosion resistance of the nanocrystalline deposits, which aligns with prior studies on nanocrystalline Ni (Rofagha et al., 1993: 1). Some authors attributed this beneficial property of nanocrystalline materials to the high surface fractions of grain boundaries and triple junctions providing an increased number of preferential attack sites, which distribute the corrosion damage so broadly that individual pits are no longer favoured (Rofagha et al., 1993: 1; Wang et al., 1995: 224).

2.2 3.5 wt.% NaCl Solution at pH = 3

Unlike the trend observed in the alkaline condition, the results in Fig. 4-8 show that the corrosion rate of nanocrystalline Ni-W in pH = 3 NaCl decreases with grain size over the range 63 to 5 nm. To understand this trend in corrosion behaviors, the competing effects of grain size and tungsten content must be considered.

First, consider the effect of grain size on corrosion as-deposited nanocrystalline Ni-W. As grain size decreases, the fraction of grain boundary volume, which serves as the active site for corrosion reaction, increases and leads to higher corrosion rate with the reduction of grain size. Nonetheless, Fig. 4-8 shows that corrosion rate of as-deposited nanocrystalline Ni-W actually decreases with the reduction of grain size. Consequently, grain size must not be the factor controlling corrosion of as-deposited nanocrystalline Ni-W in acidic regime.

The attention is then shifted to the effect of tungsten content on corrosion. Note that tungsten, in contrast to most metals, has higher corrosion resistance in acidic than in alkaline condition (Pourbaix, 1974: 555). Consequently, addition of tungsten alloying element should increase corrosion resistance of as-deposited nanocrystalline Ni-W in acidic condition. Fig. 4-8 shows that corrosion rate (i_{corr}) actually decreases with the increasing tungsten content, suggesting tungsten content as the dominating factor controlling corrosion of as-deposited nanocrystalline Ni-W in acidic condition.

It is informative to compare the corrosion behaviours of nanocrystalline Ni-W and microcrystalline Ni (Fig. 4-7). The key distinctions between the two are shown by the lower i_{corr} and i_{pass} of microcrystalline Ni relative to nanocrystalline Ni-W. As discussed

previously, these different behaviours may be attributed to a relatively low number of active grain boundary sites on the surface of microcrystalline Ni (Rofagha et al., 1991: 2867, 1993: 1; Wang et al., 1995: 224). Similar to the results found in the pH = 10 condition, microcrystalline Ni suffered localized corrosion attack while nanocrystalline Ni-W experienced uniform corrosion in the pH = 3 saline environment (Fig. 4-9). This may again underscore the influence of the relatively high number of preferential attack sites suppressing localized corrosion in nanocrystalline alloys.

3 Concluding Remarks

The findings in Part I can be summarized as follows:

- This study has demonstrated that nanocrystalline Ni-W alloys with an average grain size between 5 and 63 nm generally exhibit higher corrosion rates in acidic pH = 3 than in alkaline pH = 10 3.5 wt.% NaCl environments.
- The corrosion rates of nanocrystalline Ni-W appear to be controlled by three main factors – (i) the tungsten content, which promotes the formation of a corrosion resistant oxide film, (ii) the volume of grain boundaries, which serve as active surface sites for corrosion reaction and (iii) the tight binding atoms in close-packed {111} crystallographic texture, which tends to have higher resistance to corrosion.
- In the alkaline saline environment, with the exception of nanocrystalline Ni-W of a relatively large grain size which exhibits a strong preferred orientation with a {200} fiber, the corrosion rate of nanocrystalline Ni-W generally

increases with the reduction of grain size and increasing tungsten content (Fig. 4-8), suggesting that the increase of both grain boundary volume and tungsten content as the dominating factors controlling i_{corr} in this condition.

- On the contrary, in the acidic saline environment, the corrosion rate of nanocrystalline Ni-W decreases with the reduction of grain size (Fig. 4-8), implying that the higher W content associated with stronger film formation is the dominating factor controlling i_{corr} .
- With high surface fractions of grain boundary and triple junctions, nanocrystalline Ni-W alloys resist localized attack significantly better than microcrystalline Ni (Fig. 4-9).

Part II – Corrosion of Annealed Nanocrystalline Ni-W

1 Annealed Ni-W Specimens

Two specimen series, namely, Ni-6W and Ni-18W series, consisting of as-deposited, grain-boundary-relaxed and grain-grown specimens were successfully produced by thermal annealing as demonstrated in Chapter 4. Each specimen series were produced from the specimen with the different initial grain size which is controlled by the segregation of tungsten solute atoms to grain boundaries. During processing by heat treatment, it has been demonstrated that thermal annealing has an impact on crystallographic texture of Ni-6W and Ni-18W specimens as indicated by the change in crystallographic texture within each specimen series (Fig. 4-13 and 4-14). Consequently,

the effect of the crystallographic texture on corrosion will be included in the discussion of results. Regarding the surface compositions, the XPS spectra suggest that the surface compositions of Ni-6W specimen series are negligibly affected by thermal annealing (Fig. 4-15). Nonetheless, thermal annealing noticeably influences the surface compositions of Ni-18W specimens (Fig. 4-16). These interrelationships between grain size, tungsten content, crystallographic texture, grain boundary relaxation and grain growth create the variation of corrosion behaviors of annealed Ni-W alloys in 3.5 wt.% NaCl solution at pH = 10 and 3 as will be demonstrated in Part II.2.

2 Corrosion Behavior

2.1 3.5 wt.% NaCl Solution at pH = 10

In Part II, the results (Fig. 4-21b) demonstrate that Ni-6W series, as a group, have lower corrosion rates than Ni-18W series, in line with the results in Part I (Fig. 4-8). Since both Ni-6W and Ni-18W series have {111} dominant crystallographic texture, the texture does not play a role in their different corrosion rates.

Fig. 4-21b shows that grain boundary relaxation and grain growth have negligible effect on corrosion rates of samples with the same tungsten content. That is, the corrosion rates of Ni-6W samples remain nearly constant regardless of the heat treatment conditions of the specimens. Similarly, the corrosion rates of Ni-18W samples seem to be unchanged (varying within the error bar of measurement) upon grain boundary relaxation and grain growth. Upon grain growth, the intercrystalline volume

fraction of Ni-18W specimens decreases significantly as grain size increases from 8 (Ni-18W-R) to 62 nm (Ni-18W-GG) (Fig. 5-1). This significant change in grain boundary volume fraction, however, seems to impose insignificant impact on corrosion.

The evidence shown in this part rules out the effect of grain size on corrosion of nanocrystalline Ni-W in alkaline condition. With this additional evidence, the explanation of corrosion of nanocrystalline Ni-W alloys in Part I can be further refined as follows. In alkaline condition, the corrosion rate of electrodeposited nanocrystalline Ni-W is mainly controlled by the shift in crystallographic texture for grain size above 39 nm and by the tungsten content for grain size below 39 nm.

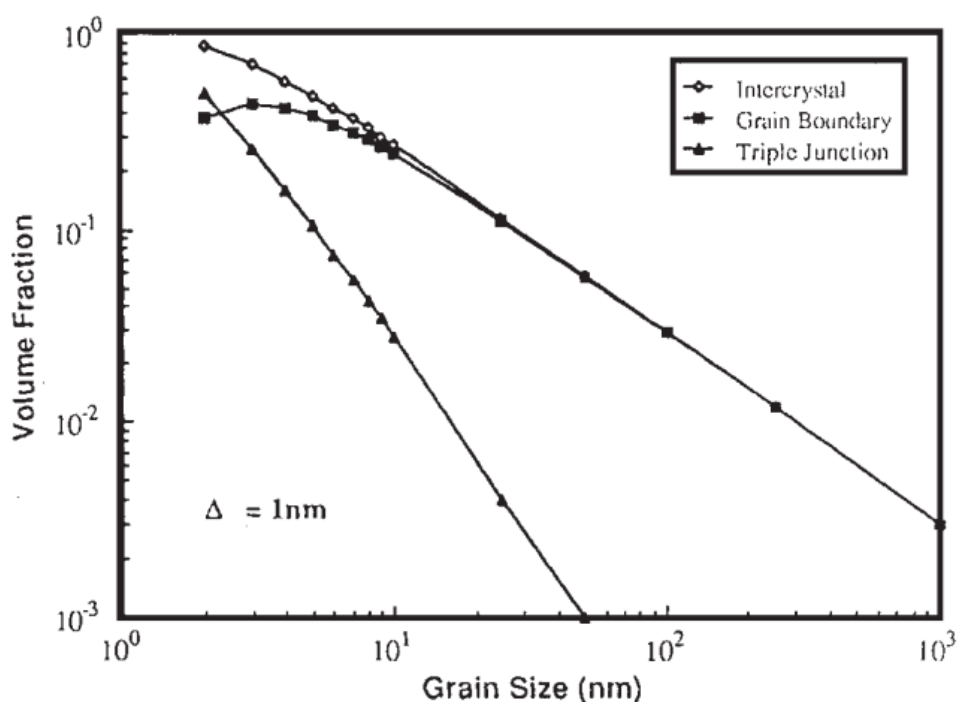


Fig. 5-1 The effect of grain size on calculated volume fractions for intercrystalline regions, grain boundaries, and triple junctions, assuming a grain boundary thickness of 1 nm (Palumbo, Thorpe, and Aust, 24(1990): 1347).

2.2 3.5 wt.% NaCl Solution at pH = 3

In Part I, in acidic condition, W content and W oxide film formation are the dominant factors controlling corrosion rate. The higher W content leads to the lower corrosion rate. In Part II, the results (Fig. 4-22b) demonstrate that Ni-6W series, as a group, have higher corrosion rates than Ni-18W series due to the lower tungsten content of the former sample series (Pourbaix, 1974: 555), in line with the results in Part I.

Fig. 4-22b shows that grain boundary relaxation has minor effect, but grain growth has significant effect on corrosion rates of Ni-6W and Ni-18W specimens. The former series clearly exhibit a flat corrosion trend, while the latter shows the variation of i_{corr} within the measurement error bar. This observation further confirms that tungsten content, not grain size, is the main factor controlling corrosion of electrodeposited nanocrystalline Ni-W in acidic regime.

3 Concluding Remarks

The findings in Part II can be summarized as follows:

- Thermal annealing imposes an impact on crystallographic texture of nanocrystalline Ni-W alloys (Fig. 4-13 and 4-14).
- In part II, it is demonstrated that grain size and grain boundary relaxation has insignificant effect on corrosion of electrodeposited nanocrystalline Ni-W in alkaline and acidic conditions.
- Based on additional evidence in Part II, it can be concluded that (i) tungsten content is the main factor controlling corrosion rate of electrodeposited

nanocrystalline Ni-W in acidic condition and (ii) in alkaline condition, corrosion rate of electrodeposited nanocrystalline Ni-W is mainly controlled by tungsten content for grain size below 39 nm (~ 6 at.% W) and by the shift in crystallographic texture for grain size above 39 nm.

Part III – Interfacial Corrosion Phenomena of As-Deposited and Annealed Nanocrystalline Ni-W

1 Circuit Analog and the Interfacial Model

The Nyquist plots of all the Ni-W specimens investigated exhibit a single semicircle (Fig. 4-23 to 4-26), indicative of the corrosion mechanism controlled only by a charge transfer step. To account for the charge transfer controlled mechanism, an equivalent circuit model (Sriraman et al., 2007a: 39; Wang et al., 2006: 657) consists of the solution resistance (R_s) connected in series with a parallel combination of a double layer capacitance (C_{dl}) and a charge transfer resistance (R_{ct}) is proposed to simulate electrochemical phenomena at the metal/electrolyte interface. Such equivalent-circuit model is found to offer a fairly good fit for the impedance data of the nanocrystalline Ni-W specimens investigated in this thesis. Thus this circuit analog (Fig. 5-2) is adopted for the description of the corrosion behavior of the nanocrystalline Ni-W coatings in pH = 10 and 3 3.5 wt.% NaCl solutions, where every element has its physical meaning. Accordingly, the impedance response generated from the electrochemical reactions of Ni-W alloys in aerated 3.5 wt.% NaCl solution at pH = 10 and 3 can be expressed as

follows (Dorf, and Svoboda, 2006: 51):

$$Z = R_s + (1/R_{ct} + j\omega C_{dl})^{-1} \quad \text{Eq. 5-1}$$

where Z = impedance measured in $\Omega \cdot \text{cm}^2$

R_s = resistance of test solution measured in $\Omega \cdot \text{cm}^2$

R_{ct} = charge transfer resistance measured in $\Omega \cdot \text{cm}^2$

C_{dl} = double layer capacitance measured in F/cm^2

ω = frequency of voltage perturbation in radian/s

Rearrange Eq. 5-1 to obtain Eq. 5-2:

$$Z = R_s + R_{ct}/(1 + (\omega R_{ct} C_{dl})^2) + j(-\omega R_{ct}^2 C_{dl})/(1 + (\omega R_{ct} C_{dl})^2) \quad \text{Eq. 5-2}$$

The 1st term of Eq.5-2 is the solution resistance. The 2nd term shows the real component of impedance. The last term is the imaginary part of impedance. With appropriate numerical algorithm (available in commercial software, for example, Autolab FRA, NOVA, etc.), the values of R_{ct} and C_{dl} that offer the best fit for the experimental impedance spectra can be computed.

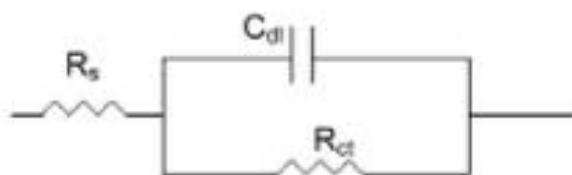


Fig. 5-2 The circuit analog of the corrosion process of Ni-6W and Ni-18W series in aerated 3.5 wt.% NaCl solution at pH = 10 and 3. The circuit element, R_s , represents the resistance of test solution; R_{ct} represents the charge transfer resistance at the metal/electrolyte interface; C_{dl} represents the capacitance of the electrical double layer formed at metal/electrolyte interface (Sriraman et al., 2007a: 39; Wang et al., 2006: 657).

Fig. 5-3 clearly illustrates the electrochemical phenomena represented by the proposed circuit analog (Fig. 5-2). From Fig. 5-3, it is apparent that the parallel combination of charge transfer resistance (R_{ct}) and double layer capacitance (C_{dl}) mimics the electrochemical phenomena at the interface between the sample surface and the test electrolyte, while the solution resistance (R_s) is attributed solely to the electrochemical phenomena in bulk electrolyte. R_s , which are in the order of $10 \Omega \cdot \text{cm}^2$ for the test solutions of all electrochemical experiments, indicates the ability of the test electrolyte to resist (or conduct) the flow of electric current; it does not affect the corrosion phenomena at the interface. However, R_s must be maintained at low magnitude so that the impedance response generated at the interface can be clearly observed. Since R_s does not provide any information about the interfacial corrosion mechanisms, it will not be discussed further. Instead, the parallel combination of R_{ct} and C_{dl} which mimics the interfacial phenomena will become our focus in the attempt to elucidate the corrosion mechanisms of Ni-W alloys in aerated alkaline and acidic saline environments.

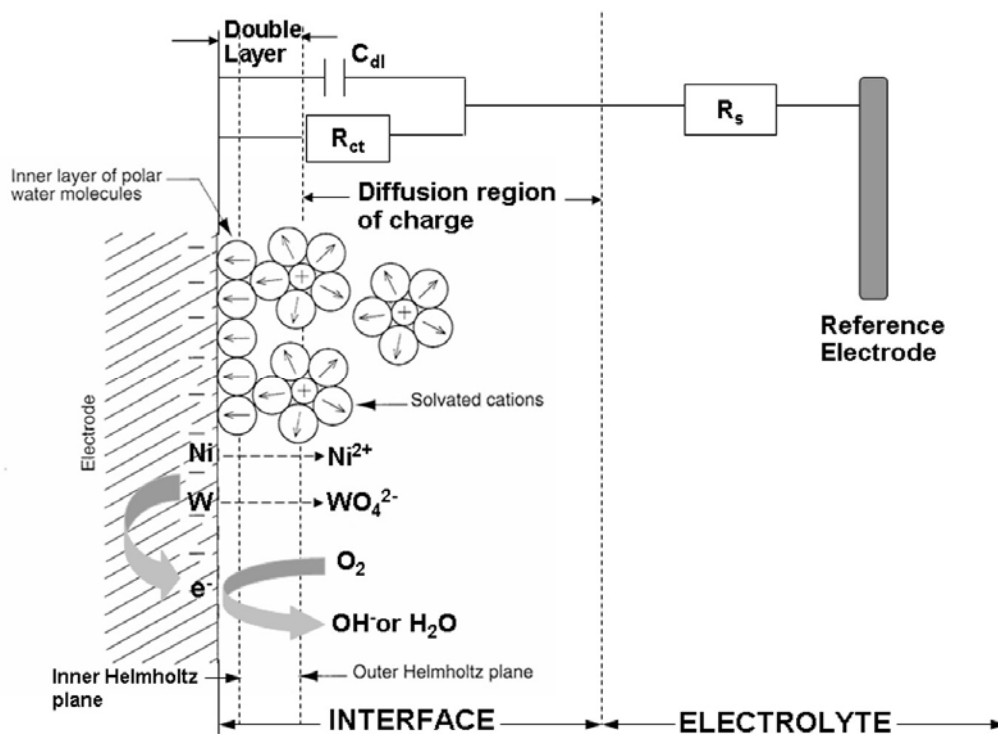


Fig. 5-3 Representative model of interfacial phenomena occurring during corrosion of nanocrystalline Ni-W alloys in aerated alkaline and acidic saline environments (Gileadi et al., 1975: 89, Jones, 1991: 101; Orazem, and Tribollet, 2008: 142).

The origin of C_{dl} will be first discussed. As illustrated in Fig. 5-3, when metal electrodes, which are Ni-W samples in our case, are immersed in an aqueous electrolyte, a monolayer of polar water molecules will be adsorbed onto the electrode surface. This monolayer of adsorbed water molecules is termed “inner Helmholtz plane” (Jones, 1991: 101). The second layer immediately adjacent to the monolayer of adsorbed water molecules is the monolayer of solvated cations, which are solvated Na^+ cations, in our case. This monolayer of solvated cations is termed “outer Helmholtz plane” and forms a plane of positive charge (Jones, 1991: 101). By Coulombic attraction,

the plane of positive charge induces the free electrons within the metal electrode to concentrate at the electrode surface (Halliday et al., 2005: 230), forming the plane of negative charge. In effect, the parallel planes of opposite charges create an atomic-scale capacitor at the metal/electrolyte interface, giving rise to the capacitive impedance response, C_{dl} , during the EIS experiments (Orazem, and Tribollet, 2008: 142).

The second parameter that characterizes the metal/electrolyte interface is the charge transfer resistance, R_{ct} . As suggested by its name, R_{ct} reflects the kinetics of the oxidation and reduction reactions on the electrode surface. Low R_{ct} indicates fast kinetics or high corrosion rate and high R_{ct} suggests otherwise. For the system of Ni-W alloys in aerated saline environments (Fig. 5-3), the measured R_{ct} is the combined consequence of the following oxidation and reduction reactions (Table 5-1), which slightly differ for alkaline and acidic conditions.

Table 5-1 List of oxidation and reduction reactions on the surfaces of Ni-W specimens in aerated alkaline and acidic saline environments (Vasko, 1985: 239; Anik, and Osseo-Asare, 2002: B224; Vanysek, 2006: 534)

Oxidation	Reduction
<p><u>Alkaline:</u></p> $\text{Ni} = \text{Ni}^{2+} + 2\text{e}^-$ $\text{W} + 8\text{OH}^- = \text{WO}_4^{2-} + 4\text{H}_2\text{O} + 6\text{e}^-$	<p><u>Alkaline:</u></p> $\text{O}_2 + 2\text{H}_2\text{O} + 4\text{e}^- = 4\text{OH}^-$
<p><u>Acidic:</u></p> $\text{Ni} = \text{Ni}^{2+} + 2\text{e}^-$ $\text{W} + 4\text{H}_2\text{O} = \text{WO}_4^{2-} + 8\text{H}^+ + 6\text{e}^-$	<p><u>Acidic:</u></p> $\text{O}_2 + 4\text{H}^+ + 4\text{e}^- = 2\text{H}_2\text{O}$

Fitting the impedance spectra with the circuit analog (Fig. 5-2) yields the R_{ct} and C_{dl} values of Ni-6W and Ni-18W series in 3.5 wt.% NaCl solution at pH = 10 and 3 as shown in Table 5-2. Note that the R_{ct} values of Ni-6W and Ni-18W groups of specimens in alkaline condition are 2-3 and 1-2 orders of magnitude larger than those of the same samples in acidic condition, suggesting the greater tendency of as-deposited and annealed Ni-W alloys to corrode in acid. Comparison of R_{ct} values between Ni-6W and Ni-18W groups demonstrates that Ni-6W group exhibit higher corrosion resistance than Ni-18W group in both acidic and alkaline conditions (Table 5-2). Both Ni-6W and Ni-18W sample series exhibit higher double-layer capacitance in acidic than in alkaline conditions, with the C_{dl} of Ni-6W series in acidic condition being the highest (Table 5-2). However, the C_{dl} values do not differ so significantly relative to the variation in the R_{ct} values. To visually illustrate the trends of C_{dl} and R_{ct} , the C_{dl} values vs. grain size were shown in Fig. 5-4 and R_{ct} values vs. grain size were shown in Fig. 5-5 and 5-6.

Table 5-2 Electrochemical impedance data of Ni-6W and Ni-18W series in pH =10 and 3 3.5 wt.% NaCl solutions

Sample	Grain size (nm)	pH = 10		pH = 3	
		R_{ct} ($\Omega \cdot \text{cm}^2$)	C_{dl} ($\mu\text{F}/\text{cm}^2$)	R_{ct} ($\Omega \cdot \text{cm}^2$)	C_{dl} ($\mu\text{F}/\text{cm}^2$)
Ni-6W-AD	52	6.23×10^4	17.1	218	226
Ni-6W-R	54	2.22×10^5	18.2	233	235
Ni-6W-GG	110	1.54×10^5	18.4	226	225
Ni-18W-AD	7	1.11×10^4	27.8	340	64.2
Ni-18W-R	8	8.51×10^3	30.1	321	62.0
Ni-18W-GG	62	1.45×10^4	26.8	380	58.1

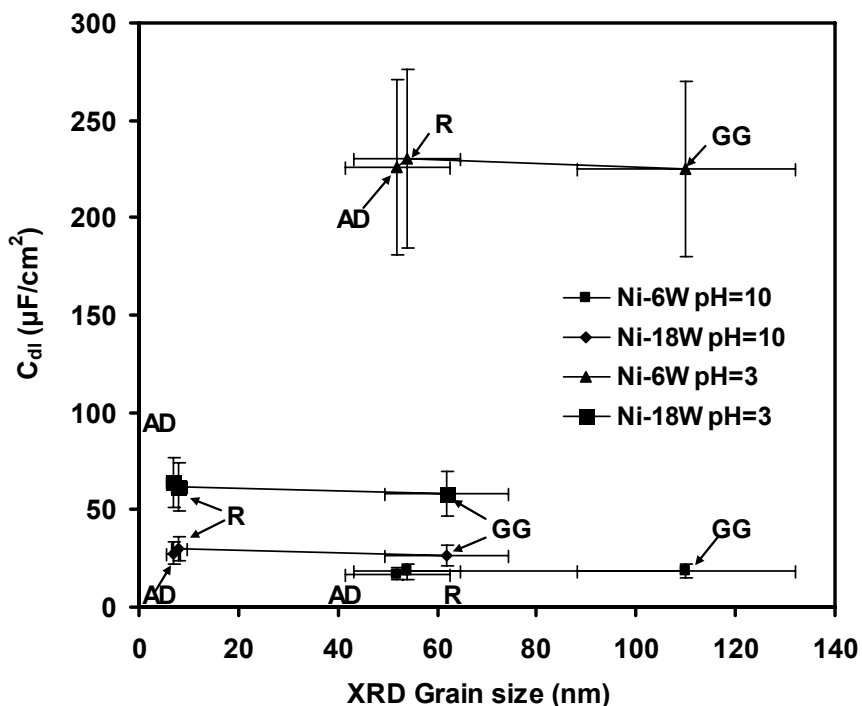


Fig. 5-4 The plot of double layer capacitance (C_{dl}) vs. grain size for Ni-6W and Ni-18W specimen series in pH=10 and 3 3.5wt.% NaCl solutions. AD denotes as-deposited. R denotes grain boundary relaxation. GG denotes grain growth.

Fig. 5-4 shows the double layer capacitance (C_{dl}) vs. grain size for Ni-6W and Ni-18W specimen series in alkaline and acidic saline solutions. Fig. 5-4 also demonstrates that both grain boundary relaxation and grain growth have negligible impact on the C_{dl} in both alkaline and acid saline environments. Moreover, the C_{dl} values of Ni-6W series are comparable (slightly lower) to those of Ni-18W series in alkaline condition, but the values of the former series are noticeably greater than the latter in acidic condition. At higher corrosion rate (i_{corr}), more ions are populated within the double layer, giving rise to higher polarizability of the media and thus the higher C_{dl} .

(Halliday et al., 2005: 311). Since the difference in i_{corr} values of Ni-6W and Ni-18W series is significantly lower in alkaline ($\sim 3 \mu\text{A}/\text{cm}^2$) (Fig. 4-21b) than in acidic condition ($\sim 15 \mu\text{A}/\text{cm}^2$) (Fig. 4-22b), the difference between C_{dl} values of Ni-6W and Ni-18 series is more dramatic in acidic condition.

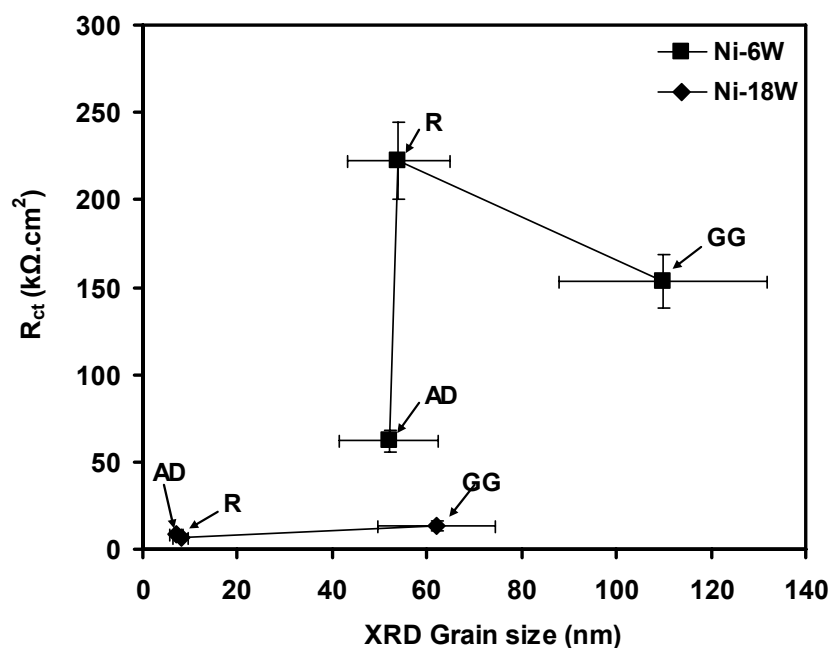


Fig. 5-5 The plot of charge transfer resistance (R_{ct}) vs. grain size for Ni-6W and Ni-18W series in pH=10 3.5 wt.% NaCl solution. AD denotes as-deposited. R denotes grain boundary relaxation. GG denotes grain growth.

The attention is now paid to charge transfer resistance, R_{ct} . From Fig. 5-5, it is apparent that the R_{ct} values Ni-18 series in pH = 10 3.5 wt.% NaCl solution are in agreement with the corresponding corrosion rates (i_{corr}) under the same condition (Fig. 4-21b). That is, both R_{ct} and i_{corr} shows flat trend with respect to grain size. However, the R_{ct} values of Ni-6W series show dramatic change upon grain boundary relaxation and

grain growth, on the contrary to the trend of i_{corr} of this series in the same test condition. The difference between the trends of R_{ct} and i_{corr} of Ni-6W samples in alkaline condition will be discussed in details later on.

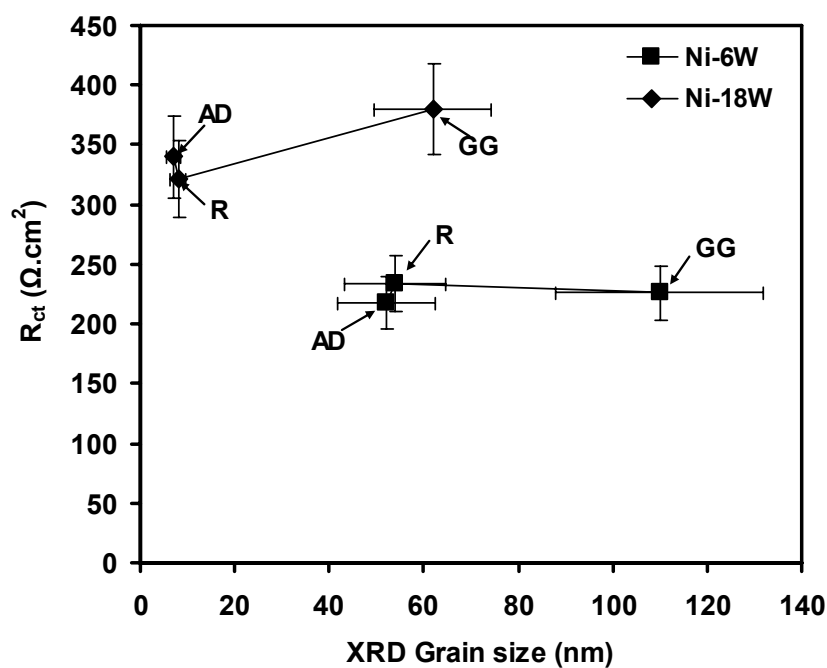


Fig. 5-6 The plot of charge transfer resistance (R_{ct}) vs. grain size for Ni-6W and Ni-18W series in pH=3 3.5 wt.% NaCl solution. AD denotes as-deposited. R denotes grain boundary relaxation. GG denotes grain growth.

Likewise, the charge transfer resistance (R_{ct}) values of Ni-6W and Ni-18W series in pH = 3 3.5 wt.% NaCl solution (Fig. 5-6) are in line with the corresponding corrosion rates (i_{corr}) under the same condition (Fig. 4-22b). That is, both R_{ct} and i_{corr} of Ni-6W and Ni-18W series show the similar flat trend with respect to grain size.

2 Validation of the Interfacial Model

In this section, the aim is to validate the proposed interfacial model for corrosion of Ni-W alloys in acidic and alkaline saline environments. To do so, the values of polarization resistance (R_p) were computed from the i_{corr} data in Part II by Eq. 5-3 (Jones, 1991: 128):

$$R_p = \beta_a \beta_c / 2.303(\beta_a + \beta_c) i_{corr} \quad \text{Eq. 5-3}$$

where R_p = polarization resistance measured in $\Omega \cdot \text{cm}^2$

i_{corr} = corrosion current density measured in A/cm^2

β_a = anodic Tafel slope measured in V/decade

β_c = cathodic Tafel slope measured in V/decade

The computed R_p values of Ni-6W and Ni-18W specimen series in pH=10 and 3 3.5wt% NaCl solutions are shown in Table 5-3. For the proposed interfacial model to be valid, the R_{ct} values calculated from fitting the impedance spectra must be in line with the R_p values computed from i_{corr} . To aid the comparison between R_p and R_{ct} , the R_p values of Ni-6W and Ni-18W series in alkaline (Fig. 5-7) and acidic (Fig. 5-8) saline conditions are plotted as a function of grain size.

Table 5-3 Polarization resistance (R_p), anodic and cathodic Tafel slopes (β_a and β_c) of Ni-6W and Ni-18W specimen series in pH=10 and 3 3.5wt% NaCl solutions.

Sample	pH = 10			pH = 3		
	β_a (V/dec)	β_c (V/dec)	R_p ($\Omega \cdot \text{cm}^2$)	β_a (V/dec)	β_c (V/dec)	R_p ($\Omega \cdot \text{cm}^2$)
Ni-6W-AD	0.067	0.047	8.34×10^4	0.031	0.027	235
Ni-6W-R	0.067	0.048	2.03×10^5	0.033	0.028	262
Ni-6W-GG	0.075	0.055	1.11×10^5	0.032	0.027	247
Ni-18W-AD	0.071	0.049	5.14×10^3	0.026	0.026	637
Ni-18W-R	0.072	0.053	3.84×10^3	0.033	0.032	555
Ni-18W-GG	0.077	0.055	7.00×10^3	0.027	0.027	687

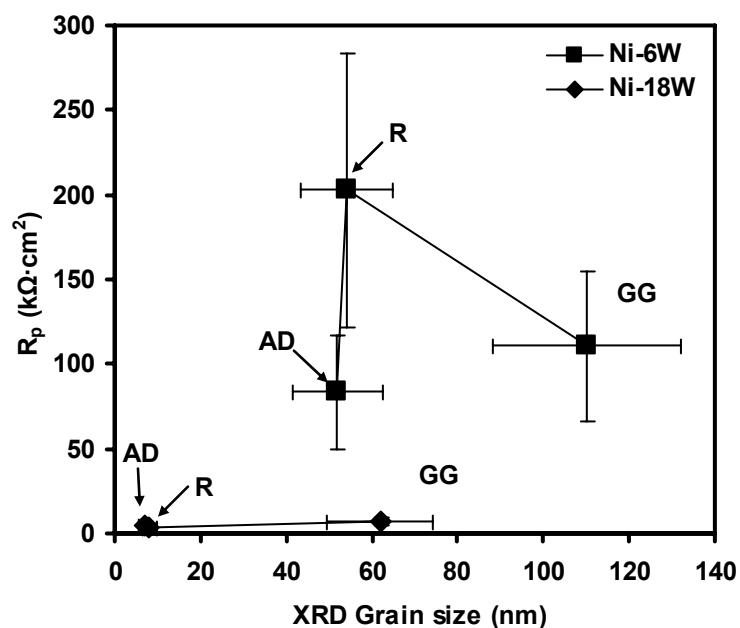


Fig 5-7 The plot of polarization resistance (R_p) (derived from i_{corr}) vs. grain size for Ni-6W and Ni-18W series in pH=10 3.5 wt.% NaCl solution. AD denotes as-deposited. R denotes grain boundary relaxation. GG denotes grain growth.

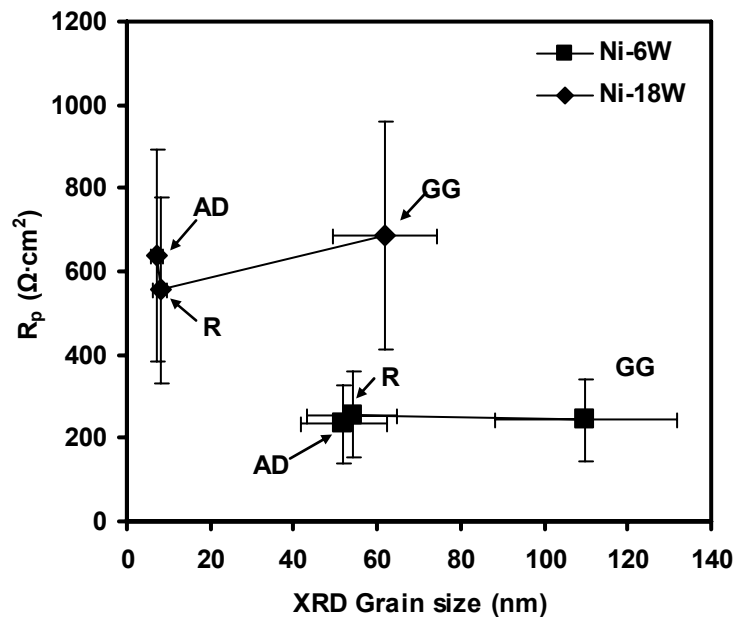


Fig 5-8 The plot of polarization resistance (R_p) (derived from i_{corr}) vs. grain size for Ni-6W and Ni-18W series in pH=3 3.5 wt.% NaCl solution. AD denotes as-deposited. R denotes grain boundary relaxation. GG denotes grain growth.

The comparison between Fig. 5-7 and Fig. 5-5 and between Fig. 5-8 and Fig. 5-6 shows strikingly similar trends and orders of magnitude of R_p and R_{ct} in both alkaline and acidic saline environments. Consequently, the proposed interfacial model for corrosion of Ni-W alloys in aerated alkaline and acidic saline conditions is validated.

3 Corrosion Behavior

It is evident from Fig. 5-5 and 5-6 that there is no significant change in corrosion resistance, which is indicated by R_{ct} , upon grain boundary relaxation and grain growth, confirming the conclusion drawn in Part II. There is, however, an exception

for the trend of corrosion of Ni-6W series in alkaline condition (Fig. 5-5), where the corrosion behavior seems to be dependent upon grain boundary relaxation and grain growth.

In Part II, all the corrosion test results, including the similar polarization curves of different annealed samples (Fig. 4-17 to 4-20) and the flat trend of corrosion with respect to grain size (Fig. 4-21 and 4-22), suggest the insignificant effect of grain boundary relaxation and grain growth on corrosion of electrodeposited nanocrystalline Ni-W in both acidic and alkaline conditions. Moreover, the majority of results in Part III (Fig. 5-5 and 5-6) also suggest the same trend of corrosion behaviors. It is therefore less likely that there is an exception for corrosion of Ni-6W series in alkaline condition.

Fig. 4-8 demonstrates that in alkaline condition the shift in crystallographic texture is the dominating factor controlling corrosion for nanocrystalline Ni-W having grain size larger than 39 nm. The grain sizes of Ni-6W series (52 – 110 nm) under investigation are actually larger than 39 nm. Moreover, Fig. 4-13 shows that there is a shift in crystallographic texture of Ni-6W upon grain boundary relaxation. Upon grain growth, the crystallographic texture was shifted back to the initial texture of Ni-6W-AD. Such shift in the crystallographic texture corresponds well to the increase in R_{ct} value upon grain boundary relaxation and the drop in R_{ct} back to the initial value of Ni-6W-AD upon grain growth (Fig.5-5). This observation in Part III further confirms that in alkaline condition the shift in crystallographic texture is the dominating factor controlling corrosion for nanocrystalline Ni-W having grain size larger than 39 nm.

4 Structural Characteristics for Enhanced Corrosion and Wear Resistance

Based on the findings of this thesis, several structural characteristics that enhance corrosion and wear resistance of nanocrystalline coating are suggested.

4.1 Grain Size

As demonstrated in Fig. 4-8b of Part I, which summarizes the corrosion behavior of as-deposited Ni-W alloys in term of i_{corr} , there is an abrupt transition in the change of i_{corr} with respect to grain size, in both alkaline and acidic saline conditions, as the grain size drop below ~ 10 nm. The mechanism describing such transition is not yet apparent and remains as the challenge for future work. Interestingly, however, as grain size drops below ~ 10 nm, corrosion rates of nanocrystalline Ni-W alloys become increasingly independent of pH and converge to a relatively low value of $\sim 5 \mu\text{A}/\text{cm}^2$ at the grain size of 5 nm regardless of the pH value of the exposed environment. It is consequently suggested that nanocrystalline Ni-W alloys with grain size approximately 5-10 nm be selected as coating materials due to the low corrosion rate at both alkaline and acidic pH. Moreover, the ability for substantial hardness enhancement through grain boundary relaxation, associated with the extremely fine grain size (5-10 nm) makes Ni-W alloys in this range of grain size (5-10 nm) even more attractive as barrier coating.

4.2 Crystallographic Texture

As demonstrated in Part I, in alkaline saline condition where grain size is the dominating factor controlling corrosion, Ni-5W (63 nm), which has larger grain size and

thus lower density of surface reactive sites, should exhibit lower corrosion rate than Ni-6W (39 nm). However, the experimental result shows that the corrosion rate of Ni-5W is actually higher than Ni-6W despite the larger grain size of the former material. This is because the close-packed {111} crystallographic texture of Ni-6W is harder to corrode than the more loosely-packed {200} crystallographic texture of Ni-5W. It is therefore suggested that the coating should be processed such that it has close-packed {111} crystallographic surface texture. Nonetheless, the processing method that achieves this ideal crystallographic surface texture remains the challenge for future work.

4.3 Grain Boundary Relaxation

As demonstrated in Parts II and III, grain boundary relaxation generally have insignificant impact on the corrosion resistance of nanocrystalline Ni-W alloys. Nevertheless, to optimize the performance of nanocrystalline Ni-W alloys as barrier coatings, thermal annealing of these materials is encouraged because it enhances hardness and thus the wear resistance of the coatings through the effect of grain boundary relaxation.

Based on the combination of the three structural characteristics suggested above, a grain-boundary relaxed nanocrystalline Ni-W coating having close-packed {111} crystallographic surface texture with grain size of 5-10 nm is optimal for corrosion and wear resistant coating. We are optimistic that the suggested optimal structural characteristics can be generalized to other nanocrystalline metallic coatings.

5 Concluding Remarks

The findings in Part III can be summarized as follows:

- The impedance spectra and the circuit analog suggest that corrosion reactions of nanocrystalline Ni-W alloys in alkaline and acidic saline conditions are controlled by a charge transfer step. The corresponding interfacial model is also validated through the agreement of R_{ct} derived from EIS results and R_p derived from i_{corr} .
- The EIS results in Part III are in line with the potentiodynamic results in Parts I and II, confirming that (i) in alkaline condition tungsten content and crystallographic texture are the dominant factors controlling corrosion rate for grain size below and above 39 nm, respectively and (ii) tungsten content is the dominant factors controlling corrosion rate in acidic condition.
- It is suggested that the grain-boundary relaxed nanocrystalline Ni-W coating having close-packed {111} crystallographic surface texture with grain size of 5-10 nm is optimal for corrosion and wear resistance.

CHAPTER VI

CONCLUSION

This thesis is the first systematic investigation of corrosion behaviors of nanocrystalline alloys using only one alloy system and only one processing route. Consequently, the variation in chemical composition and structural defects associated with multiple alloy systems and processing routes is eliminated, leading to the significant improvement of reliability and repeatability of experimental results relative to those reported in the literature. The extraordinary consistency of the results is clearly demonstrated by the agreement between the trends in corrosion resistance of Ni-W alloys, measured by two different techniques, namely, potentiodynamic polarization and electrochemical impedance spectroscopy (EIS). Moreover, this thesis addresses all possible factors that may influence corrosion, namely, alloying element, surface composition, pH of the environment and various structural factors including grain size, crystallographic texture and grain boundary relaxation on corrosion of nanocrystalline alloys. Such thorough investigation leads to the fundamental understanding of corrosion behaviors of nanocrystalline alloys. The important findings of this thesis include :

- Nanocrystalline Ni-W alloys with an average XRD grain size between 5 and 63 nm generally exhibit higher corrosion rates in acidic than in alkaline saline environments. However, as XRD grain size approaches 5 nm, the corrosion rate approaches $\sim 5 \mu\text{A}/\text{cm}^2$ regardless of the pH of environments.
- The impedance results suggest that corrosion of nanocrystalline Ni-W alloys in alkaline and acidic conditions is controlled by charge transfer.

- The results in Part I, II and III of this thesis are in line with one another. All of them demonstrate that (i) in alkaline condition tungsten content and crystallographic texture are the dominant factors controlling corrosion rates for grain size below and above ~40 nm, respectively and (ii) in acidic condition tungsten content are the dominant factors controlling corrosion rates.
- It is suggested that the grain-boundary relaxed nanocrystalline Ni-W coating having close-packed {111} crystallographic texture with grain size between 5 to 10 nm is optimal for corrosion and wear resistance.
- With high surface fractions of grain boundary and triple junctions, nanocrystalline Ni-W alloys resist localized corrosion significantly better than microcrystalline Ni.

In closing, the author would like to point out that there are several structurally related behaviors of nanocrystalline Ni-W alloys that can be generalized to other nanocrystalline metals. These include (i) enhancement of corrosion resistance through close-packed crystallographic texture, (ii) significantly enhanced hardness through thermally activated grain boundary relaxation, especially, for nanocrystalline metals with extremely fine grain size, and (iii) superior localized corrosion resistance of nanocrystalline metals to coarse-grained polycrystalline metals with identical composition. Most importantly, the methodological and analytical framework established in this thesis can be applied to investigate the corrosion behaviors of other nanocrystalline metallic systems in general.

REFERENCES

- Alimadadi, H., Ahmadi, M., and Aliofkhazraei, M., et al. Corrosion Properties of Electrodeposited Nanocrystalline and Amorphous Ni-W Alloy. Materials and Design 30 (2009) : 1356-1361.
- Anik, M., and Osseo-Asare, K. Effect of pH on the Anodic Behavior of Tungsten. Journal of the Electrochemical Society 149 (2002) : B224-B233.
- Aroyo, Y., and Tzonev, N. Pulse Periodic Reverse Plating – New Possibilities for Electrodeposition of Metal Coatings with Improved Properties: Part 1. Plating and Surface Finishing 89 (2002) : 48-53.
- Aroyo, Y., and Tzonev, N. Pulse Periodic Reverse Plating - Possibility for Electrodeposition of Metal Coatings with Improved Properties: Part 2. Plating and Surface Finishing 90 (2003) : 50-54.
- Asaro, R.J., and Suresh, S. Mechanistic Models for the Activation Volume and Rate Sensitivity in Metals with Nanocrystalline Grains and Nano-scale Twins. Acta Materialia 53 (2005) : 3369-3382.
- Asgari, H., Toroghinejad, M.R., and Golozar, M.A. On Texture, Corrosion Resistance and Morphology of Hot-Dip Galvanized Zinc Coatings. Applied Surface Science 253 (2007) : 6769-6777.
- ASM International. ASM Handbook. Vol 3. Alloy Phase Diagrams. Materials Park, OH : ASM, 1992.
- Barsoukov, E., and Macdonald J.R. Impedance Spectroscopy; Theory, Experiment, and Applications. 2nd ed. Hoboken, New Jersey : Wiley Interscience Publications, 2005.
- Boonyongmaneerat, Y., Saengkiattiyut, K., and Saenapitak, S., et al. Effect of WC Addition on Structure and Hardness of Electrodeposited Ni-W. Surface and Coatings Technology 203 (2009) : 3590-3594.
- Brenner, A. Electrodeposition of Alloys: Principles and Practice. New York : Academic Press, 1963.

- Brooks, I. Synthesis and Characterization of Nanocrystalline Single α -Phase Zn-Ni alloys coatings. Master's Thesis Department of Materials and Metallurgical Engineering College of Engineering Queen's University, 1998.
- Chandrasekar, M.S., Shanmugasigamani, and Pushpavanam, M. Synergistic Effects of Pulse Constraints and Additives in Electrodeposition of Nanocrystalline Zinc: Corrosion, Structural and Textural Characterization. Materials Chemistry and Physics 124 (2010) : 516-528.
- Chassaing, E., Roumegas, M.P., and Trichet, M.F. Electrodeposition of Ni-Mo Alloys with Pulse Reverse Potentials. Journal of Applied Electrochemistry 25 (1995) : 667-670.
- Chianpairot, A., Lothongkum, G., Schuh, C.A., and Boonyongmaneerat, Y. Corrosion of Nanocrystalline Ni-W Alloys in Alkaline and Acidic 3.5 wt.% NaCl Solutions. Corrosion Science 53 (2011) : 1066-1071.
- da Silva, M., and Klement, U. A Comparison of Thermal Stability in Nanocrystalline Ni- and Co-Based Materials. Zeitschrift Fur Metallkunde 96 (2005) : 1009-1014.
- de Lima-Neto, P., Correia, A.N., and Santana, R.A.C., et al. Morphological, Structural, Microhardness and Electrochemical Characterizations of Electrodeposited Cr and Ni-W Coatings. Electrochimica Acta 55 (2010) : 2078-2086.
- Detor, A.J., and Schuh, C.A. Tailoring and Patterning the Grain Size of Nanocrystalline Alloys. Acta Materialia 55 (2007a) : 371-379.
- Detor, A.J., Miller M.K., and Schuh, C.A. Measuring Grain-Boundary Segregation in Nanocrystalline Alloys: Direct Validation of Statistical Techniques Using Atom Probe Tomography. Philosophical Magazine Letters 87 (2007b) : 581-587.
- Detor, A.J. Grain Size Control and Microstructural Evolution in Nanocrystalline Ni-W Alloys. Doctoral dissertation Department of Materials and Engineering College of Engineering Massachusetts Institute of Technology, 2007c.
- Detor, A.J., and Schuh, C.A. Microstructural Evolution during the Heat Treatment of Nanocrystalline Alloys. Journal of Materials Research 22 (2007d) : 3233-3248.
- Dorf, R.C., and Svoboda, J.A. Introduction to Electric Circuits. 7th ed. Hoboken, New Jersey : John Wiley & Sons, 2006.

- Eckert, J, Holzer, J.C., and Krill, C.E., et al. Structural and Thermodynamic Properties of Nanocrystalline FCC Metals Prepared by Mechanical Attrition. Journal of Materials Research 7 (1992) : 1751-1761.
- Eliaz, N, Sridhar, T.M., Gileadi, E. Synthesis and Characterization of Nickel Tungsten Alloys by Electrodeposition. Electrochimica Acta 50 (2005) : 2893-2904.
- Eliaz, N., and Gileadi, E. The Mechanism of Induced Codeposition of Ni-W Alloys. Transactions of the Electrochemical Society 6 (2007) : 337-349.
- El-moneim, A.A, Gebert, A., and Schneider, F., et al. Grain Growth Effects on the Corrosion Behavior of Nanocrystalline NdFeB Magnets. Corrosion Science 44 (2002a) : 1097-1112.
- El-moneim, A.A., Gebert, A., and Uhlemann, M., et al. The Influence of Co and Ga Additions on the Corrosion Behavior of Nanocrystalline NdFeB Magnets. Corrosion Science 44 (2002b) : 1857-1874.
- El-moneim, A.A., Gutfleisch, O., and Plotnikov, A., et al. Corrosion Behavior of Hot-Pressed and Die-Upset Nanocrystalline NdFeB-Based Magnets. Journal of Magnetism and Magnetic Materials 248 (2002c) : 121-133.
- Erb, U., Aust, K.T., and Palumbo, G. Electrodeposited Nanocrystalline Metals, Alloys and Composites. In Koch, C.C. (eds.), Nanostructured Materials: Processing, Properties and Applications, 235-292. New York : William Andrew Publishing, 2007.
- Farkas, D., Froseth, A., and Van Swygenhoven, H. Grain Boundary Migration during Room Temperature Deformation of Nanocrystalline Ni. Scripta Materialia 55 (2006) : 695-698.
- Furstenau, R.P., McDougall, G., and Langell, M.A. Initial Stages of Hydrogen Reduction of NiO(100). Surface Science 150 (1985) : 55-79.
- Garcia, I., Conde, A., and Langelaan, G., et al. Improved Corrosion Resistance Through Microstructural Modifications Induced by Codeposition of SiC Particles with Electrolytic Nickel. Corrosion Science 45 (2003) : 1173-1189.

- Giga, A., Kimoto, Y., and Takigawa, Y. Demonstration of an Inverse Hall-Petch Relationship in Electrodeposited Nanocrystalline Ni-W Alloys through Tensile Testing. Scripta Materialia 55 (2006) : 143-146.
- Gileadi, E., Kirowa-Eisner, E., and Penciner, J. Interfacial Chemistry: An Experimental Approach. U.S.A. : Addison-Wesley, 1975.
- Gleiter, H. Nanocrystalline Materials. Progress in Materials Science 33 (1989) : 223-315.
- Gleiter, H. Nanostructured Materials: State of the Art and Perspective. Nanostructured Materials 6 (1995) : 3-14.
- Gleiter, H. Nanostructured Materials: Basic Concepts and Microstructure. Acta Materialia 48 (2000) : 1-29.
- Gutkin, M.Y., Ovid'ko, I.A., and Pande, C.S. Yield Stress of Nanocrystalline Materials: Role of Grain-Boundary Dislocations. Philosophical Magazine 84 (2004) : 847-863.
- Gutman, E.M. Mechanochemistry of Solid Surfaces. Singapore : World Scientific Publishing, 1994.
- Halliday, D., Resnick, R., and Walker, J. Fundamentals of Physics. 7th ed. U.S.A. : John Wiley & Sons, 2005.
- Haseeb, A.S.M.A., Albers, U., and Bade, K. Friction and Wear Characteristics of Electrodeposited Nanocrystalline Nickel-Tungsten Alloy Films. Wear 264 (2008) : 106-112.
- Hasnaoui, A., Van Swygenhoven, H., and Derlet, P.M. On Non-Equilibrium Grain Boundaries and Their Effect on Thermal and Mechanical Behaviour: A molecular Dynamics Computer Simulation. Acta Materialia 50 (2002) : 3927-3939.
- Hassani, Sh., Raeissi, K., and Azzi, M., et al. Improving the Corrosion and Tribocorrosion Resistance of Ni-Co Nanocrystalline Coatings in NaOH Solution. Corrosion Science 51 (2009) : 2371-2379.
- Hibbard, G., Aust, K.T., and Palumbo, G., et al. Thermal Stability of Electrodeposited Nanocrystalline Cobalt. Scripta Materialia 44 (2001) : 513-518.
- Hibbard, G., Erb, U., and Aust, K.T., et al. Thermal Stability of Nanostructured Electrodeposits. Materials Science Forum 386-388 (2002) : 387-396.

- Huang, Y.K., Menovsky, A.A., and de Boer, F.R. Electrical Resistivity of Nanocrystalline Copper. Nanostructured Materials 2 (1993) : 505-513.
- Jang, D., and Atzmon, M. Grain-Boundary Relaxation and Its Effect on Plasticity in Nanocrystalline Fe. Journal of Applied Physics 99 (2006) : 083504.
- Jones, A.R, Hamann, J., Lund, A.C., and Schuh, C.A. Nanocrystalline Ni-W Alloys Coating for Engineering Applications. Plating and Surface Finishing 97 (2010) : 52-60.
- Jones, D. Principles and Prevention of Corrosion. U.S.A. : Macmillan, 1991.
- Klement, U., Erb, U., and El Sherik, A.M., et al. Thermal Stability of Nanocrystalline Nickel. Materials Science and Engineering A 203 (1995) : 177-186.
- Klug, H.P., and Alexander, L.E. X-Ray Diffraction Procedures for Polycrystalline and Amorphous Materials. New York : John Wiley & Sons, 1974.
- Liu, L., Li, Y., and Wang, F.H. Influence of Microstructure on Corrosion Behavior of a Ni-Based Superalloy in 3.5% NaCl. Electrochimica Acta 52 (2007) : 7193-7202.
- Lu, H.B., Li, Y., and Wang, F.H. Improved Corrosion Behavior of Nanocrystalline Cu-20Zr Films in HCl Solution. Thin Solid Films 510 (2006) : 197-202.
- Liu, X.H., Liu, W., Lv, X.K., Yang, F., Wei, X., Zhang, Z.D., and Sellmyer, D.J. Magnetic Properties of Nickel Hydroxide Nanoparticles. Journal of Applied Physics 107 (2010) : 083919.
- Luo, W., Qian, C., and Wu, X.J. Electrochemical Corrosion Behavior of Nanocrystalline Copper Bulk. Materials Science and Engineering A 452-453 (2007) : 524-528.
- Macdonald, D.D. Reflections on the History of Electrochemical Impedance Spectroscopy. Electrochimica Acta 51 (2006) : 1376-1388.
- Malow, T.R, and Koch C.C. Thermal Stability of Nanocrystalline Materials. Materials Science Forum 225-227 (1996) : 595-604.
- Mansfeld, F. Electrochemical Impedance Spectroscopy (EIS) as a new tool for investigation methods of corrosion protection. Electrochimica Acta 35 (1990) : 1533.
- Meng, G.Z., Li, Y., and Wang, F.H. The Corrosion Behavior of Fe-10Cr Nanocrystalline Coating. Electrochimica Acta 51 (2006) : 4277-4284.

- Mishra, R., and Balasubramaniam, R. Effect of Nanocrystalline Grain Size on the Electrochemical and Corrosion Behavior of Nickel. Corrosion Science 46 (2004) : 3019-3029.
- Moussa, S.O., Ibrahim, M.A.M., and Abd El Rehim, S.S. Induced Electrodeposition of Tungsten with Nickel from Acidic Citrate Electrolyte. Journal of Applied Electrochemistry 36 (2006) : 333-338.
- Ng, K.T., and Hercules, D.M. Studies of Nickel-Tungsten-Alumina Catalysts by X-ray Photoelectron Spectroscopy. The Journal of Physical Chemistry 80 (1976) : 2094-2102.
- Obradovic, M.D., Bosnjakov, G.Z., and Stevanovic, R.M., et al. Pulse and Direct Current Plating of Ni-W Alloys from Ammonia-Citrate Electrolyte. Surface and Coatings Technology 200 (2006) : 4201-4207.
- Orazem, M.E., Tribollet, B. Electrochemical Impedance Spectroscopy. Hoboken, New Jersey : John Wiley & Sons, 2008.
- Palumbo, G., Thorpe, S.J., and Aust, K.T. On the Contribution of Triple Junctions to the Structure and Properties of Nanocrystalline Materials. Scripta Metallurgica et Materialia 24 (1990) : 1347-1350.
- Park, H. and Szpunar, J.A. The Role of Texture and Morphology in Optimizing the Corrosion Resistance of Zinc-Based Electroplated Coatings. Corrosion Science 40 (1998) : 525-545.
- Puippe, J.C. Pulsed Electrodeposition of Nanocrystalline Metals. In Weil, R., and Barradas, R.G. (eds.), Proceedings of the Symposium on Electrocrystallization, 531-554. New York : The Electrochemical Society, 1980.
- Pumphrey, P.H., and Gleiter, H. Annealing of Dislocations in High-Angle Grain Boundaries. Philosophical Magazine 30 (1974) : 593-602.
- Qin, L.Y., Lian, J.S., and Jian, Q. Effect of Grain Size on Corrosion Behavior of Electrodeposited Bulk Nanocrystalline Ni. Transactions of Nonferrous Metals Society of China 20 (2010) : 82-89.
- Qu, N.S., Chan, K.C., and Zhu, D. Surface Roughening in Pulse Current and Pulse Reverse Current Electroforming of Nickel. Surface and Coatings Technology 91

(1997) : 220-224.

Ramanauskas, R. Structural Factor in Zn Alloy Electrodeposit Corrosion. Applied Surface Science 153 (1999) : 53-64.

Ramanauskas, R., Gudaviciute, L., and Juskenas, R., et al. Structural and Corrosion Characterization of Pulse Plated Nanocrystalline Zinc Coatings. Electrochimica Acta 53 (2007) : 1801-1810.

Raub, E., and Muller, K. Fundamentals of Metal Deposition. New York : Elsevier Publishing Company, 1967.

Rofagha, R., Langer, R., El-Sherik, A.M., Erb, U., Palumbo, G., and Aust, K.T. The Corrosion Behavior of Nanocrystalline Nickel. Scripta Metallurgica et Materialia 25 (1991) : 2867-2872.

Rofagha, R., Langer, R., El-Sherik, A.M., Erb, U., Palumbo, G., and Aust, K.T. Comparison of the Corrosion Behavior of Nanocrystalline and Normal Crystalline Nickel. Materials Research Society Symposium Proceedings 238 (1992) : 751-755.

Rofagha, R., Erb, U., Ostrander, D., Palumbo, G., and Aust, K.T. The Effects of Grain Size and Phosphorus on the Corrosion of Nanocrystalline Ni-P Alloys. Nanostructured Materials 2 (1993) : 1-10.

Ruan, S., and Schuh, C.A. Meso-scale Structure and Segregation in Electrodeposited Nanocrystalline Alloys. Scripta Materialia 59 (2008) : 1218-1221.

Sanders, P.G., Fougere, G.E., and Thompson, L.J., et al. Improvements in the Synthesis and Compaction of Nanocrystalline Materials. Nanostructured Materials 8 (1997) : 243-252.

Sa-nguanmoo, R., Nisaratanaporn, E., and Boonyongmaneerat, Y., et al. Hot-dip galvanization with pulse-electrodeposited nickel pre-coatings. Corrosion Science 53 (2011) : 122-126.

Schiotz, J., Vegge, T., and Di Tolla, F.D., et al. Atomic-Scale Simulations of the Mechanical Deformation of Nanocrystalline Metals. Physical Review B 60 (1999) : 11971.

Schiotz, J., and Jacobsen, K.W. A Maximum in the Strength of Nanocrystalline Copper.

- Science 301 (2003) : 1357-1359.
- Schiotz, J. Atomic-Scale Modeling of Plastic Deformation of Nanocrystalline Copper. Scripta Materialia 51 (2004) : 837-841.
- Schmidt, G. Synthesis of Nanoparticles. In Klabunde, K.J. (eds.), Nanoscale Materials in Chemistry, 23-24. New York : John Wiley & Sons, 2001.
- Schuh, C.A., Nieh, T.G., and Iwasaki, H. The Effect of Solid Solution W Additions on the Mechanical Properties of Nanocrystalline Ni. Acta Materialia 51 (2003a) : 431-443.
- Schuh, C.A., Anderson, K., and Orme, C. Rapid Assessment of Anisotropic Surface Processes: Experiments on the Corrosion of Inconel 600. Surface Science 544 (2003b) : 183-192.
- Slavcheva, E., Mokwa, W., and Schnakenberg, U. Electrodeposition and Properties of NiW Films for MEMS Application. Electrochimica Acta 50 (2005) : 5573-5580.
- Somekawa, H., Nieh, T.G., and Higashi, K. Instrumented Indentation Properties of Electrodeposited Ni-W Alloys with Different Microstructures. Scripta Materialia 50 (2004) : 1361-1365.
- Sriraman, K.R., Raman, S.G.S., and Seshadri, S.K. Synthesis and Evaluation of Hardness and Sliding Wear Resistance of Electrodeposited Nanocrystalline Ni-W Alloys. Materials Science and Engineering A 418 (2006) : 303-311.
- Sriraman, K.R., Raman, S.G.S., and Seshadri, S.K. Corrosion Behavior of Electrodeposited Nanocrystalline Ni-W and Ni-Fe-W Alloys. Materials Science and Engineering A 460-461 (2007a) : 39-45.
- Sriraman, K.R., Raman, S.G.S., and Seshadri, S.K. Influence of Crystallite Size on the Hardness and Fatigue Life of Steel Samples Coated with Electrodeposited Nanocrystalline Ni-W Alloys. Materials Letter 61 (2007b) : 715-718.
- Takano, I., Isobe, S., Sasaki, T.A., and Baba, Y. Nitrogenation of Various Transition Metals by N_2^+ -Ion Implantation. Applied Surface Science 37 (1989) : 25-32.
- Tjong, S.C., and Chen, H. Nanocrystalline Materials and Coatings. Materials Science and Engineering R 45 (2004) : 1-88.
- Trelewicz, J.R., and Schuh, C.A. The Hall-Petch Breakdown in Nanocrystalline Metals: A

- Crossover to Glass-Like Deformation. Acta Materialia 55 (2007) : 5948-5958.
- Trelewicz, J.R. Nanostructure Stabilization and Mechanical Behavior of Binary Nanocrystalline Alloys. Doctoral dissertation Department of Materials Science and Engineering College of Engineering Massachusetts Institute of Technology, 2008.
- Tschope, A., Birringer, R., and Gleiter, H. Calorimetric Measurements of the Thermal Relaxation in Nanocrystalline Platinum. Journal of Applied Physics 71 (1992) : 5391-5394.
- Van Swygenhoven, H., Spaczer, M., and Caro, A., et al. Competing Plastic Deformation Mechanisms in Nanophase Metals. Physical Review B 60 (1999) : 22.
- Van Swygenhoven, H., and Derlet P.M. Grain-Boundary Sliding in Nanocrystalline FCC Metals. Physical Review B 64 (2001) : 224105.
- Van Swygenhoven, H., Derlet, P.M., and Hasnaoui, A. Atomic Mechanism for Dislocation Emission from Nanosized Grain Boundaries. Physical Review B 66 (2002) : 024101.
- Van Swygenhoven, H., Derlet, P.M., and Froseth, A.G. Stacking Fault Energies and Slip in Nanocrystalline Metals. Nature Materials 3 (2004) : 399-403.
- Vanysek, P. Electrochemical Series. In Lide, D.R. (eds.), CRC Handbook of Chemistry and Physics, 534-535. Cleveland, OH : CRC Press, 2006.
- Varin, R.A., and Romanowskiahaftek, E. On the Kinetics of the Spreading of Extrinsic Grain Boundary Dislocations. Metallurgical Transactions A 17 (1986) : 1967-1975.
- Vasko, A.T. Chromium, Molybdenum, and Tungsten. In Bard, A.J. (eds.), Standard Potentials in Aqueous Solution, 239-242. New York : M. Dekker, 1985.
- Wang, L.P., Zhang, J.Y., and Gao, Y., et al. Grain Size Effect in Corrosion Behavior of Electrodeposited Nanocrystalline Ni Coatings in Alkaline Solution. Scripta Materialia 55 (2006) : 657-660.
- Wang, L.P., Lin, Y.M., and Zeng, Z.X., et al. Electrochemical Corrosion Behavior of Nanocrystalline Co Coatings Explained by Higher Grain Boundary Density. Electrochimica Acta 52 (2007) : 4342-4350.

- Wang, S., Rofagha, R., Roberge, P.R., and Erb, U. Corrosion Evaluation of Electrodeposited Bulk Nanocrystalline Nickel. Proceedings of the Electrochemical Society 95-98 (1995) : 224-228.
- Weertman, J.R. Hall-Petch Strengthening in Nanocrystalline Metals. Materials Science and Engineering A 166 (1993) : 161-167.
- Wu, X.L., Zhu, Y.T., and Ma, E. Predictions for Partial-Dislocation-Mediated Processes in Nanocrystalline Ni by Generalized Planar Fault Energy Curves: An Experimental Evaluation. Applied Physics Letters 88 (2006) : 121905.
- Yamakov, V., Wolf, D., and Phillpot, S.R., et al. Deformation Mechanism Crossover and Mechanical Behaviour in Nanocrystalline Materials. Philosophical Magazine Letters 83 (2003) : 385-393.
- Yamasaki, T., Tomohira, R., and Ogino, Y., et al. Formation of Ductile Amorphous and Nanocrystalline Ni-W Alloys by Electrodeposition. Plating and Surface Finishing 87 (2000) : 148-152.
- Yang, F.Z., Guo, Y.F., and Huang, L., et al. Electrodeposition, Structure and Corrosion Resistance of Nanocrystalline Ni-W Alloy. Chinese Journal of Chemistry 22 (2004) : 228-231.
- Younes, O., and Gileadi, E. Electroplating of High Tungsten Content Ni/W Alloys. Electrochemical and Solid State Letters 3 (2000) : 543-545.
- Younes, O., and Gileadi, E. Electroplating of Ni/W Alloys. Journal of the Electrochemical Society 149 (2002) : 100-111.
- Youssef, Kh.M.S., Koch, C.C., and Fedkiw, P.S. Improved Corrosion Behavior of Nanocrystalline Zinc Produced by Pulse-Current Electrodeposition. Corrosion Science 46 (2004) : 51-64.
- Yu, B., Woo, P., and Erb, U. Corrosion Behavior of Nanocrystalline Copper Foil in Sodium Hydroxide Solution. Scripta Materialia 56 (2007) : 353-356.
- Zhang, L., and Macdonald, D.D. Segregation of Alloying Elements in Passive Systems-I. XPS Studies on the Ni-W System. Electrochimica Acta 43 (1998) : 2661-2671.
- Zhang, X.H., Wang, H.Y., and Kassem, M., et al. Origins of Stored Enthalpy in Cryomilled Nanocrystalline Zn. Journal of Materials Research 16 (2001) : 3485-

3495.

Zhang, Z., Zhou, F., and Lavernia, E.J. On the Analysis of Grain Size in Bulk Nanocrystalline Materials via X-ray Diffraction. Metallurgical and Materials Transactions A 34 (2003) : 1349-1355.

Zhu, Y.T., and Langdon, T.G. Influence of Grain Size on Deformation Mechanisms: An Extension to Nanocrystalline Materials. Materials Science and Engineering A 409 (2005) : 234-242.

BIOGRAPHY

Name	Amnuaysak Chianpairot
Birthday	6 January 1974
Education	- Bachelor of Science Department of Materials Science and Engineering, The Johns Hopkins University, 1997 - Master of Science Department of Materials Science and Engineering, University of California, Berkeley, 2001
Current position	- Research assistant, National Metal and Materials Technology Center, 2001